REPORT DOCUMENTATION PAGE		READ INSTRUCTIONS BEFORE COMPLETING FORM
1. REPORT NUMBER AFIT/CI/NR 82-70T	**2. GOVT ACCESSION NO.** AD-A125254	**3. RECIPIENT'S CATALOG NUMBER**
4. TITLE (and Subtitle) Diagnosis of the Comma Cloud of 10 April 1979		**5. TYPE OF REPORT & PERIOD COVERED** THESIS/DISSERTATION
		6. PERFORMING ORG. REPORT NUMBER
7. AUTHOR(s) Daniel Victor Ridge		**8. CONTRACT OR GRANT NUMBER(s)**
9. PERFORMING ORGANIZATION NAME AND ADDRESS AFIT STUDENT AT: University of Oklahoma		**10. PROGRAM ELEMENT, PROJECT, TASK AREA & WORK UNIT NUMBERS**
11. CONTROLLING OFFICE NAME AND ADDRESS AFIT/NR WPAFB OH 45433		**12. REPORT DATE** 1982
		13. NUMBER OF PAGES 108
14. MONITORING AGENCY NAME & ADDRESS(if different from Controlling Office)		**15. SECURITY CLASS. (of this report)** UNCLASS
		15a. DECLASSIFICATION/DOWNGRADING SCHEDULE

16. DISTRIBUTION STATEMENT (of this Report)

APPROVED FOR PUBLIC RELEASE; DISTRIBUTION UNLIMITED

17. DISTRIBUTION STATEMENT (of the abstract entered in Block 20, if different from Report)

18. SUPPLEMENTARY NOTES

APPROVED FOR PUBLIC RELEASE: IAW AFR 190-17

17 Feb 83

LYNN E. WOLAVER
Dean for Research and
Professional Development
AFIT, Wright-Patterson AFB OH

19. KEY WORDS (Continue on reverse side if necessary and identify by block number)

20. ABSTRACT (Continue on reverse side if necessary and identify by block number)

ATTACHED

DD FORM 1473 EDITION OF 1 NOV 65 IS OBSOLETE

UNCLASS

DTIC
ELECTE
MAR 4 1983

H

83 03 03 049

ABSTRACT

On 10 April 1979 a comma cloud developed in association with
a severe storm outbeak in Texas and Oklahoma during the AVE-SESAME 1
regional-scale experiment. With high time- and space-resolution rawin-
sonde data, plus GOES, radar, and surface data, a diagnosis was made of
the structure and evolution of the disturbance which spawned the clouds.
Vertical motion was computed by the kinematic method and from the quasi-
geostrophic omega equation. An alternate partition of the quasi-
geostrophic forcing function was tested. Patterns of Richardson number
(R_i) were compared to the circulation and weather.

Five mesoscale waves in the mid- to high-troposphere strongly
affected the weather patterns on 10 April 1979. These disturbances had
wavelengths from 500 to 800 km, phase speeds of 20 to 33 m/s, and 500mb
height amplitudes around 30m. They showed excellent time continuity in
the 500mb relative vorticity analyses.

Both omega analyses showed 500mb rising motion in eastern New
Mexico six hours before a subsynoptic surface low and tornadic storms
developed just to the east in Texas. Kinematic omegas indicated subsi-
dence over the Texas coastal plain for six hours in the afternoon,
evidently associated with maintenance of a surface pressure ridge and an
intense low-level inversion which inhibited convection in that area.
Regions of very low R_i above 500mb accompanied the mesoscale upper
disturbances. Below 500mb, very low R_i was typical of the region behind
the dry line, the subsynoptic surface low, the warm sector southeast of
that low, and sometimes of the warm front northeast of the low.

Codes
.d/or
Dist   .svcial

A

AFIT RESEARCH ASSESSMENT

The purpose of this questionnaire is to ascertain the value and/or contribution of research accomplished by students or faculty of the Air Force Institute of Technology (ATC). It would be greatly appreciated if you would complete the following questionnaire and return it to:

AFIT/NR
Wright-Patterson AFB OH 45433

RESEARCH TITLE: Diagnosis of the Comma Cloud of 10 April 1979

AUTHOR: Daniel Victor Ridge

RESEARCH ASSESSMENT QUESTIONS:

1. Did this research contribute to a current Air Force project?

( ) a. YES   ( ) b. NO

2. Do you believe this research topic is significant enough that it would have been researched (or contracted) by your organization or another agency if AFIT had not?

( ) a. YES   ( ) b. NO

3. The benefits of AFIT research can often be expressed by the equivalent value that your agency achieved/received by virtue of AFIT performing the research. Can you estimate what this research would have cost if it had been accomplished under contract or if it had been done in-house in terms of manpower and/or dollars?

( ) a. MAN-YEARS _____   ( ) b. $_____

4. Often it is not possible to attach equivalent dollar values to research, although the results of the research may, in fact, be important. Whether or not you were able to establish an equivalent value for this research (3. above), what is your estimate of its significance?

( ) a. HIGHLY   ( ) b. SIGNIFICANT   ( ) c. SLIGHTLY   ( ) d. OF NO
   SIGNIFICANT   SIGNIFICANT   SIGNIFICANCE

5. AFIT welcomes any further comments you may have on the above questions, or any additional details concerning the current application, future potential, or other value of this research. Please use the bottom part of this questionnaire for your statement(s).

NAME	GRADE	POSITION

ORGANIZATION	LOCATION

STATEMENT(s):

THE UNIVERSITY OF OKLAHOMA

GRADUATE COLLEGE

DIAGNOSIS OF THE COMMA CLOUD

OF 10 APRIL 1979

A THESIS

SUBMITTED TO THE GRADUATE FACULTY

in partial fulfillment of the requirements for the

degree of

MASTER OF SCIENCE OF METEOROLOGY

By

DANIEL VICTOR RIDGE

Norman, Oklahoma

1982

ERRATA

p. 24, line 9: "easterlies" should read "westerlies".

p. 35, line 17: "to his case" should read "to this case".

p. 38, line 8: "$35 \times 10^{15} s^{-1}$" should read "$35 \times 10^{-5} s^{-1}$."

p. 72, Figure 3: the mean 500mb height at Denver, Colorado, should read "5428" rather than "5488."

DVR

DIAGNOSIS OF THE COMMA CLOUD

OF 10 APRIL 1979

A THESIS

APPROVED FOR THE DEPARTMENT OF METEOROLOGY

By

Howard B. Bluestein

Jay L. Dunmon

Frederick H. Carr

To Grace and Layla.

To the pros at Air Force Global Weather Central.

ACKNOWLEDGEMENTS

TABLE OF CONTENTS

LIST OF TABLES

LIST OF FIGURES

DIAGNOSIS OF THE COMMA CLOUD

OF 10 APRIL 1979

CHAPTER I

INTRODUCTION

The cloud patterns associated with synoptic scale, midlatitude
cyclonic disturbances usually take on a spiral shape equatorward of the
upper cyclone with a broader region of cloudiness spreading poleward
across the path of the upper trough. Often the pattern is isolated from
other cloudy regions, taking the shape of a vast comma ~2000km long; and
by common usage, any vaguely similar cloud pattern that accompanies
short waves in the westerlies has come to be known as a "comma cloud."

Unfortunately, the term "comma cloud" is used also to refer to
meso-α cloud vortices ~300km long, which occur with vorticity maxima in
the relatively cold air around upper level extratropical cyclones.

Boucher and Newcomb (1962) proposed a model of the lifecycle
of the synoptic scale vortex patterns related to the evolving surface
frontal wave with which they are associated. Efforts to infer the ver-
tical motion field in the vicinity of comma clouds directly from
satellite observed cloudiness failed (Timchalk and Hubert (1961), Leese
(1962), Hansen and Thompson (1964), Nagle, et al. (1966), Barr, et al.

1

(1966)), but the work demonstrated that:

(1) _Instantaneous_ vertical velocity fields do _not_ agree with synoptic-scale cloud patterns, except possibly in the early stages of storm development. Maxima of _instantaneous_ upward and downward motion tend to be upstream of the centers of cloudy and cloud-free areas, respectively, especially in rapidly moving systems. This reinforces the view that clouds result from the time-integrated ascent of parcels which become saturated somewhere downstream of the maximum of instantaneous ascent.

(2) Other factors, such as moisture stratification and the _history_ of vertical motion, which air parcels have experienced, control the _development_ and _dissipation_ of clouds.

(3) The _shape_ of major cloud patterns is due mainly to the horizontal advection of pre-existing cloud matter.

This study will attempt to verify, as did Barr, _et al._ (1966), that, despited the disregard of nongeostrophic advection and other important physical processes, quasi-geostrophic analysis is able to resolve features having a much smaller scale than that appropriate to the theory. It will also compare vertical motion fields calculated by the kinematic and quasi-geostrophic methods, and will attempt to relate fields of low Richardson number to the clouds and circulation.

The _primary_ purpose of this research is to verify and refine the model of the three-dimension flow near developing comma clouds on the basis of fine-scale data, so that forecasters may eventually judge more accurately the location and strength of disturbances indicated by this type of characteristic cloud pattern.

2

CHAPTER II

CASE SELECTION AND METHODOLOGY

This thesis will use international system units throughout except for pressure (millibars), vertical motion (microbars/second), and altimeter setting (inches of mercury).

A. Case Selection

Inspection of geostationary satellite imagery reveals that in only one case during the 1978 and 1979 Atmospheric Variability Experiment (AVE) did a clearly outlined comma cloud cross a dense rawinsonde network, on 10-11 April 1979. The "regional scale" rawinsonde network captured all of the associated storm at lower levels--the dry southwest quadrant, the moist southeast quadrant, and the cool airmass north of the warm front. In mid to high-levels, the trough was slightly west of the AVE-SESAME 1 rawinsonde network until 0600 GMT 11 April 1979, but standard upper air data supplemented the analysis every twelve hours.

3

Associated tornadoes, duststorms, and other severe weather occurred in the SESAME network on this day, including the infamous Wichita Falls, Texas, tornado.

Normally, the term "comma cloud" refers to a synoptic-scale cloud shield which evolves rather gradually in a developing extratropical cyclonic disturbance, or to a meso-α scale cloud in the cold core of an upper cyclone. This comma cloud was unusual in that it developed very rapidly from meso-α to macro proportions above an intense squall line (in the middle of the SESAME data set). This case is representative, in the vigorous extreme, of comma clouds which accompany rapid development and changing weather, and a detailed knowledge of its structure is valuable to operational forecasters.

B. Data Preparation

Data description. Rawinsonde data were available every three hours from 1200 GMT 10 April 1979 to 1200 GMT 11 April 1979, over a "regional scale" network with approximately 214 km average separation of each station from its nearest neighbor. Service C teletype rolls yielded additional 12-hourly reports, while Service A rolls contained hourly surface observations. Figure 1 illustrates the SESAME stations, the standard rawinsonde stations used, and the analysis grid chosen.

Half-hourly satellite photographs consisted of half-mile resolution video data in the daytime and one mile resolution infrared data at night, with the National Earth Satellite Service MB enhancement of the gray scale. Manually digitized radar data were used to locate

4

convective features when gridding was missing or incorrect on the sat-
ellite images. Nephanalyses were prepared by hand from these satellite
images and radar charts, emphasizing convective areas, the duststorm,
and the thunderstorm cirrus canopy which evolved into a comma cloud.

Subjective error analysis. Before archiving the information
on magnetic tape, NASA contractors at Texas A&M University decoded it,
checked it for errors both manually and by machine, and interpolated it
linearly from the surface to 25mb at multiples of 25 millibars
(Fuelberg (1974), Gerhard et al. (1979)). Based on subjectively ana-
lyzed constant-pressure height fields for each time, Gerhard et al.
(1979) decided that some specific rawinsondes were probably in error
because their heights did not appear to fit the overall height pattern
at that particular time (Sanders (1981b)). This approach to error iden-
tification recognizes the potential for error in every individual rawin-
sonde ascent, and it smooths mesoscale features whether they represent
noise or the true state of the atmosphere. However, one may question
whether any analyst can faithfully distinguish noise from real data
during such a disturbed weather situation. Moreover, for this research,
information about features on scales down to 480 kilometers, persistent
on the order of 10 hours, was considered acceptable. It was more
feasible to eliminate any errors consistent in all data from a given
station (e.g., heights reported at Gage, Oklahoma (GAG) were too large
at all times).

For this reason, twelve-hour time-averaged constant-pressure
height charts were prepared for 700mb, 500mb, and 200mb. The average-

5

height charts, subjectively analyzed at a 20 meter interval, are shown as Figures 2-4. These fields suggested that several stations, including Gage, had height errors persistent in time and pressure level. Although many interpretations of Figures 2-4 are possible, the desired result of any data adjustment must be to weaken the height gradients and curvature of contours which the original data indicate are too intense. This was done by subtracting a constant from the heights of all rawinsonde reports for the three most erroneous stations (Gage, Oklahoma (17m high); Abilene, Texas (12m high); and Stephenville, Texas (7m high)), and by adding a constant to the heights of a fourth station (Goodland, Kansas (5m low)), before input to the objective analysis.

Errors in station pressure can lead to errors in the hydrostatically integrated heights above the surface, and Barnes (1981) has cast doubt on the dependability of station pressure for the special SESAME rawinsonde stations. However, Barnes' surface pressure analyses tend to remove transient features in the same manner as the height analyses by NASA and the persistent errors one might expect in the height field aloft can be assessed better right there--in the height field aloft (Sanders (1981b)). Since this is the intent and effect of the corrections to heights at four stations, discussed above, Barnes' station pressure error estimates were not used. The identification and correction of individual errors is explained in the next section of this chapter.

Balloon drift and release time. The SESAME data sets include the balloon release time and location of the balloon relative to the

6

tracking station during ascent. Some researchers (e.g., Moore & Fuelberg (1981), Jedlovec & Fuelberg (1981)) have used this information to increase the accuracy of their analyses. In this study, the actual balloon location downwind of the rawinsonde station was used, rather than station location. All data were linearly interpolated or extrapolated to a common balloon release time as explained in Appendix A.

Static stability. The static stability parameter was calculated at each station at each time, every 100mb from 1000mb to 100mb, with the following equation:

$$\sigma = \frac{287 \times T \times \{\ln(\theta_2) - \ln(\theta_1)\}}{p \times 50 \text{ mb}} \qquad (II.1)$$

where T is the observed temperature at pressure level p, and θ_2 and θ_1 are the potential temperatures 25mb respectively above and below pressure level p. The area averaged sigma is shown in Table 1 as a function of time and pressure.

p(mb)	NACA	Time(GMT)								
		1200	1500	1800	2100	0000	0300	0600	0900	1200
100	1.830	1.605	1.619	1.586	1.628	1.617	1.633	1.720	1.645	1.639
200	.450	.348	.384	.392	.378	.362	.348	.343	.318	.320
300	.070	.060	.061	.070	.062	.061	.058	.057	.059	.077
400	.042	.023	.023	.022	.025	.026	.022	.026	.026	.027
500	.027	.021	.023	.019	.019	.021	.017	.019	.019	.019
600	.020	.017	.016	.017	.016	.013	.013	.013	.014	.016
700	.015	.017	.014	.016	.017	.016	.014	.014	.017	.014
800	.012	.021	.021	.017	.019	.017	.017	.019	.019	.018
900	.010	.035	.037	.035	.021	.021	.024	.025	.021	.023

Table 1: Area averaged static stability parameter σ in units of (m^3/kg) per 100mb for NACA standard and for every three hourly SESAME data set.

The stability parameters for NACA Standard Atmosphere (Haltiner and Martin (1957)) were computed from data at 25mb above and

below each pressure level of interest. The strength of the maximum of stability at 900mb is worthy of note.

Auxiliary soundings. Because of the location of the cloud vortex on the western edge of the SESAME network, it was necessary to use standard 12-hourly rawinsonde data from stations near the western part of the grid (see Figure 1). One must remember that the analyses at 1200 GMT 10 April 1979, and 0000 and 1200 GMT 11 April 1979 had the benefit of this extra information, while the analyses at 1500, 1800, 2100, 0300, 0600, and 0900 GMT did not.

Height, wind direction, and wind speed for these 12-hourly rawinsondes, were extracted from Service C teletype rolls and interpolated to non-mandatory levels (1000, 900, 800, and 600 mb). A logarithmic interpolation was used (see Appendix A for details).

Richardson number. A gradient Richardson number, R_i, was calculated over 25mb intervals, every 25mb, for each rawinsonde by the formula:

$$R_i = \frac{g}{\theta} \frac{\partial \theta}{\partial Z} \bigg/ \left(\frac{\partial |u|}{\partial Z}\right)^2 \tag{II.2}$$

where g is the acceleration of gravity, θ is the potential temperature, $|u|$ is the wind speed, and Z is the height. Wind speeds and potential temperatures were not smoothed or averaged in the vertical. Rawinsondes with low R_i ($0 < R_i \leqslant .25$ and/or $0 < R_i \leqslant .95$) in two vertical domains (at/above 500mb and below 500mb) were plotted on charts for every three hour data set. Two sets of charts (one above 500mb, one below) were analyzed by hand for areas where $0 < R_i \leqslant .25$ enclosed in areas where $0 < R_i \leqslant .95$.

The Richardson number gives a measure of the ratio of buoyant forces to wind accelerations in a vertical column of the atmosphere. As the column becomes more buoyant ($\partial \theta/\partial Z$ decreases) or the vertical difference in kinetic energy (($\partial |u|/\partial Z$)^2) increases R_i decreases. Then the atmosphere is more likely to overturn in turbulent exchange.

Stone (1966) demonstrated that three basically different types of instability may dominate a baroclinic current under different combinations of zonal (k) and meridional (λ) wavenumber, and of Richardson's number (R_i). The problem of the existence and relative power of each of these forms of instability for arbitrary combinations of values of K, λ, R_i is far from solved, but Stone's partial solution suggests very strongly that one may expect:

1. Conventional baroclinic instability for $R_i > 0.95$.

2. Symmetric instability for $0.25 < R_i < 0.95$, exciting motion around axes parallel to the zonal flow.

3. Kelvin-Helmholz instability for $0.25 < R_i$, causing motion around horizontal axes perpendicular to zonal flow.

C. Objective Analysis

Overview. Cressman's (1959) successive approximation proce- dure for interpolating values of randomly spaced data to regularly spaced gridpoints was used in this study. This procedure is sensitive to many factors which can affect the quality of the analysis, such as the choice of the rectangular grid spacing, d, and the maximum radius, R, at which data points influence a gridpoint. An overview of the

9

problems involved will make the solutions taken in this research more understandable.

Given data separated in the average by s=214km, one would like to define gridded values at an interval much smaller than s. However, the expected variance of interpolation error (for the best analysis conditions) increases rapidly as the grid distance decreases below s (Stephens and Stitt (1970), figure 9). The choice of a grid interval only slightly less than s (d=s/1.33) avoids this problem, so d was set to 161 km. Stephens and Stitt (1970) also identified a range of radii of influence, R (defined below) for Cressman analysis of data with separation s to a grid of interval d, over which the error generated by the interpolation operator is minimal. The strategy of using suc-cessively smaller R with increasingly more restrictive error iden-tification, must be done within this range. Stephens and Stitt advise avoiding the lower limit on R, approximately 1.5d, as deduced from their figure 9. Preliminary runs with values of R from 1.5d to 3.5d indicated that this SESAME data set yields a reasonably smooth height analysis for R>3d.

Table 2 (below) shows the five steps which were applied in this analysis, with R ranging from 3d down to 2d. Pass I created a first guess field from the reported data, without reference to data at any other pressure level or time. Every field except the last pass was smoothed with a simple smoothing operator (see Appendix B) to eliminate high frequency noise, although the Cressman weighting function filters

10

much noise at wavelengths less than 2R (Stephens 1967)). No analysis,
objective or subjective, can extract information about disturbances of
wavelengths less than 2s, the lower limit of the ability of the SESAME
data set to discriminate patterns unambiguously. Therefore, for the
last pass, when 2R=3s (since R=2d and d=s/1.33), noise at wavelengths
less than the 2s lower limit of the SESAME data set was definitely eli-
minated by the Cressman analysis without need for final smoothing.
Since the observations may contain unacceptible errors, the Pass I field
was used only to identify the most erroneous data (by a method which
will be discussed below). After Passes II, III, and IV, the latest
values of all fields were substituted for missing reports in the origi-
nal data set and used as bogus for the next pass.

Pass I   R=3.00d = 483km   Smooth.
          Check errors, but do not bogus.

Phase II   R=3.00d = 483km   Smooth.
          Check errors and bogus missing data.

Phase III R=2.67d = 429km   Smooth.
          Check errors and bogus.

Phase IV   R=2.33d = 376km   Smooth.
          Check errors and bogus.

Phase V   R=2.00d = 322km   Do not smooth.

Table 2: Analysis strategy.

Computational grid. The analysis region has 11x12 points in
the horizontal and eleven levels in the vertical: the surface plus
every 100mb from 1000mb to 100mb. Gridpoints below the smooth terrain
analysis were flagged immediately after the height analysis for each
data set. The pressure-coordinate scheme is simpler than a terrain

11

following σ-coordinate system because the data were supplied at
constant pressure levels. The system would require interpolation of
data from pressure to σ-coordinates for computation then back to
pressure coordinates for graphic display. It is hoped that vertical
finite differencing over intervals of constant pressure would yield
more consistent results than differencing between layers, which vary in
pressure separation. For these reasons, the pressure coordinate system
was chosen.

Cressman analysis. Data within a fixed horizontal "radius of
influence", R, of a given gridpoint were averaged after weighting by
the Cressman (1959) weighting function, w:

$$S_0 = \sum_{i=1}^{n} (w_i S_i) / \sum_{i=1}^{n} w_i \quad , \tag{II.3}$$

$$\text{for} \quad w_i = \frac{R^2 - d_i^2}{R^2 + d_i^2} \tag{II.4}$$

where data, S_i, observed at locations (x_i, y_i) within the radius of
influence, R, of the gridpoint (x_0, y_0) were weighted relative to the
distance d_i. Each pressure level was considered independent of data
above or below the level. If rawinsonde reports of height and wind
were both available, the height estimate, Z_i, was augmented by the
height gradient computed from the observed wind assuming geostrophic
balance, and the compound report was weighted four times a simple
height report (Cressman (1959)). Appendix B details further theory
behind this scheme.

Objective error identification. After each analysis pass,
all data were checked against an analyzed value at the rawinsonde loca-

12

tion, calculated by bilinear interpolation of the latest gridded analy-
sis (see Appendix B). Each deviation was checked against an error cri-
terion which varied with pressure level, with parameter, and with the
radius of influence, R. If the deviation was less than the criterion,
the observed value was stored in a working rawinsonde array.
Otherwise, the observation was disregarded for that particular pass,
and the analyzed value was stored in the working array. This working
rawinsonde array was used to calculate the next pass analysis. The
original reports, including missing flags, were stored for reference
throughout the analysis, and re-checked against later pass analyses.
Thus, observations considered "bad" relative to an early, rough analy-
sis could be used later when their comparison to more reasonable analy-
ses indicated the observation was "good."

A visual inspection of the observation/analysis deviations,
$|z_0-z_a|$ and $((u_0-u_a)^2+(v_0-v_a)^2)^{1/2}$, for some of the data showed that the
statistical properties of the data set itself should dictate the height
and wind error criteria. Each of the nine data sets were analyzed by a
single pass with R=3d, giving nine separate analyses of z, u, and v at
each level, and the root-mean-square (r.m.s.) of all data at each
pressure level was accumulated and are illustrated in Table 3.

p(mb)	sfc	1000	900	800	700	600	500	400	300	200	100
σ_z(m)	-	8.5	14.8	16.9	15.1	18.8	19.6	22.6	28.5	30.5	24.7
σ_v(m/s)	4.8	3.6	5.4	6.6	6.5	7.3	8.8	9.8	11.3	9.2	6.5

Table 3: Standard deviation of first-pass analyzed heights and wind
speeds accumulated from all nine sets of observed data.

13

These standard deviations were used to define basic height-dependent criteria, δ_z and δ_v, for testing errors in height and wind, respectively. The basic criteria, δ_T and δ_r, for temperature and relative humidity were taken as twice the r.m.s. errors expected for AVE data (Fuelberg (1974)), independent of height. For the surface pressure tendency, which is used as part of the lower boundary condition on kinematic omega, δ_χ is taken as 50% in order to eliminate only the worst errors.

In order to restrict the error tolerances more and more with each analysis pass, the criteria for error identification were decreased linearly in R from $2\delta_\pi(p)$ at R=3d, to $\delta_\pi(p)$ at R=2d, where δ_π is one of the basic pressure-dependent criteria relative to the parameters (π) which were analyzed. Table 4 indicates the numerical definition of the basic criteria and the testing inequalities which were applied to each piece of data after each analysis pass. Subscripts o and a refer to observed data and analyzed values of height, u and v wind components, pressure tendency, temperature and relative humidity; σ_z and σ_v are pressure-dependent standard deviations of height and wind speed for the entire SESAME data set. The factor (R-1) decreases the criteria linearly with R, the radius of influence.

14

	Basic Criterion:	Application:

Z (height) $\quad \delta_z = \sigma_z(p)$ (meters) $\qquad |Z_0 - Z_a| > (R-1)\delta_z$

$\mathbf{V}$ (vector wind) $\quad \delta_v = \sigma_v(p)$ (meters/second) $\qquad |(u_0-u_a)^2 + (v_0-v_a)^2|^{1/2} > (R-1)\delta_v$

X (surface pressure tendency) $\quad \delta_X = 50\%$ $\qquad |(x_0-x_a)/x_0| > (R-1)\delta_X$ or $(x_0 x_a) < 0$

T (temperature) $\quad \delta_T = 2°C$ $\qquad |T_0 - T_a| > (R-1)\delta_T$

rh (relative humidity) $\quad \delta_r = 20\%$ $\qquad |rh_0 - rh_a|/rh_0 > (R-1)\delta_r$

Table 4: Criteria $(\delta_z, \delta_v, \delta_X, \delta_T, \delta_r)$ for error identification. See text for explanation. Also see Fuelberg (1974) for δ_T and δ_r.

Residual errors. Table 5, below shows the r.m.s. deviations of analyzed fields from the observed data after five analysis passes, with a final radius of influence R=2d. Values at other pressure levels are listed in Tables 7 and 8 in Appendix B.

Time (GMT)	z(m) (500mb)	$|\mathbf{V}|$(m/s)	z(m) (200mb)	$|\mathbf{V}|$(m/s)
1200	5.5	3.1	9.6	5.3
1500	6.6	3.2	9.8	6.3
1800	5.5	3.4	12.1	4.5
2100	6.5	5.0	39.8	5.3
0000	8.8	4.9	23.8	3.8
0300	6.9	4.8	23.1	4.8
0600	6.4	8.2	16.6	9.1
0900	10.0	6.4	14.0	13.2
1200	11.4	4.0	10.5	6.5
	$(\delta_z=19.6)$	$(8.8=\delta_v)$	$(\delta_z=30.5)$	$(9.2=\delta_v)$

Table 5: Final r.m.s. height and vector wind speed errors for each data set at 500mb and 200mb.

Some of the values at 200mb are larger than the criteria δ_z and δ_v, and they deserve the following explanation.

At 2100 GMT, σ_z(200mb)=18.6m for 31 stations inside the analysis grid. However, one station (COU) with a 200m indicated error raises the σ_z for all 32 stations to 39.8m. The analyzed height at COU is consistent in time and space with all data, except the 2100 GMT sounding at COU. The COU heights are reasonable as high as 500 mb, but the indicated error increases from 38m at 400mb, to 115m at 300mb, to 200m at 200mb; and they lose consistency with the 1800 and 0000 GMT soundings from COU. Temperature reports are exceedingly warm in this part of the sounding. All the evidence indicates that the 2100 GMT rawinsonde from COU failed above 500mb, that the reported heights were bad, and that the analysis scheme was able to identify the error.

AT 0900 GMT, σ_v(200mb)=13.2, mainly because the analysis smoothed a very strong jet maximum. The strongest wind at 200mb at that time was at OKC, reported at 83 m/s but analyzed as 41 m/s, with an 43 m/s vector deviation from the observation.

A thorough search for the causes of large r.m.s. errors indicated that the height analysis dealt with height errors very well, but that the wind analysis smoothed some jet streaks to half the intensity a hand analysis shows and also removed mesoscale troughs evident in hand-drawn 500mb streamline analyses. From the understatement of horizontal wind gradients in such regions, one must expect weaker values of kinematically computed vertical motion than a better wind analysis might reveal. The results from this kinematic analysis will be com-

16

pared to kinematic omega computed by Moore and Fuelberg (1981) for
reasonableness.

D. Vertical Velocity

Comparison of methods. Two methods of calculating vertical
motion were used in this study, namely the kinematic and the quasi-
geostrophic (QG) methods. The QG omega equation was chosen for the two
following reasons. First, the cause of vertical motion may be
separated into two physically meaningful parts. The QG analysis is a
compromise between the kinematic method, which provides no such physi-
cal insight, and much more complicated omega equations which also
account for latent heat release, surface friction, advection by the
divergent part of the wind, and so on. Second, these calculations,
based entirely on a smooth height analysis, eliminate the large cumula-
tive error characteristic of the kinematic method which can result from
minor noise in the wind field. Both of these points present paradoxes,
however, which underscore the independence of the two methods.
Krishnamurti (1968) demonstrated what operational forecasters have long
known, that the two first-order terms of QG forcing do not always ade-
quately define the total vertical motion of the atmosphere in response
to complex forcing. Using only the first two terms, one must rely on
experience and empirical guidance to decide whether the non-QG forces
may dominate in some area, and what changes they will cause in the
height field. Second, the kinematic method (adjusted) often yields
omega fields which compare well to the observed clouds and weather

despite the problem of noise. Again, the analyst can never be certain whether any particular kinematic analysis is better or worse than the corresponding QG analysis without comparing the fields to cloud, precipitation, or moisture patterns, or by calculating some higher order version of the omega equation (e.g., Krishnamurti (1968)).

Summary of computations. With the quasigeostrophic (QG) omega equation, vertical motion was calculated over a 7x8 gridpint interior domain (ω=o around around the sides) using boundary conditions specified at 100mb (ω=o) and at the first vertical level above terrain (generally 900mb in the east and 800mb in the west). Kinematic omega was computed over a 9x11 grid and adjusted to zero at 100mb using O'Brien's (1969) quadratic technique. Two different types of lower boundary condition were used: one for the kinematic method and another for the QG method.

The QG omega field was partitioned in two separate ways. The traditional partition between forcing due to differential vorticity advection and to thermal advection, and also an alternate partition between forcing due to advection of vorticity by the thermal wind and to a deformation function both were computed.

Top boundary conditions. At the top (100mb) omega can be assumed to be zero or it can be calculated by some independent method, e.g. the adiabatic method. Omega was calculated at 100mb by the (dry) adiabatic method in order to inspect the magnitude of stratospheric vertical motion.

18

Calculations by this method indicated values of omega at 100mb in the range $\pm 1.15\,\mu$b/s for all of the nine data sets (omega fields not illustrated). Thus a representative value of $\pm .5\,\mu$b/s would be susceptible to around $\pm .17\,\mu$b/s rms error, as discussed in Appendix C. As might be expected, this magnitude of error resulted in erratic continuity in the computed omega fields. Therefore, the top boundary condition was assumed to be $\omega = 0$.

Lower boundary conditions. Two types of lower boundary conditions were used, one for each method. First, the kinematic method requires a surface vertical motion which results from observed wind:

$$\omega_s = - \rho_s g(\vec{V}_s \cdot \nabla h) + \chi_s \tag{II.5}$$

where ρ_s, $\vec{V}_s$, and χ_s are the density, observed wind, and local pressure tendency at the surface, h is the terrain height, and g is the acceleration of gravity. Surface pressure, density, and geostrophic wind (used in another boundary condition) were computed indirectly based on the hypsometric equation, as detailed in Appendix C. The observed wind $\vec{V}_s$ was gridded from rawinsonde u and v components, without the use of hourly surface reports.

The QG omega equation is most consistent with the lower boundary condition:

$$\omega_g = -\{\rho_s g(\vec{V}_g \cdot \nabla h)\} \tag{II.6}$$

where

$$\vec{V}_g = \frac{1}{2}\,\vec{k}\,\times \frac{1}{\rho_s f_\circ}\,\nabla P \tag{II.7}$$

19

Here, the surface geostrophic wind, $\vec{V}_g$, is taken as half the value indicated by the gradient of pressure, P, at the terrain height of each gridpoint, in order to account for the decrease in wind speed toward the surface because of friction (Carr (1981)). See Appendix C for the method of computing P hydrostatically from the gridded height field.

Kinematic omega. The kinematic method for calculating omega consists of integrating the continuity equation from the surface upward.

$$\omega_N = \omega_0 + \sum_{k=1}^{N} (P_{k-1} - P_k) \frac{1}{2} (\delta_{k-1} + \delta_k) \tag{II.8}$$

The average divergence, $\frac{1}{2}(\delta_{k-1} + \delta_k)$, over a pressure layer, P_{k-1} to P_k, determines the vertical change in omega over the layer. Only a lower boundary value, ω_0, is required.

If one assumes wind errors at neighboring gridpoints to be independent of one another, then the horizontal gradient of wind would have an r.m.s. error of σ_v/d, because the winds at either end of the 2d interval would each contribute σ_v error. As shown in Appendix C, this leads one to expect errors of about 10 μb/s in omega after vertical integration of divergence. The r.m.s. value of omega at 100mb calculated by the kinematic method before correction to zero was slightly smaller than this expectation (~7.5 μb/s).

A simple but effective technique for adjusting the solution of the kinematic equation (II.8) to some reasonable top boundary value is that due to O'Brien (1969). The top value, ω_k, of a column of K+1 calculated values of omega is in error by an amount ($\omega_k - \omega_{top}$) from the

20

desired boundary value, ω_{top}. One can distribute a correction to each ω_k, either linearly with height:

$$\omega'_k = \omega_k - \frac{k}{K} (\omega_K - \omega_{top}) \qquad\qquad k=0,K \qquad\qquad (II.9)$$

or quadratically:

$$\omega'_k = \omega_k - \frac{k(k+1)}{K(K+1)} (\omega_K - \omega_{top}) \qquad\qquad k=0,K \qquad\qquad (II.10)$$

Experimentation indicated that equation (II.9) distributes too much error into the middle part of the column, creating bulls-eyes in the omega field in mid-levels, more often than not of the opposite sign one would expect from synoptic reasoning. The quadratic adjustment (II.10) controls the corrections at lower levels, eliminates the bulls-eyes at 500mb, and gives somewhat satisfying results at high levels.

In summary, the final product of O'Brien's quadratic technique in this research conforms very well to the synoptic pattern, suggesting that the actual noise problem is less severe than one might expect from the theory of the kinematic method.

The quasi-geostrophic omega equation. In three dimensions,

$$\nabla^2 \omega + f_0^2/\sigma \frac{\partial^2 \omega}{\partial p^2} = F \qquad\qquad (II.11)$$

where f_0 is a constant value of the coriolis parameter, $F(x, y, p)$ is a forcing function, and static stability, σ, depends only on time and pressure. The vertical derivative was computed using finite differences over two hundred millibars.

There are two popular ways to express the QG forcing function:

the traditional

$$F = \frac{f_0}{\sigma} \frac{\partial}{\partial(-p)} \left(-\vec{V}_g \cdot \nabla(\zeta+f) \right) + \frac{R_d}{\sigma p} \nabla^2 \left(-\vec{V}_g \cdot \nabla T \right) \qquad (II.12)$$

$$= F1 + F2$$

and the alternative

$$F = \frac{f_0}{\sigma} \left(-\vec{V}_T \cdot \nabla(2\zeta+f) \right) - \frac{f_0}{\sigma} \left(E\frac{\partial D}{\partial p} - D\frac{\partial E}{\partial p} \right) \qquad (II.13)$$

$$= F3 + F4$$

The first term in equation (II.12), F1, represents forcing by the differential advection of absolute vorticity (ζ+f) by the geostrophic wind $\vec{V}_g$. The second term, F2, is forcing by the laplacian of thermal advection by $\vec{V}_g$. The alternative partition due to Winn-Nielsen (1959) involves Trenberth's (1977) F3=(2A+C) term for the advection of the quantity (2ζ+f) by the thermal wind, $\vec{V}_T$, and Winn-Nielsen's F4=(-2Λ) deformation function, where D and E:

$$D = \frac{\partial v}{\partial x} + \frac{\partial u}{\partial y}; \quad E = \frac{\partial u}{\partial x} - \frac{\partial v}{\partial y} \qquad (II.14)$$

are the so-called shearing and stretching parts of deformation. Finite-difference forms and their mutual consistency are discussed in Appendix C.

Winn-Nielson's formulation permits an easy visualization of the QG vertical motion from an isobaric chart of thickness and (2ζ+f), providing the F4 forcing function is negligible compared to F3. Using the thermal wind indicated by the direction and spacing of thickness "isotherms" (cold on the left), the degree of cyclonic vorticity advec-

22

tion is inversely proportional to omega, without the troublesome $\dfrac{\partial}{\partial(-p)}$ and ∇^2 operators in the F1 and F2 terms. One of the secondary objectives of this research is to examine the magnitude of F4 and the resulting QG omega using fine-scale data, in order to verify the utility of this analysis tool in the vicinity of a strong developing wave.

CHAPTER III

RESULTS

A. Vertical Motion

A few words of explanation will facilitate the discussion of
the nine individual, three-hourly data sets.

The clouds and weather on 10 April 1979 were influenced very
strongly by five meso-α (see Orlanski (1975)) short waves that passed
through the area. These disturbances had wavelengths from 500 to 800
km, phase speeds of 20 to 33m/s, and amplitudes of around 30m in the
500mb height field. They can be followed best in the 500mb relative
vorticity analyses which varied $\pm5 \times 10^{-5}s^{-1}$ as the minor troughs and
ridges passed. Waves of this scale in the extratropical easterlies have
not received much attention in the literature. Because these short
waves are smaller than the better understood synoptic scale short waves
(Palmen and Newton (1969)) they will be called "minor short waves" or
"minor waves" in this thesis. Other researchers have found evidence of
these disturbances in this case. They show up in the 300mb isotach ana-
lyses in Moore and Fuelberg (1981) and in the time cross-sections of
weather, humidity, and vertical motion in Wilson (1981).

24

In this thesis, 500mb ascent downwind of subsidence will be taken as evidence of a minor wave in the mid- to upper-troposphere which can be corroborated, hopefully, in the height and vorticity fields.

Each use of the term "500mb jet" in this discussion will refer to the zone of maximum winds implied by a region of strong 500mb height contour gradient in Figures 5c, 6c, 7c, etc.

For brevity, the total quasi-geostrophic omega resulting from the sum of F1 and F2 forcing, will be called QG omega in constrast to the four partitions of this field by differential vorticity advection (F1 omega), laplacian of thermal advection (F2 omega), advection of vorticity by the thermal wind (F3 omega), and Winn-Nielsen's deformation function (F4 omega). "Kinematic omega" refers to omega computed kinematically and adjusted by O'Brien's quadratic method. Omega of absolute value greater than $10 \mu b/s$ is defined as "strong" vertical motion.

Bear in mind the fact that these data sets are very close in time. Features in the omega analyses which exhibit time continuity should be considered true expressions of the atmosphere as interpreted by the respective mathematical model (QG or kinematic), but features which appear and disappear within six hours must be judged as noise.

Reference to tornado and hail occurrences are taken from the damage summaries in Alberty, et al. (1979).

Daybreak, 10 April 1979. At 1200 GMT (Fig 5a and b) showers accompany a low in the lee of the Colorado Rockies, a cold front in New Mexico, and a developing warm front on the Texas coast. Gulf stratus extends up the Rio Grande valley. A 500mb trough in Kansas (Fig 5c) is

25

minor wave #1 of this case study. A 500 mb ridge across the Texas panhandle separates this trough from minor wave #2 in New Mexico.

Both the QG and kinematic omega fields (Fig 5d and e) show ascent in western Kansas and subsidence in Oklahoma associated with minor wave #1. The ascent in this case is not directly downstream from the descent but is located in the cold air on the left of the 500mb jet which flows from south to north across Kansas (see Fig 5c). Kinematic omega shows 500mb ascent in the showery region of the Texas coast, while QG omega does not. Both methods show an area of ascent in eastern New Mexico at least six hours before the appearance of a subsynoptic surface low (SSL) in west Texas (see Fig 8a).

The two methods disagree about the situation over extreme west Texas. Kinematic omega (Fig 5e) suggests rising motion in advance of another minor wave, and kinematic omega three hours later (Fig 6e) reinforces this inference, as weak subsidence appears south of El Paso, Texas. QG omega shows moderate subsidence (+7μb/s in Fig 5d) over southern New Mexico. Surface temperatures at Carlsbad and Roswell, New Mexico, rose 14°C in two hours, suggesting warming by strong subsidence. The dry line probably began moving some time in the next three hours, but it cannot be located well until 1500 GMT (Fig 6a) in southeastern New Mexico. The surface warming supports the QG omega analysis of subsidence behind minor wave #2.

As indicated in Fig 5f and g, F1 and F2 omega generally te. to cancel one another, except near strong centers where one or the other often dominates. In west Texas and southern New Mexico, cold advection

26

is balancing subsidence warming, so that 500mb temperatures are nearly constant (Fig 5c and 6c). Although one might expect the subsidence warming to weaken faster than the horizontal advection cooling well below 500mb (because the ground does not interrupt horizontal motion as directly as vertical), with consequent low level cooling, the opposite occurs. That is, surface temperatures are rising at the rate of 14°C in two hours.

Figures 5h and 5d show that F3 omega approximates (total) QG omega very well, but exaggerates the maximum value by 25%. For reasons discussed in Appendix C (see equation C.28), deformation forced omega (F4) was calculated by an operator inconsistent with the residual (F1+F2=F3), so that the sum of Fig 5h and i may be slightly different from the QG omega of Fig 5d.

Mid-Morning, 10 April 1979. By 1500 GMT (Fig 6a and b) the cold front is slowing down in New Mexico upwind of a region of pressure falls in southeastern New Mexico. A dry line is apparent in this area and in the Pecos Valley of Texas. Visual satellite data shows Gulf Coast stratus as far northwest as Lubbock, Texas (dewpoint 10°C). Despite the gradual clearing of clouds in east Texas, surface winds, temperatures, and dew points (not illustrated) show a strengthening warm front in the area (Fig 6a). Now three minor waves are evident in the 500mb relative vorticity pattern (Fig 6c): #1 on the Kansas/Nebraska border, #2 in northwest Texas, and a new minor wave #3 in extreme west Texas. Wave #2 seems to be weakening.

The QG and Kinematic omegas (Fig 6d and e) both reflect minor wave #3 in west Texas with a small region of ascent directly over the northern part of the surface dry line, downwind of descent near El Paso, Texas, in the area between the dry line and the cold front. Kinematic omega shows rising motion in northeast Colorado and subsidence in northwestern Oklahoma evidently associated with wave #1.

Kinematic omega shows ascent in south Texas near a thunderstorm area on the coast. This area moves eastward over the following six hours (Fig 6e, 7e, and 8e). Weak subsidence covers northeast Texas in Fig 6e, and skies are clearing there (Fig 5b, 6b, and 7b).

The QG omega pattern (Fig 6d) shows very little structure on the anticyclonic side of the 500mb jet, which flows from southwest to northeast across west Texas and Oklahoma (Fig 6c), especially in comparison with kinematic omega (Fig 6e).

Figures 6f and g reveal that the ascent probably associated with the nascent SSL in eastern New Mexico/West Texas is due entirely to F1 omega. The subsidence in extreme west Texas behind the dry line is forced as much by vorticity advection as by cold advection, in contrast to the domination by F2 omega three hours earlier (Fig 5f and g).

Again F3 omega (Fig 6h) approximates total QG omega (Fig 6d) closely with some exaggeration of the values in closed centers.

Noon, 10 April 1979. At 1800 GMT (Fig 7a and b) severe thunderstorms break out from the bulge on the dry line northward toward Amarillo, Texas. Severe storms break out also in north central Texas between the warm front and the Red River. Wink, Texas, and Carlsbad,

28

New Mexico, first report blowing dust at 1800 GMT. Minor wave #2 is

barely evident in the 500mb relative vorticity pattern (Fig 7c) in

northwest Oklahoma. Minor wave #3 is in southeastern New Mexico just

upstream from the first (weak) tornado of the day (near the thunderstorm

symbol in west Texas on Fig 7b). Low clouds are dissipating in

southeast Colorado after at least six hours of downslope flow.

QG omega (Fig 7d) shows moderate uplift at the dry line bulge.

The ascent region of kinematic omega in eastern New Mexico failed to

move from 1500 to 1800 GMT (Fig 6e and 7e), but remained along the cold

front, where a few thunderstorms are already occurring (Fig 7b). This

is a good example of the ability of the kinematic method to pick out

small regions of active convection. The kinematic omega ascent region

over the Red River is remarkably timely--after many hours of rain and

drizzle, this small area breaks out in hailstorms just before the time

of this analysis (see Alberty, et al. (1979)). QG omega does not show

moderate ascent over this thunderstorm area until 2100 GMT (Fig 8d),

three hours after kinematic omega does. Although the lower tropospheric

convergence resulted in a strong upward flux of mass, moisture, and sen-

sible heat, the transport probably was confined to a few violent thun-

derstorm updrafts. As a result, the 600 to 400mb height patterns and,

hence, the 500mb QG omega pattern remained unchanged on the scale of

this analysis for the first few hours of this convection.

In east Texas, QG omega subsidence disagrees with kinematic

omega rising motion (Fig 7d and e). Kinematic omega compares better

with cloudiness; after several hours of clearing in east Texas, clouds

29

begin to thicken again <u>after</u> 1800 GMT and thunderstorms break out over the Texas/Louisiana border (Fig 6b, 7b, and 8b).

F2 omega ascent over much of north and west Texas is cancelled by F1 omega descent (Fig 7d, f, and g).

<u>Early Afternoon, 10 April 1979.</u> A subsynoptic surface low (SSL) develops around 2100 GMT (Fig 8a) and moves rapidly across the Texas panhandle. The clouds and weather (Fig 8b) change dramatically: a streak of wind-borne dust afflicts west Texas, a thunderstorm system which spawned tornadoes around Lubbock now spreads over the northern panhandle region, tornadic thunderstorms break out west of Wichita Falls, and a comma cloud appears over Oklahoma. A region of thunderstorms in what has become the "dry slot" of the comma cloud, began earlier southwest of Clovis, New Mexico, and now showers are clearly visible in satellite data <u>above the duststorm</u>. If one extrapolates the past position of minor wave #2 to 2100 GMT, it should be in central Kansas in Fig 8c. It is very weak, and is not illustrated in that figure. Minor wave #3 is located in north Texas above the SSL and just north of the tornado area southwest of Wichita Falls, Texas (Fig 8a and b). Minor wave #3 is moving north-northeastward at about 30m/s over the SSL moving east-northeastward at 9m/s. Although positive vorticity advection would indicate pressure <u>falls</u> ahead of minor wave #3, the quasigeostrophic pressure tendency equation allows simultaneous pressure <u>rises</u> there if warm advection is stronger close to the ground than aloft. The rapid development of the SSL as minor wave #3 passed overhead and the outbreak of violent tornadoes just in the wake of the

minor wave suggest that <u>dynamical forcing associated with the mid-level</u> <u>disturbance influenced the low level circulation very strongly for a</u> <u>few hours.</u> It will be interesting to see what happens later as minor wave #3 gets farther away from the SSL and warm front, and also what happens when minor waves #4 and #5 approach the front.

QG and kinematic omega (Fig 8d and e) appear similar. However, QG omega shows near zero vertical motion on the entire right side of the 500mb jet running across western and northern Texas and Oklahoma (Fig 8c and d). This compares poorly with the comma cloud and thunderstorms in Oklahoma (Fig 8b) where kinematic omega shows ascent (Fig 8e). The reason for this major failure of the method is that the QG approximation using only F1 and F2 terms eliminates forcing due to latent heat release, which is becoming important around the convection on the right side of the jet, and also ageostrophic forcing near jet streaks (Ucellini and Johnson (1979)). An analysis of jet streaks and ageostrophic accelerations is beyond the scope of this thesis; but the reader is referred to partial analyses of the same case in Benjamin and Carlson (1982), Kocin, <u>et al.</u> (1982), and Moore and Fuelberg (1981).

Kinematic omega (Fig 8g) indicates subsidence in south Texas. Skies do not clear in this region (Fig 8b); in fact, one would expect continued cloudiness under a strengthening low-level inversion. However, <u>a surface ridge is observed in southeast Texas beginning around</u> <u>2100 GMT</u> (Fig 8a) which is associated with two phenomena. First, the <u>flow of moist air</u> is shunted northwestward between Austin and San

31

Antonio, Texas, so that a tiny area northwest of Mineral Wells, Texas,
becomes extremely unstable ater 2100 GMT (isodrosotherm analysis not
illustrated).   Second, no severe weather occurred along or south of this
sharp surface ridge, probably because of the strong capping inversion.

QG omega (Fig 8d) shows subsidence just upwind of the
duststorm in west Texas/New Mexico and rising motion with that portion
of the comma cloud on the cyclonic side of the 500mb jet (Fig 8c).
Kinematic omega (Fig 8e) indicates a long area of moderate ascent over
the entire comma cloud, centered just east of the most severe thun-
derstorms, and extending over the "dry slot," including the SSL. In
summary, QG omega is poorly related to the comma cloud and kinematic
omega is well related during the first few hours of the comma cloud's
existence.

F1 and F2 vary in time and space more than the total QG
field.   Compare the relatively simple continuity of QG omega in Fig 8d,
9d, and 10d to the interplay between F1 and F2 omega in Fig 8f/g, 9f/g,
and 10f/g.   The F1 and F2 omega fields (Fig 8f and g) have more maxima
and minima than the total QG omega pattern (Fig 8d).   One final obser-
vation of interest is that the F1 omega pattern over Oklahoma and north
Texas in Fig 8f is upwind of the 500mb vorticity advection pattern of
Fig 8c, because the trough axis is vertical from the surface to 500mb
above the SSL, but slopes southwestward above the mid-troposphere.

F3 omega (Fig 8h) exaggerates QG omega (Fig 8d), but also
shows a tiny subsidence region in north Texas just west of the tornadic
cells (Fig 8b).

Late afternon, 10 April 1979. By 0000 GMT (Fig 9a and b)
savage tornadoes have struck at Wichita Falls, Texas, at Lawton,
Oklahoma, and at several towns in central Oklahoma. The comma cloud
has tripled in area. The SSL is moving slowly and filling; the cold
front and dry line move very little. A line of towering cumuli deve-
lops suddenly east of Midland, Texas, about 2300 GMT. Minor wave #3 is
in northern Oklahoma (Fig 9c) and minor wave #4 appears in extreme west
Texas. The most severe thunderstorms are occurring behind minor wave
#3 in central Oklahoma and just northeast of the SSL in Texas.

QG omega (Fig 9d) shows descent over the filling SSL behind
wave #3. The region of kinematically computed ascent in Oklahoma (Fig
9e) is much stronger and broader than the QG omega ascent area. The
most significant difference in the two omega solutions is that the
center of kinematic ascent lies on the 500mb vorticity ridge of minor
wave #3 (Fig 9c), and extends south of the wave slightly beyond the SSL
and warm front in Texas. Figures 7e, 8e, 9e, and 10e indicate
excellent consistency in the kinematic omega pattern, and the clouds
and weather at 0000GMT (Fig 9b) supports the kinematic analysis.
Intense condensation heating in the northwestern half of Oklahoma and
convergence ahead of a low-level jet (not illustrated) in southeast
Oklahoma/northeast Texas are forcing vertical motion which QG omega
cannot discern. In Fig 9b and e, kinematic omega shows rising motion
near all active thunderstorms, including the consistently observed "dry
slot" thunderstorms (northwest of Amarillo, Texas), except for the
upslope area around Colorado Springs. Although the kinematic analysis

33

shows ascent under the comma cloud, it shows moderate ascent in other regions also. QG omega (Fig 9d) indicates ascent only under that part of the comma head over and west of the 500mb jet (Fig 9b and c). The kinematic method gives sharp definition to the subsidence pattern just west of the developing squall line near Midland, Texas (Fig 9b and e).

Evening, 10 April 1979. At 0300 GMT (Fig 10a and b) the SSL is nearly gone. The comma cloud doubled in size in three hours, extending eastward as far as Indiana. Strong surface ridging in west Texas (Fig 10a) is associated with development of a squall line to the east (Fig 10b) which is producing large hail and some tornadoes. Severe storms continue in central Oklahoma east of the SSL along the warm front, but no damaging tornadoes are reported for a few hours. Minor wave #3 in southern Kansas (Fig 10c) is about 300km past that area of weakening severe weather. Minor wave #4, the cold front, and the dry line all intersect at the now tornadic squall line east of Midland, Texas.

The strongest QG omega ascent analyzed in this study (9μb/s) is in Kansas in a region of little or no convective activity (Fig 10b and d). It encompasses the part of the comma head west of the 500mb jet (Fig 10c), but it also invades the dry slot where one might expect subsidence. Kinematic omega (Fig 10e) shows most of the comma in a region of 500mb ascent; however, it also shows moderate dry slot ascent, similar to the QG solution. The comma extends northeastward over a region of subsidence in Iowa. The QG solution does not show much ascent over the strong convection in southwest Missouri, although kine-

34

matic omega does. Both solutions show moderate or better ascent associated with the minor wave in southern Kansas with an important difference: <u>QG omega shows ascent changing to descent as the upper wave passes, while kinematic omega shows strong ascent centered on the troughline of the minor wave, extending several hundred kilometers upstream of the trough.</u> QG omega shows subsidence behind wave #4 in west Texas, but kinematic omega shows rising motion there (Fig 10c, d, and e). The surface ridge in south Texas (Fig 10a) shifts southward under continued (kinematically computed) subsidence.

Beginning at this time, QG omega (Fig 10d) shows intense subsidence over west Texas and southern New Mexico in contradiction to kinematic omega (Fig 10e). Diabatic cooling of the surface would intensify subsidence, so some other ageostrophic forcing must account for this unreasonable QG result. The area is also the scene of moderate F4 (deformation-induced) forcing. In Krishnamurti's (1968) case study, two terms compensated for very strong forcing due to thermal advection in a synoptic location very similar to his case (see his Figures 10 and 11). These were the "differential deformation" and "differential divergence" terms in the balance omega equation. The location was just upstream from an occluding frontal wave, equatorward from the 500mb low (and slightly upstream), on the left flank of the 500mb jet. These two ageostrophic effects may have compensated for strong cold-advection subsidence on 11 April 1979 as well.

F3 omega (Fig 10f) begins to have significant deviations from QG omega (Fig 10h) at this time. In its analysis in west Texas,

Kansas, and Oklahoma, QG omega complements the cloud and weather pat-
terns (Fig 10b) less and less. So this failure of Wiin-Nielsen's
method to approximate QG omega comes at a time when QG omega itself
looks rather poor.

Midnight, 10-11 April 1979. The SSL is gone by 0600 GMT (Fig
11a and b), and the cold front slows down in central Texas. The squall
line in north Texas becomes coincident with the tail of the comma cloud.
Thunderstorms persist in the dry slot of the comma cloud. Three minor
waves are evident in the 500mb relative vorticity pattern (Fig 11c).
Wave #3 is on the Kansas/Nebraska border, wave #4 is in western
Oklahoma, and wave #5 is in southeastern New Mexico. Although some
severe weather continues in northeastern Oklahoma, the most severe thun-
derstorms are occurring at the intersection of minor wave #4 and the
warm front, and behind wave #4 along the cold front in central Texas.

The QG and kinematic omega fields are not even remotely simi-
lar at this time (Fig 11d and e). The QG pattern is generally perpen-
dicular to the comma cloud tail, and some of the active thunderstorms
are in areas of QG omega subsidence (Fig 11b). The kinematic omega
pattern is very similar to the comma cloud except that (1) the
strongest kinematic ascent is along the poleward side of the comma tail,
and (2) the part of the comma head to the left of the 500mb jet (Fig
11c) is indicated as subsiding. Thus, the center line of the comma
tail is slightly downwind (northeast) of the axis of maximum
kinematically-computed ascent. The strongest ascent of the entire
study (13μb/s) is analyzed 200km northeast of the nose of the dry slot.

36

Strong QG omega descent (Fig 11d) in New Mexico is largely the result of F2 omega (Fig 11f), but F1 omega (Fig 11g) shows strong rising motion in north Texas.

Early morning, 11 April 1979. A mesolow forms on the cold front near the Texas/Oklahoma border at 0900 GMT (Fig 12a). Both minor wave #4 in northern Kansas and minor Wave #5 in west Texas are too distant from this region to account for this development (Fig 12c). The squall line in central Texas is moving northeastward, well north of the surface ridge on the Texas coastal plains (Fig 12a and b). Less severe weather in eastern Oklahoma and north Texas was reported at this time of the morning than in earlier hours.

Kinematic omega (Fig 12e) conforms to the comma cloud pattern very well (Fig 12b), except that the ascent in Texas is much more widespread than the clouds and thunderstorms. There has been a consistent pattern since the comma cloud first appeared around 2100 GMT (see Fig 8b/e, 9b/e, 10b/e, 11b/e, and 13b/e) for the kinematic omega to indicate ascent south and southeast of the tip of the comma cloud, and for the comma cloud tail to grow toward the southwest with the repeated squall lines in north Texas. Most of the comma cloud advects downstream very rapidly, but the tip of the comma cloud tail stays in north Texas in a region of rising motion. QG omega (Fig 12d) shows descent just northeast of an active squall line in north Texas and ascent over all of the dry slot (Fig 12b). There is a thunderstorm in the dry slot, but the kinematically computed (Fig 12e) descent over most of the dry slot (except zero at the thunderstorm location) looks

more believable. In northern New Mexico, downslope winds (see the surface omega in Fig 12a) are reflected in the kinematic omega but not in QG omega.

F1 and F2 omegas (Fig 12f and g) both contribute to extreme QG omega subsidence in southeastern New Mexico (Fig 12d). F3 omega (Fig 12h) seems to moderate the QG omega maximum. Recall that F3 omega normally overestimates QG maxima. F4 omega (Fig 12i) rises to $+4\mu b/s$ near a $35 \times 10^{15} s^{-1}$ relative vorticity maximum in New Mexico.

Dawn, 11 April 1979. By 1200 GMT (Fig 13a and b) most of the comma cloud has moved out of the analysis region. Very little severe convection continues. However, minor wave #5 (Fig 13c) is in central Texas approaching the mesolow on the cold front. At this point, one might forecast renewed severe weather activity east and northeast of this mesolow beginning about the time wave #5 would be above the mesolow (say, 1830 GMT). Severe weather did break out again at 1850 GMT south-southeast of the mesolow, and it spread northeastward into Oklahoma, Louisiana, and Arkansas during 11 April 1979 (Alberty, et al. (1979)).

Again, QG omega (Fig 13d) seems unrelated to the comma cloud, thunderstorm, or kinematic omega patterns. Kinematic omega (Fig 13e) compares very favorably with clouds and weather (Fig 13b).

F3 omega (Fig 13h) exaggerates QG omega (Fig 13d) in an analyzed ascent area in central New Mexico. A maximum of relative vorticity (Fig 13c) dominates the F4 omega pattern (Fig 13i).

B. Richardson Number

In areas of low Richardson number (R_i), turbulent motion is favored more than in other areas. This motion moves heat, moisture, and momentum upward from the surface much more efficiently than the rate by molecular diffusion. If areas of low R_i exist near the jet stream level, strong horizontal momentum can be exchanged downward. For these reasons, R_i was analyzed independently in two vertical regimes, one below and one above 500mb. Two criteria for low values of R_i are suggested by Stone (1966). $0.25 < R_i < .95$ may be associated with symmetric instability and $0 < R_i < .25$ may be associated with Kelvin-Helmholz instability.

Figures 14a/b through 22a/b portray general areas of low Richardson number in two vertical regimes: mid/upper troposphere (500-100mb) and boundary layer/lower-troposphere (near surface to 500mb). Each figure shows the region with $0 < R_i < .95$ and, enclosed within this area, with $0 < R_i < .25$. Considering R_i as a continuous mathematical function of height, it is impossible to identify a sounding as having some layer with $0 < R_i < .25$ unless the neighboring layer above and below has $.25 < R_i < .95$. That is, a sounding with a layer with the smaller values of R_i must have, therefore, some nearby layer with the larger values ($0 < R_i < .95$) as well. Areas with $.25 < R_i < .95$ are easy to identify in Fig 14a/b through 22a/b between the outer (solid) contour and the inner (dashed) contour. In Addition, Fig 14b, 15b, 16b, etc. illustrate areas where $R_i < .95$ in the lowest 25mb above the surface, including reports of negative lapse rates of potential temperature.

The fields of Richardson number suggest widespread instability with details that vary considerably over three-hour periods. Fig 14a and 15a compared show that low values of R_i above 500mb spread behind minor wave #1 crossing Kansas. From 1800 to 2100 GMT (Fig 16a and 17a) minor wave #3 leaves a region of low R_i in its wake across west Texas, and has a relatively stable region in central Texas to its south. This instability continues following minor wave #3 through 0300 GMT (Fig 18a and 19a) across Oklahoma. Minor wave #4 exhibits a very similar pattern as it crosses northwest Texas and western Oklahoma in Fig 19a through 22a. Low, even very low Richardson numbers spread on the poleward side of its wake, and a curious stable spot occurs south or southeast of the minor wave trough. By 1200 GMT (Fig 22a) two of these stable regions (one in Arkansas, one in central Texas) and two regions of instability (one in Kansas, one in west Texas) seem to be associated with minor waves #4 (in Nebraska) and #5 (in southwest Oklahoma).

Below 500mb (Fig 14b-22b), low Richardson numbers are found not only in the area behind the dry line, but also around and often northeast of the mesolow in north Texas, and in the warm sector southeast of the mesolow. The unstable region around the mesolow increases in area three times (Fig 17b, 19b, and 22b), possibly in phase with the 500mb minor waves (compare to Fig 17a, 19a, and 22a). A possible explanation for this phenomenon might be that transient wind maxima associated with the minor waves cause ageostrophic low-level accelerations northwestward under the exit region of the upper tro-

40

pospheric jet. With each pulse of the low level, warm flow under the upper jet (see the 850mb analyses in Moore and Fuelberg (1981)), $\partial\theta/\partial z$ decreases and $\partial|u|/\partial z$ increases momentarily.

Figure 16b shows such a region around the Red River at the time severe storms are breaking out in north Texas, even before the SSL arrives.

CHAPTER IV

CONCLUSIONS AND RECOMMENDATIONS

Conclusions. Five mid-level disturbances of wavelength 500 to 800 km passed through the area at speeds of 20 to 33 m/s, evident in strong variations of mid-level height, vorticity, vertical motion, and Richardson number on a three-hour scale. The 500mb quasi-geostrophic (QG) omega field often showed rising followed by subsidence as these disturbances passed, while kinematically computed omega showed ascent on the troughline of these disturbances. The discrepancy between the two omega solutions was probably a result of physical forcing not considered in the simplified QG omega equation, namely latent heat release and ageostrophic response in general. The "minor" short waves were associated with movement of the subsynoptic surface low (SSL) and dry line, with development and filling of the SSL, with the location and onset of severe storms, and with major features of the comma cloud. As two of these waves passed the SSL or the cold front/dry line intersection in central Texas, severe thunderstorms broke out or intensified just northeast through southeast of the surface low and remained violent until the waves were several hundred kilometers downstream.

A comparison of vertical motion computed by the kinematic method (with O'Brien correction) and the QG omega equation method, to clouds and weather indicates that both methods are able to resolve detail in weather phenomena as small as three gridlengths (480 km) under the best circumstances. However, QG omega became very inaccurate as ageostrophic processes became stronger during this study. In fact, both methods give spurious results at times and one can make the following statement: for research purposes these methods make an independent and complementary pair, while for operational purposes the computational ease and ageostrophic sensitivity of the kinematic method make it preferable to the QG method.

In comparison of the QG omega and kinematic omega to clouds and weather, the QG method apparently failed in many situations. It grossly overestimated the subsidence region in southern New Mexico southwest of the closing upper low. Krishnamurti's (1968) solution of the balance wind omega equation for a very similar synoptic situation showed an almost identical subsidence region forced by cold advection, which was counterbalanced by two ageostrophic forcing functions: differential deformation and differential divergence. Kinematic omega consistently analyzed rising motion in active thunderstorm areas. Its ability to locate ascent forced by physical factors neglected in the QG omega equation which was solved, especially latent heat release and ageostrophic accelerations under the exit region of a jet streak, establish the kinematic method as definitely superior to the QG method

43

for forecasting purposes. Sometimes kinematic omega indicated ascent in an area before thunderstorms occurred.

The QG method consistently analyzed 500mb ascent under that portion of the comma "head" to the left of the jet, but elsewhere failed. In general, the QG analysis did not recognize significant vertical motion on the anticyclonic side of the 500mb jet. One may infer, tentatively, that vertical motion due to latent heat release and to ageostrophic forcing on the right of the mid-tropospheric jet became as significant as the quasi-geostrophic forces. In particular, other researchers have found evidence that the accelerations in the exit region of a jet streak became important (Kocin, et al. (1982), Moore and Fuelberg (1981)). As shown in Ucellini and Johnson (1979), strong vertical motion occurs in the low levels of jet streak exit regions, induced by ageostrophic forces.

The relationship of kinematically computed omega to the comma cloud can be summarized as follows.

1. Kinematic omega was always centered on the active convection on the western edge of the comma's tail, so that the center line of the comma tail advected in time slightly east of the axis of maximum instantaneous rising motion.

2. New centers of ascent formed repeatedly southeast and south of the comma tail before the tail extended over these new convective regions.

3. Kinematic calculations indicated that omega in the "dry slot" varied considerably, but tended to be upward around the consistently observed dry slot thunderstorms. The sharp back edge of the

comma cloud can not be taken as a dividing line between instantaneous
descent and ascent.

4. Kinematic omega usually indicated rising motion under
that portion of the comma head to the left of the 500mb jet; however,
in one analysis (0600 GMT) the opposite was true.

Two details of this analysis apply specifically to forecasting
severe thunderstorms in the southern plains in springtime. First, both
the kinematic and the QG analyses showed an area of 500mb rising motion
in eastern New Mexico at least six hours before an SSL and tornadoes
formed just to the east in Texas. Second, subsidence over the Texas
coastal plain caused ridging and the maintenance of an intense low-
level inversion. These features simultaneously surpressed convection
in southeast Texas and diverted moisture northwest of the region.

Minor waves aloft brought on very low Richardson number (R_i)
in the middle- and high-troposphere, plus small regions of high R_i to
their south. Below 500mb, very low R_i was typical of the area west of
the dry line, the SSL, the warm sector southeast of the SSL, and some-
times the warm front area northeast of the SSL. R_i analyses showed
strong vertical wind speed shear directly over the SSL.

Recommendations for further study. Many mechanisms in this
storm are contained in its three-dimensional structures of horizontal
wind, vertical motion, and other parameters. A complete analysis,
particularly a three-dimensional analysis of moisture, clouds, and
weather, could provide a definitive portrait of the evolution of the
system. This thesis highlights three points of departure. First, more
information about the structure of meso-α scale upper disturbances

45

which are termed "minor waves" in this thesis and their relationship to the low level circulation and weather is necessary to the understanding of the organization of cloud patterns and severe weather. The problem of detecting and forecasting these waves is important. Second, the implications of ageostrophic accelerations in the exit region of jet streaks need to be explored and modeled on smaller scales (meso-α or meso-β) than studies heretofore (Ucellini and Johnson (1979)). Third, a fully integrated moisture and cloud analysis every three hours would be an ideal verification tool for all types of cloud forecasting techniques.

A study of the magnitude and source of the subsidence in south Texas may be able to quantify the contributions of adiabatic descent and thermal advection toward maintenance of the capping inversion in that region. Carlson, et al. (1980) have proposed that the advection of warm air heated over the Mexican Plateau is the dominant process that maintains this inversion.

Calculations were made in a pressure coordinate system rather than a σ-coordinate system in hopes of achieving more consistent vertical finite differencing. Unfortunately, (1) a number of gridpoints below ground level were rendered useless in the process, (2) the computer run time required to test for flagged gridpoints is excessive, and (3) the task of programming a computer to test for flags on each use of gridded data proved to be very complicated and time-consuming. Despite the straightforward simplicity and apparently more consistent vertical differencing, the pressure coordinate system is less practical than the σ-coordinate system.

REFERENCES

Alberty, R.L., D.W. Burgess, C.E. Hane, and J.F. Weaver, 1979: SESAME 1979 Operations Summary. National Oceanic and Atmospheric Administration, Boulder, Colorado, 253 pp.

Barr, S., M.B. Lawrence, and F. Sanders, 1966: TIROS vortices and large scale vertical motion. Mon. Wea. Rev, 94, 675-696.

Barnes, S., 1981: Corrections to surface pressure measurements at supplementary SESAME 1979 rawinsonde stations. In Proceedings of the SESAME 1979 Preliminary Results Workshop, Huntsville, Alabama, 10-13.

Benjamin, S.G., and T.N. Carlson, 1981: Numerical simulations of the severe storm environment for the 10-11 April 1979 (SESAME-I) case. In Preprints of the 12th Conference on Severe Local Storms (San Antonio), American Meteorological Society, Boston, 201-204.

Bloom, S.C., 1980: The Objective Analysis of Prestorm Mesoscale Rawinsonde Data through the Imposition of Dynamical Constraints. Doctoral dissertation, University of Illinois, Urbana, Illinois, 109 pp.

Boucher, R.J., and R.J. Newcomb, 1962: Synoptic interpretation of some TIROS vortex patterns: a preliminary cyclone model. J. Appl. Meteor., 1, 127-136.

Bluestein, H.B., 1979: Quasigeostrophic Theory. Unpublished, mimeograph class notes, 52 pp.

Carr, F., 1981: Personal communication.

Carlson, T.N., 1980: Airflow through midlatitude cyclones and the comma cloud pattern. Mon. Wea. Rev., 108, 1498-1509.

Carlson, T.N., R.A. Anthes, M. Schwartz, S.G. Benjamin, and D.G. Baldwin, 1980: Analysis and prediction of severe storms environment. Bull. Am. Meteor. Soc., 61, 1018-1032.

Cressman, G.P., 1959: An operational objective analysis system. Mon. Wea. Rev., 87, 367-374.

Fuelberg, H.E., 1974: Reduction and Error Analysis of the AVE II pilot experiment data. NASA Contract Report CR-120496, Marshall Space Flight Center, Alabama, 131 pp.

Gerhard, M.L., H.E. Fuelberg, S.F. Williams, and R.E. Turner, 1979: AVE-SESAME I: 25-mb sounding data. NASA Tech. Memo. TM-78256, Marshall Space Flight Center, Alabama, 360 pp.

Haltiner, G.J., and F.L. Martin, 1957: Dynamical and Physical Meteorology. McGraw-Hill, New York, 470 pp.

Hansen, J., and A.H. Thompson, 1964: Vertical motion calculations and satellite cloud observations over the western and central United States. J. Appl. Meteor., 4, 18-30.

Jedlovec, G., and H.E. Fuelberg, 1981: A synoptic-scale kinematic energy analysis of the 10-11 April SESAME '79 period. In Proceedings of the SESAME 1979 Preliminary Results Workshop, Huntsville, Alabama, 21-23.

Kocin, P.J., L.W. Uccellini, and R.A. Petersen, 1981: The role of jet streak "coupling" in the development of the 10-11 April 1979 Wichita Falls tornado outbreak. In Preprints of the 12th Conference on Severe Local Storms (San Antonio), American Meteorological Society, Boston, 560-563.

Krishnamurti, T.N., 1968: A study of a developing wave cyclone. Mon. Wea. Rev., 96, 208-217.

Leese, J.A., 1962: The role of advection in the formation of vortex cloud patterns. Tellus, 12, 409-421.

Moore, J., and H.E. Fuelberg, 1981: A synoptic analysis of the first AVE-SESAME '79 period. Bull. Am. Meteor. Soc., 62, 1577-1590.

Nagle, R.E., J.R. Clark, and M.M. Holl, 1966: Tests of the diagnostic-cycle routine in the interpretation of layer-cloud evolutions. Mon. Wea. Rev., 94, 55-66.

O'Brien, J.J., 1969: Alternative solutions to the classical vertical velocity problem. J. Appl. Meteor., 9, 197-203.

Orlanski, I, 1975: A rational subdivision of scales for atmospheric processes. Bull. Am. Meteor. Soc., 56, 527-530.

Palmen, E., and C.W. Newton, 1969: Atmospheric Circulation Systems, Academic Press, New York, 603 pp.

Sanders, F., 1971: Analytic solutions of the nonlinear omega and vorticity equations for a structurally simple model of disturbances in the baroclinic westerlies. Mon. Wea. Rev., 99, 393-407.

Sanders, F., 1981a: The origin and maintenance of the severe thunderstorms of 10 April 1979. In Proceedings of the SESAME 1979 Preliminary Results Workshop, Huntsville, Alabama, 36-37.

Sanders, F., 1981b: Personal communication.

Stephens, J.J., 1967: Filtering responses of selected distance-dependent weight functions. Mon. Wea. Rev., 95, 45-46.

Stephens,J.J., and J.M. Stitt, 1970: Optimum influence radii for interpolation with the method of successive corrections. Mon. Wea. Rev., 98, 680-687.

Stone, P.H., 1965: On non-geostrophic baroclinic instability. J. Atmos. Sci., 23, 390-400.

Timchalk, A., and L.F. Hubert, 1961: Satellite pictures and meteorological analysis of a developing low in the central United States. Mon. Wea. Rev., 89, 429-445.

Trenberth, K.E., 1977: On the interpretation of the diagnostic quasi-geostrophic omega equation. Mon. Wea. Rev., 106, 131-137.

Ucellini, L.W., and D.R. Johnson, 1979: The coupling of upper and lower tropospheric jet streaks and implications for the development of severe convective storms. Mon. Wea. Rev., 107, 682-703.

Vincent, D., and T. Carney, 1981: Kinetic energy budget analysis prior to severe storm outbreak of 10-11 April 1979. In Proceedings of the SESAME 1979 Preliminary Results Workshop, Huntsville, Alabama, p. 20.

Wiin-Nielsen, A., 1959: On a graphical method for an approximate determination of the vertical velocity in the mid-troposphere. Tellus, 11, 432-440.

Williams, S.F., J.R. Scoggins, N. Horvath, and K. Hill, 1980: A preliminary look at AVE-SESAME I conducted on April 10-11, 1979. NASA Tech Memo. TM-78262, Marshall Space Flight Center, Alabama, 56 pp.

Wilson, G., 1981: Structure and dynamics of important mesoscale systems influencing the thunderstorm development during April 10-11, 1979 (AVE SESAME I). In Proceedings of the SESAME 1979 Preliminary Results Workshop, Huntsville, Alabama, 28-31.

Appendix A

Preparation of Data Before Interpolation to a Grid

The AVE-SESAME 1 case contains a total of 335 rawinsonde
ascents made from 39 stations every three hours from 1200 GMT 10 April
1979 through 1200 GMT 11 April 1979. Figure 1   illustrates the geo-
graphic location of these stations. Data were collected at all stations
and at all times except those indicated as missing in Table 6.

		Missing	"Questionable"
1200	10 April	CLL, FSM	BVD, GAG, GLD
1500	10 April	CLL	GAG
1800	10 April	CLL	BVO, GAG
2100	10 April	MRF	FSM, GAG
0000	11 April	BVO, MTX	SEP, GAG
0300	11 April	None	GAG
0600	11 April	ABI, CLL, MTX	LCH, GAG
0900	11 April	BVO, COU, RTN	GAG
1200	11 April	BVO, DUA, UOX	FSM, GAG

Table   6: Missing rawinsondes and rawinsondes which the NASA archivers
considered questionable.

Although NASA archivers considered sixteen of the rawinsondes
"questionable", these data were used without reservation in this analysis.
A subjective analysis explained in Section B of Chapter II indicated the
following biases in height data from four stations: GAG(+17m), ABI(+12m),
SEP(+7m), and GLD(-5m). All height reports from these stations were
corrected before the objective analysis.

50

All data at all pressure levels were interpolated linearly to a balloon release one hour before data time. For example, information from rawinsondes released at Abilene, Texas, at 1121, 1442, and 1740 GMT were used to construct a sounding which would have resulted from a balloon released at 1400 GMT, and these data bear the label "1500 GMT sounding". More explicitly, the linear interpolation to 1400 between 1121 and 1442 was averaged with the linear extrapolation from 1740 past 1442 to 1400.

Surface pressure tendencies were calculated at each time at each station from the rawinsonde reported surface pressure. Because no data was available before the first data set at 1200 GMT, 10 April 1979, the computed surface pressure change designated for that time is actually valid at 1330 GMT. Likewise, the 1200 GMT, 11 April 1979 change is valid at 1030 GMT.

Some data for the 12-hourly standard rawinsonde were computed by hand. Height, wind direction, and windspeed at non-mandatory levels (1000, 900, 800, and 600mb) were calculated by logarithmic interpolation of Service C data $(p_3 < p_2 < p_1)$:

$$Z_2 - Z_1 = (R_d/g) \, \overline{T}_{v(1,2)} \ln(p_1/p_2) \qquad (A.1)$$

$$Z_3 - Z_1 = (R_d/g) \, \overline{T}_{v(1,3)} \ln(p_1/p_3) \qquad (A.2)$$

where p_2 refers to a pressure level between two standard pressure surfaces p_1 and p_3, while Z_1 and Z_3 are reported heights. R_d is the gas constant and g is the acceleration of gravity. Notice that the highest pressure, p_1, may be the station pressure if Z_1 is taken as the station elevation. Now, if the mean virtual temperature $\overline{T}_{v(1,2)}$ in the p_1-p_2 layer is approximately equal to $\overline{T}_{v(1,3)}$ in the p_1-p_3 layer, the equations can be

combined to yield the height Z_2 at p_2:

$$Z_2=Z_1+(Z_3-Z_1)\ln(p_1/p_2)/\ln(p_1/p_3) \qquad (A.3)$$

The error introduced by assuming $\overline{T}_v$ constant causes Z_2 to be estimated too small, because $\overline{T}_{v(1,3)}$ is less that $\overline{T}_{v(1,2)}$ generally (recall $p_3 < p_2 < p_1$). One may estimate the error at 600mb, where it is largest in absolute value due to the logarithmic spreading of pressure layers with height. Assuming $T_v=T$, the solution of Equation (A.3) for NACA Standard Atmospheric heights (Haltiner and Martin (1957)) for $p_3=500$mb, $p_2=600$mb, $p_1=700$mb yields a 600mb height estimate of 4183m. This is 17m less than the standard atmosphere 4200m. This research did not make an adjustment for the expected error in the height estimate, but simply used the result of Equation (A.3).

Terrain heights were derived from two data sources and then smoothed. For gridpoints on or east of 105°W, a U.S. Air Force data set (Carr (1981)) at 1° latitude-longitude interval was interpolated linearly, while west of 105°W, heights were estimated from a 1:3 million scale weather chart.

Appendix B

Gridded Analysis Calculations

The grid chosen for this study is an 11x12 array on a polar stereographic projection, with grid spacing in both directions one inch at 1:7.5 million scale. The reference meridian is 100° west longitude (Figure 1). At 35° north latitude, 161km separates grid points, and this is taken as the nominal grid distance. The average distance of each station from its nearest neighbor for SESAME stations inside the grid (i.e. west of 91° west) is 214km, or 1.33 gridpoints. The grid extends vertically every 100mb from 1000mb to 100mb, plus a surface grid.

Cressman analysis. Data were interpolated to the grid using a Cressman (1959) weighting function:

$$w = \frac{R^2 - d^2}{R^2 + d^2} \quad \text{for } d < R \tag{B.1}$$

where R is a constant radius of influence and d is the distance between the gridpoint and the balloon location at the given pressure level. Figure 23 shows that the weighting function falls from one at the grid point to zero at and beyond distance R.

53

Only data within the radius of influence are used to calculate grid values according to the formula:

$$S_0 = \left(\sum_{i=1}^{n} w_i S_i\right) / \sum_{i=1}^{n} w_i \qquad (B.2)$$

where data, S_i, observed at locations (x_i, y_i) within the radius of influence, R, of a particular gridpoint (x_0, y_0) are weighted relative to the distances from the gridpoint.

The height analysis utilizes the observed wind at each data point to estimate the height gradient. After eliminating second order terms of the Taylor's series expansion of $Z(x,y)$,

$$Z(x+\Delta x, y+\Delta y) = Z(x,y) + \frac{\partial Z}{\partial x} \Delta x + \frac{\partial Z}{\partial y} \Delta y \qquad (B.3)$$

But the observed wind should be a good approximation of the geostrophic wind (Cressman, 1959), except that the observed wind is typically weaker than the geostrophic wind by a factor of 1.08:

$$\frac{\partial Z}{\partial x} = (f_0/g)v_{obs} \times 1.08$$

$$\frac{\partial Z}{\partial y} = (-f_0/g)u_{obs} \times 1.08 \qquad (B.4)$$

for f_0 = constant value coriolis parameter and g = acceleration of gravity. The equation used to calculate height at gridpoints was

$$Z_0 = \sum_{i=1}^{n} w_i k_i \left(Z_i + \frac{\partial Z}{\partial x}(x_i - x_0) + \frac{\partial Z}{\partial y}(y_i - y_0)\right) / \sum_{i=1}^{n} (w_i k_i) \qquad (B.5)$$

with $k_i = 1$ when no wind data were available and $k_i = 4$ otherwise.

After the <u>second</u> pass approximation to the gridded fields, miss-
ing height and wind data were bogused from the latest approximation, and
these bogus data were treated equally with observed data in the next
analysis pass. Thus, there were no missing data in the working rawin-
sonde array after the second pass.

Missing data sometimes made it necessary to increase the fixed
radius of influence in increments of 0.5 gridlengths at individual points
until at least two data points were included. But a listing of radii
greater than 3 gridlengths showed that R=5.0 was the maximum radius (on
the extreme northwest and southwest corners of the grid). Moreover,
when 12-hourly data were available, R was nowhere larger than 3.5.

<u>Smoothing</u>. The simple smoothing technique mentioned throughout
this thesis involves the double application of two one-dimensional
operators:

$$\overline{f}_{i,j}^{\,i} = (1-s)f_{i,j} + \frac{s}{2}(f_{i+1,j}+f_{i-1,j}) \tag{B.6}$$

$$\overline{f}_{i,j}^{\,j} = (1-s)f_{i,j} + \frac{s}{2}(f_{i,j+1}+f_{i,j-1}) \tag{B.7}$$

First (B.6) is applied to the entire field, with $s=+\frac{1}{2}$, then (B.7) is
applied with $s=+\frac{1}{2}$. Next (B.6) is applied with $s=-\frac{1}{2}$; and finally (B.7)
with $s=-\frac{1}{2}$. The response function

$$R(l_x,l_y) = (1-\sin^4\pi d/l_x)(1-\sin^4\pi d/l_y) \tag{B.8}$$

shows the amplitude of smoothed disturbances of wavelength l_x and l_y
in the x and y directions.

$$\overline{f}(l_x,l_y) = f \times R(l_x,l_y) \tag{B.9}$$

In particular 2d waves (in either direction) are completely quashed.

55

Bilinear interpolation. Estimated values of height and wind components were derived by bilinear interpolation of gridded data to the location of the rawinsonde. With reference to Figure 24 , the value of field S at point p_5 between gridpoints g_1 and g_2 is given by

$$S_5 = S_1 x(1-a) + S_2 x(a) \qquad (B.10)$$

and at point p_6 by

$$S_6 = S_3 x(1-a) + S_4 x(a) \qquad (B.11)$$

Then the value of S at the target p_0 between p_5 and p_6 is given by

$$S_0 = S_5 x(1-b) + S_6(b) \qquad (B.12)$$

This same method is used later to interpolate in the vertical and time domains for the trajectory calculations (trilinear and quadrilinear interpolation).

Error calculations. Root-mean-square (r.m.s.) deviations of the SESAME data set were calculated by

$$(\sigma_z(p))^2 = \sum_{t=1}^{9} (\sum_{n=1}^{N_t} (\sum_{i=1}^{11} \sum_{j=1}^{12} (z_0(p) - z_a(p)) |^2_{tp}))/N_z \qquad (B.13)$$

and

$$(\sigma_v(p))^2 = \sum_{t=1}^{9} (\sum_{n=1}^{N_t} (\sum_{i=1}^{11} \sum_{j=1}^{12} [(u_0(p) - u_a(p))^2 \qquad (B.14)$$

$$+ (v_0(p) - v_a(p))^2]_{tp}))/N_v$$

for each pressure level. N_t refers to the number of soundings at time t (1=12Z/10 April, 2=15Z/10 April, etc.). The notation $|_{tp}$ indicates that each piece of sounding data was compared to the analysis for the same time and pressure level. N_z and N_v refer to the total number of deviations that were computed, discounting missing data.

time(GMT) pressure(mb)	1200	1500	1800	2100	0000	0300	0600	0900	1200	σ_z
100	20.2	15.0	11.4	7.7	11.5	33.0	17.2	17.3	14.4	24.7
200	9.6	9.8	12.1	39.8	23.8	23.1	16.6	14.0	10.5	30.5
300	8.8	9.9	10.7	23.3	27.4	13.6	17.6	12.1	12.1	28.5
400	6.5	7.7	7.4	9.7	11.4	7.6	10.3	7.9	9.3	22.6
500	5.5	6.6	5.5	6.5	8.8	6.9	6.4	10.0	11.4	19.6
600	6.8	4.6	4.7	6.2	5.9	6.8	6.7	7.8	7.2	18.8
700	6.2	4.1	5.0	7.1	4.6	5.3	5.6	6.0	8.0	15.1
800	7.9	3.8	5.2	5.2	4.9	5.2	5.2	7.2	5.5	16.9
900	11.2	4.2	4.7	4.9	5.0	7.9	11.3	5.8	4.4	14.8
1000	1.5	2.3	2.2	.9	1.4	2.5	2.6	.2	1.4	8.5

Table 7: R.m.s. height error (m) with R=2d after five passes.

time(GMT) pressure(mb)	1200	1500	1800	2100	0000	0300	0600	0900	1200	σ_v
100	1.4	4.5	1.6	2.6	2.1	2.9	9.4	13.8	7.7	6.5
200	5.3	6.3	4.5	5.3	3.8	4.8	9.1	13.2	6.5	9.2
300	3.9	5.7	4.3	8.5	5.8	6.1	8.8	6.8	7.7	11.3
400	3.4	3.7	3.8	6.2	6.6	6.0	5.9	4.8	4.7	9.8
500	3.1	3.2	3.4	5.0	4.9	4.8	8.2	6.4	4.0	8.8
600	2.6	3.7	3.0	3.1	5.4	4.4	7.4	4.7	3.2	7.3
700	5.0	2.4	2.4	2.8	6.3	4.6	5.9	4.8	5.1	6.5
800	2.5	2.5	2.5	2.5	5.3	5.4	5.6	4.1	4.6	6.6
900	2.0	2.2	2.1	2.1	3.0	3.6	4.6	4.5	3.3	5.4
1000	.9	1.2	.7	.7	.8	2.4	2.0	.8	2.0	3.6
surface	2.1	2.6	2.5	3.0	3.3	4.2	3.8	2.9	2.1	4.8

Table 8: R.m.s. vector wind speed error (m/s).

Tables 7 and 8 list the final r.m.s. deviations of height and wind fields from observed data, after five analysis passes with a final radius of influence R=2d. The reason why 1000mb height and wind errors and 100mb wind errors are so small is that the analysis is constrained by very few reports at these levels. This serves to illustrate the tongue-in-cheek forecaster's maxim, that nothing can ruin a good analysis like more data.

Appendix C

Vertical Velocity: Formulation, Errors, and Consistency

This appendix describes the methods for computing boundary conditions on omega, the finite-difference forms of the kinematic and quasi-geostrophic equations, and such elements as surface pressure, divergence, vorticity, and deformation. When calculating horizontal derivatives on a square grid in polar stereographic projection, it is necessary to calculate a local value of grid distance

$$D = d \times \left(\frac{1+\sin\phi}{1+\sin 60°} \right) \qquad (C.1)$$

as a function of the latitude, ϕ, and the constant grid length d=190.5km valid at 60°N.

The adiabatic method. The finite difference form for omega by the adiabatic method (assuming dry-adiabatic motion) is:

$$\omega = \frac{R_d}{\sigma p} \left\{ \left(\frac{T(t+3hr)-T(t-3hr)}{6 \ hr} \right) + \frac{g}{f_0(2D)^2}(-\Delta_y Z\Delta_x T + \Delta_x Z\Delta_y T) \right\} \qquad (C.2)$$

The operators Δ_x and Δ_y refer to finite differences over two horizontal grid distances. For the first and last data sets, $\frac{\partial T}{\partial t}$ over the nearest three hours was assumed to approximate the value at the end times.

The adiabatic method is sensitive to observational error, especially in the local rate of change of temperature. Let the

58

root-mean-square (r.m.s.) errors of the SESAME observations at 100mb (Fuelberg (1974)) be $\sigma_t = 1°C$ and $\sigma_z = 30m$. For $f_o = .92 \times 10^{-4} s^{-1}$, $p = 10^4$ Pa, $\sigma = 160 \times 10^{-6} m^3/kg/Pa$, 2D=322km, and time differencing over six hours, one would expect an error in the first term of equation (C.2) of $.17 \mu b/s$, and in the second term of $.0045 \mu b/s$. Thus, one would expect errors in 100mb omega computed by the adiabatic method as large as $\pm .17 \mu b/s$.

Derived surface quantities. Although surface temperature was gridded directly from rawinsonde data, surface pressure p_s and the resultant surface density ρ_s were analyzed indirectly from gridded values of the mean virtual temperature in the lowest 100mb above the surface, T_v. This mean virtual temperature was assumed to be more conservative than observed surface pressure and temperature, especially in the mountains.

$$p_s = p \, \exp\left(\frac{g}{R_d T_v}(Z - Z_s)\right) \qquad (C.3)$$

$$\rho_s = p_s \, / \, R_d T_s \qquad (C.4)$$

where Z is the vertically interpolated height 100mb above the surface Z_s, and T_s is the gridded surface temperature.

Since the terrain height varied so much over the analysis domain, the standard approach of calculating geostrophic surface winds from a 1000mb height field obtained by downward extrapolation did not seem justifiable. Instead, a horizontal pressure field, P, was computed locally at each gridpoint at the terrain height of the gridpoint.

Then $\quad u_g = -\dfrac{1}{2}\dfrac{1}{(2D)}\dfrac{\Delta_y P}{f_o \rho_s} \qquad (C.5)$

and

$$v_g = + \frac{1}{2} \frac{1}{(2D)} \frac{\Delta_x P}{f_0 \rho_s} \qquad (C.6)$$

where $f_0 = .92 \times 10^{-4} s^{-1}$ is a constant value of the coriolis parameter and P is the local pressure field. To find P, first a pressure level p_0 was located above the gridpoint terrain height, Z_0, at which all four of the closest gridpoints in the x and y directions were above ground. For each of these neighboring points, the mean virtual temperature in the layer above the surface is taken either as $\tau = T_v$ (discussed above) when p_0 is no more than 100mb above the surface, or as $\tau = \frac{1}{2}(T_v + \overline{T})$, where $\overline{T}$ is the average temperature in the 100mb layer below p_0. Refer to Figure 25. Then for each of the four neighboring points,

$$P_i = p_0 \exp\left(\frac{g}{R_d \tau}(Z_i - Z_0)\right), \quad i=1,4 \qquad (C.7)$$

from the gridded value of Z_i at pressure level p_0 at the respective neighboring points. To repeat, Z_0 is held constant at the terrain height of the center gridpoint where $\vec{V}g$ will be calculated. These four values of P_i, $i=1,4$, are used for one value of u_g and v_g in equations (C.5) and (C.6).

The kinematic method. The finite-difference equation used to calculate divergence from observed wind components is:

$$\delta = \frac{1}{(2D)}(\Delta_x u + \Delta_y v) \qquad (C.8)$$

Let us assume that the average vertical column in the kinematic calculations ran from 800mb to 100mb, and try to estimate the rms error which will develop in the 100mb omega field which will be calculated. Now, the wind errors in two vertically adjacent gridpoints should be positively

60

correlated, assuming the errors are generated consistently during each rawinsonde ascent. The positive correlation need not be large, only greater than zero. Now the root-mean-square error of any quantity (a+b) averaged or integrated from two fields a and b is related to the individual rms errors by:

$$\sigma_{a+b}^2 = \frac{1}{N} \sum_i (\delta(a+b)_i)^2 = \frac{1}{N} \sum_i (\delta a_i + \delta b_i)^2$$

$$= \frac{1}{N} \sum_i ((\delta a_i)^2 + (2\delta a_i \delta b_i) + (\delta b_i)^2) \qquad (C.9)$$

$$= \sigma_a^2 + \sigma_b^2 + 2\frac{1}{N} \sum_i (\delta a_i \delta b_i)$$

Where δa_i and δb_i are the individual errors over N gridpoints, so that $\delta(a+b)_i$ is the individual error of the sum of the fields. Since we assume a and b are positively correllated, $\sum (\delta a_i \delta b_i) > 0$, implying that

$$\sigma_{a+b}^2 > \sigma_a^2 + \sigma_b^2 \qquad (C.10)$$

For a column of seven layers, between 800mb and 100mb, the variance of the mean divergence of a vertical column is larger than the sum of the variances contributed by each layer of the atmosphere.

$$\sigma_\Delta^2 > \sum_{k=1}^{7} \frac{1}{2} (\sigma_{\delta_{k-1}}^2 + \sigma_{\delta_k}^2) \qquad (C.11)$$

where σ_Δ^2 is the variance of the mean divergence in the columnn, δ_k is is the divergence at pressure levels p_0=800mb, p_1=700mb, etc. The factor of $\frac{1}{2}$ accomplishes layer-averaging. Combining equations (C.8), (C.11), and (II.9) and <u>assuming also that</u> $\Delta_x u$ and $\Delta_y v$ each has an r.m.s. error of $2\sigma_v$,

then $\quad \sigma_\omega = (800mb-100mb)\sigma_\Delta$

$$>700mb \times [\sum_{k=1}^{7} \frac{1}{2} (\sigma_{\delta_{k-1}}^2 + \sigma_{\delta_k}^2)]^{1/2} \qquad (C.12)$$

$$>700mb [\sum_{k=1}^{7} \frac{1}{2} ((\frac{4}{2D}\sigma_{v_{k-1}})^2 + (\frac{4}{2D}\sigma_{v_k})^2)]^{1/2}$$

Recall that σ_v, the rms wind error, is a function of pressure. Using the values of σ_v in Table 8 for 1200 GMT/10 April 1979 and 1500 GMT/ 10 April 1979 from 800 mb through 100mb, the expected values of 100mb omega errors would be around 10 ub/s.

In contrast, the values of 100mb omega computed by the kinematic method had an r.m.s. around 7.5 ub/s for these two data sets, most of which is error (that is, adiabatic calculations indicate that 100mb omega should be no greater than 1ub/s in absolute value). The source of this discrepancy ($\sigma_\omega=85ub/s$ vs $\sigma_\omega=7.5ub/s$) lies in the assumption that the horizontal gradients of u and v have r.m.s. errors comparable to $2\sigma_v$.

One must conclude that $\Delta_x u$ and $\Delta_y v$ each has an r.m.s. error no more than $\frac{2}{10}\sigma_v$. It is certainly reasonable to infer that for a Cressman analysis, the horizontal gradient of any scalar has an rms error on the order of 1/10 the error of the scalar itself.

O'Brien's technique. O'Brien's (1969) quadratic correction factor,

$$\kappa(k) = \frac{k(k+1)}{K(K+1)} \qquad k=0,K \qquad (C.13)$$

depends somewhat on the total number of vertical grid spaces, K, but it decreases rapidly for all K to values less than 34% at 500mb and below (see Figure 26).

The quasi-geostrophic method. For indices i, j, and k in the x, y, and (-p) directions, the finite difference form for the residual of the QG omega equation (II.12) is:

$$r_{i,j,k} = (\omega_{i+1,j,k} + \omega_{i,j+1,k} + \omega_{i-1,j,k} + \omega_{i,j-1,k} - 4\omega_{i,j,k})$$

$$+ \frac{f_o^2 D^2}{\sigma(dp)^2} (\omega_{i,j,k+1} + \omega_{i,j,k-1} - 2\omega_{i,j,k})$$

$$-D^2 F_{i,j,k} \qquad (C.14)$$

Here $F_{i,j,k}$ is a pre-defined forcing function, dp is always 200mb, and all values of omega are initialized at zero. Using an overrelaxation factor

$$\alpha = 2/\{1+\sin \arccos (\frac{1}{3} \sum_{i=1}^{3} \cos (\pi/N_i))\} \qquad (C.15)$$

where N_i is the number of grid intervals in each direction, one can make a better guess of omega:

$$\omega'_{i,j,k} = \omega_{i,j,k} + r_{i,j,k} \; \alpha/(4+2\frac{f_o^2 D^2}{\sigma(dp)^2}) \qquad (C.16)$$

The forcing function is fully consistent within itself only if (1) second derivatives are calculated over four gridlengths in combination with first derivatives over two gridlengths, and (2) the factor $(\frac{1+\sin\phi}{1+\sin60°})$ is applied to the reference gridlength d=190.5km locally, at the center of each horizontal finite difference calculated. Since it was deemed necessary to violate (1) in order the maximize the interior domain where values of $F_{i,j,k}$ could be calculated, an alternative to (2) was required as well.

Specifically, laplacians were calculated over two grid lengths

$$\nabla^2 z_{i,j} = \frac{1}{d^2}(z_{i+1,j} + z_{i-1,j} + z_{i,j+1} + z_{i,j-1} - 4z_{i,j}) \quad (C.17)$$

63

and the factor $\left(\dfrac{1+\sin\phi}{1+\sin 60°}\right)^4$ was applied to each value of the forcing

function after all the intermediate calculations were made using a constant d=190.5 km. In addition, the second vertical derivative was computed inconsistent with the first derivative:

$$\frac{\partial^2 \omega}{\partial p^2} = \frac{1}{(dp)^2}(\omega_{k+1}+\omega_{k-1}-2\omega_k) \qquad (C.18)$$

Since relative vorticity has not been corrected for latitude

$$\zeta = \frac{g}{f_0}\nabla^2 x \qquad (C.19)$$

the coriolis parameter must have this correction factor removed:

$$f = 14.292 \, \sin\phi/\left(\frac{1+\sin\phi}{1+\sin 60°}\right)^2 \qquad (C.20)$$

The finite difference forms of the four quasi-geostrophic

forcing functions are (dp=200mb, $K=\left(\dfrac{1+\sin\phi}{1+\sin 60°}\right)$, d=190.5km):

$$F1=\frac{f_0}{\sigma}\frac{K^4}{(dp)}(a_t-a_b) \text{ where} \qquad (C.21)$$

$$a = \frac{g}{f_0}\frac{1}{(2d)^2}(+\Delta_y z\Delta_x(\zeta+f)-\Delta_x z\Delta_y(\zeta+f))$$

from the vorticity advection above (a_t) and below (a_b) the gridpoint.

$$F2 = \frac{R_d}{\sigma p} K^4 \nabla^2 b \qquad \text{where} \qquad \text{(C.22)}$$

$$b_{i,j} = \frac{pg^2/(R_d f_0)}{(dp)(2d)^2}(\Delta_y z(z_{i+1,j,k+1} - z_{i+1,j,k-1} - z_{i-1,j,k+1} + z_{i-1,j,k-1})$$

$$- \Delta_x z(z_{i,j+1,k+1} - z_{i,j+1,k-1} - z_{i,j-1,k+1} + z_{i,j-1,k-1}))$$

where b is horizontal temperature advection.

$$F3 = \frac{g}{\sigma} \frac{K^4}{(dp)(2d)^2}(\Delta_x n(z_{i,j+1,k+1} - z_{i,j+1,k-1} - z_{i,j-1,k+1} + z_{i,j-1,k-1})$$

$$- \Delta_y n(z_{i+1,j,k+1} - z_{i+1,j,k-1} - z_{i-1,j,k+1} + z_{i-1,j,k-1})) \qquad \text{(C.23)}$$

where $n_{i,j} = 2\zeta_{i,j} + f_{i,j}$

$$F4 = \frac{-g}{f_0 \sigma} \frac{K^4}{(2d)^4} \frac{1}{(dp)}(E_{i,j,k}(D_{i,j,k-1} - D_{i,j,k+1})$$

$$- D_{i,j,k}(E_{i,j,k-1} - E_{i,j,k+1})) \qquad \text{(C.24)}$$

where D and E are the components of horizontal deformation. Since F4 can
be calculated either as a residual of the other forcing functions

$$F4_{i,j,k} = F1_{i,j,k} + F2_{i,j,k} - F3_{i,j,k} \qquad \text{(C.25)}$$

or "independently" as a separate function by equation (C.24) it was not
necessary to make F4 consistent with the other forcing functions so long
as the resultant omega fields agreed to a reasonable extent. It seemed
appropriate to compute shearing deformation in a way which is not con-
sistent with derivatives over two gridlengths. The stretching deformation
is computed from four points at a distance ($\sqrt{2}d$) from the center point:

$$E_{i,j} = \frac{2g}{f_0(2d)^2}(z_{i+1,j+1} - z_{i+1,j-1} - z_{i-1,j+1} + z_{i-1,j-1}) \qquad (C.26)$$

A consistent finite difference would be computed from four points at a distance (2d) from the center:

$$D_{i,j} = \frac{g}{f_0(2d)^2}(z_{i+2,j} - z_{i,j+2} - z_{i,j-2} + z_{i-2,j}) \qquad (C.27)$$

One senses a scale inconsistency between the D and E components, as illustrated in Figure 27. Considering the perfect similarity of the two operators (C.26) and (C.27), the analyzed fields will not have the same degree of accuracy unless D is computed from four points at a distance ($\sqrt{2}$d) from the center. The finite difference form for D used in this research was based on linear interpolation

$$D_{i,j} = \frac{2g}{f_0(2d)^2}([\sqrt{2}-1](z_{i+2,j} - z_{i,j+2} - z_{i,j-2} + z_{i-2,j})$$

$$+ [2-\sqrt{2}](z_{i+1,j} - z_{i,j+1} - z_{i,j-1} + z_{i-1,j})) \qquad (C.28)$$

Notice that the factor 2 appears in the numerator analogous to equation (C.26).

Appendix D

Sanders' Analytic Model

The model. An interesting experiment was performed in which a known height field with a known quasi-geostrophic (QG) omega field was compared with the product of Cressman analysis and numerical solution of the QG omega equation.

Sanders (1971) created an analytic model of an atmospheric disturbance and solved the QG omega equation analytically for a three-dimensional omega field. A hypothetical vertical temperature profile, $T_m(p)$, is varied sinusoidally in x(east) and y(north) by the function

$$T(x,y,p)=T_m(p)-(1-\alpha \ln\frac{1000}{p})\times(Ay+T_a\cos\frac{2\pi}{L}x \ \cos\frac{2\pi}{L}y) \qquad (D.1)$$

where the amplitude of the oscillations are specified (T_a), and the oscillations are damped with height to zero at the tropopause. The constant α determines the tropopause pressure, above which the reversed temperature perturbations become unrealistically large. The model requires a synoptic scale wavelength, L, to scale both the north-south and east-west perturbations, and a zonal temperature gradient, A.

Hydrostatic integration of the mean temperature profile, $T_m(p)$, yields a mean height profile, $Z_m(p)$. Now we construct a surface (1000mb) height field ($Z_m(1000)=0$):

67

$$Z(x,y,1000) = z_a\cos\frac{2\pi}{L}(x+\lambda)\cos\frac{2\pi}{L}y \tag{D.2}$$

where z_a is the amplitude of the surface wave and λ is the phase difference between the surface temperature and geopotential perturbations. The vertical integral of temperature gives

$$Z(x,y,p) = z_m(p) + z_a\cos\frac{2\pi}{L}(x+\lambda)\cos\frac{2\pi}{L}y \tag{D.3}$$

$$-\frac{1}{g}[R_d\ln\frac{1000}{p} - (R_d\alpha/2)(\ln\frac{1000}{p})^2](Ay + T_a\cos\frac{2\pi}{L}x\ \cos\frac{2\pi}{L}y)$$

Assuming zero vertical motion at p=1000mb and p=0, Sanders (1971) solved for omega

$$\omega(x,y,p) = \omega_1(p)\ \sin\frac{2\pi}{L}x\ \cos\frac{2\pi}{L}y \tag{D.4}$$

$$+\omega_2(p)\ \sin\frac{2\pi}{L}(x+\lambda)\ \cos\frac{2\pi}{L}y$$

$$+\omega_3(p)\ \sin\frac{4\pi}{L}y$$

where the three pressure-dependent omega functions have quite complicated algebraic expressions. Figures 28a and b illustrate the analytic height, temperature, omega, and (derived) relative vorticity fields generated by equations (D.1) through (D.4).

The analysis. Sanders' equations were used to create gridded values of height and omega, as well as synthetic height soundings at the location of all 47 stations of the SESAME data set at 1200 GMT on 10 April 1979. The constants used in equations (D.1-D.4) were chosen

68

identical to "Case C" in Sanders' (1971) article, except that the mean

temperature profile, $T_m(p)$, was taken from the NACA Standard atmosphere

(Haltiner and Martin (1957)).

$T_m(p)$ (NACA Standard temperature profile)

α .722 (tropopause at 250 mb)

A   1.12°C per 100 km

T_a 7.25°

Z_a 104 gpm ~ $1020 m^2/s^2$

L   2900 km

λ L/4 = 725 km (1000 mb cold center west of 1000 mb low)

Table   9:   Constants supplied to Sanders' analytic model.

    The objective analysis of the 47 synthetic soundings based on

heights alone was quite poor. The worst analysis was at 1000mb:

29m r.m.s. deviation of the gridded height analysis from the synthetic

1000mb height data. But the height field analyzed with the help of

synthetic, quasi-geostrophic winds was superb: 2m r.m.s. height deviation

at 1000mb. The wind analysis (from soundings of geostrophic wind computed

from Sanders' analytic height field differenced over 100km interals) had

r.m.s. errors between 2m/s at the surface and 3.6m/s at 300mb. The wind-

assisted height analysis at 500mb is shown in Figure 29a.

    Next, two forms of Sanders' height field were tested in the

quasi-geostrophic (QG) programs. The height field objectively analyzed

from synthetic soundings was used to compute QG omega for comparison

against the analytic QG omega of equation (D.4). The analytic height

field of equation (D.3) was used to compute the four separately forced

QG components F1, F2, F3=(2A+C), and F4=(-2Λ). In all calculations,

top and bottom boundary conditions were taken as zero, exactly as in

Sanders' model.

Figure 29b shows how well the 500mb QG omega calculation

approximates the analytic QG field, except close to the side boundaries,

where omega was held to zero. The partitions of QG omega in Figure 30a-d

are all reasonable. The most notable feature is the magnitude of vertical

motion due to F4, Winn-Nielsen's deformation function, which is at least

an order of magnitude less than the other three components of QG omega.

The location of this F4-induced omega relative to the synoptic situation

is also of interest.
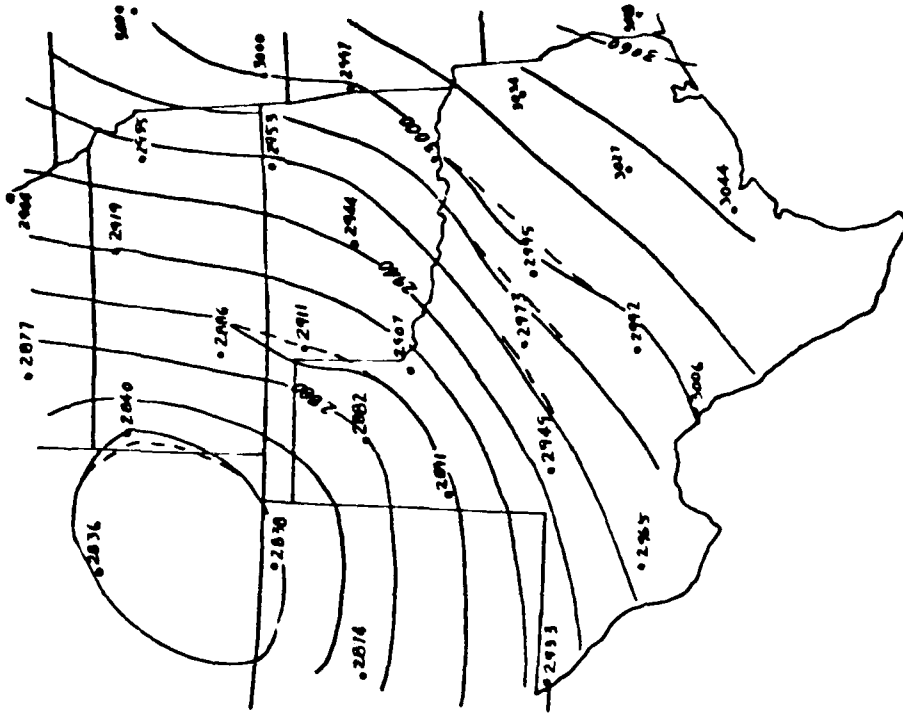
Fig.1: Computational grid, SESAME rawin-
sonde stations (not underlined), and supple-
mental rawinsonde stations (underlined).
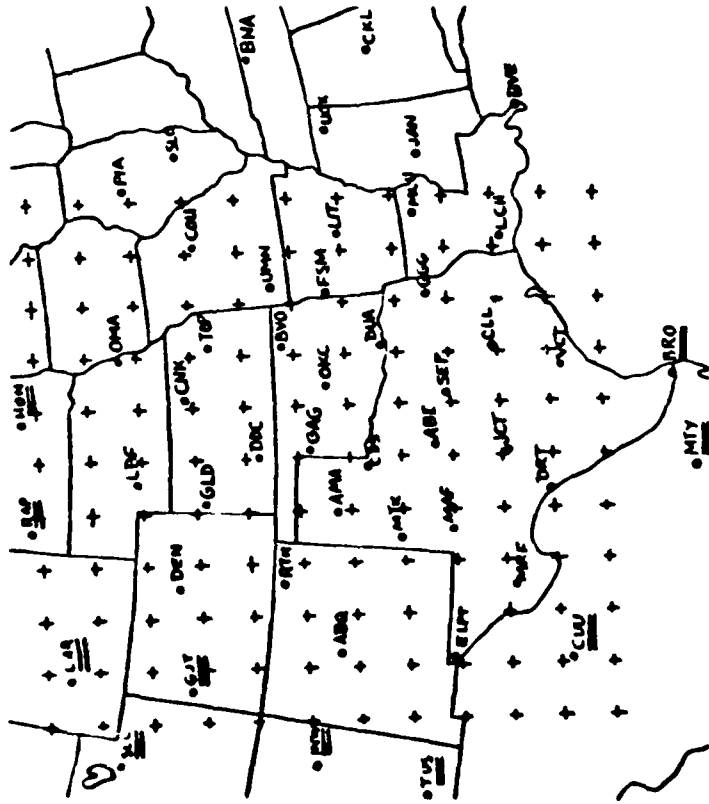
Fig.2: Time-averaged 700 mb height
10-11 April 1979. Subjective corrections
shown as dashed lines.

71
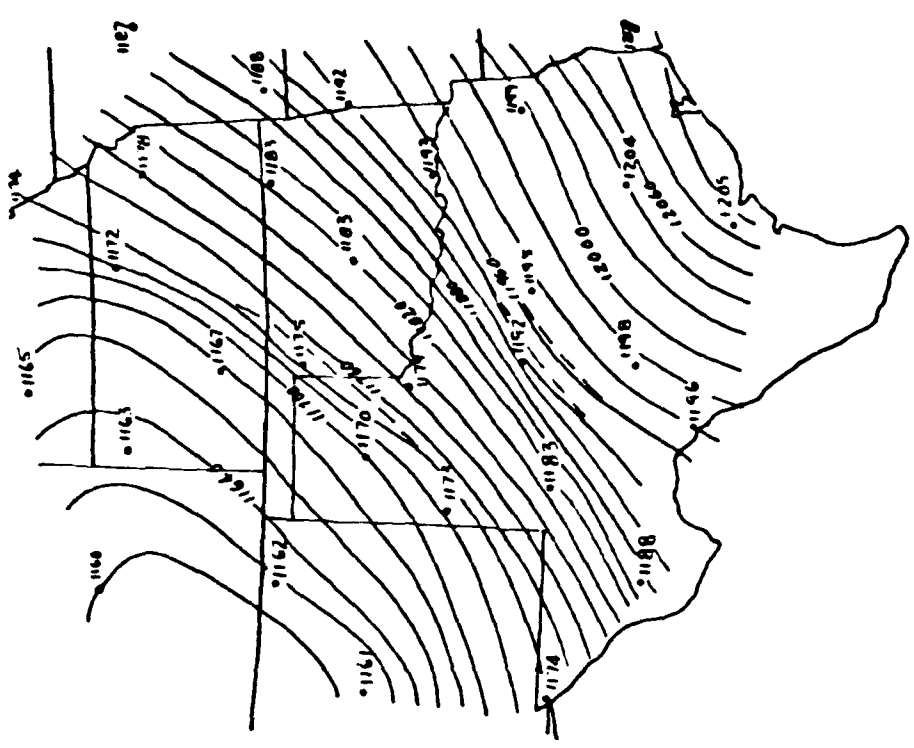
Fig.4: Time-averaged 200 mb height 10-11 April 1979. Subjective corrections shown as dashed lines.
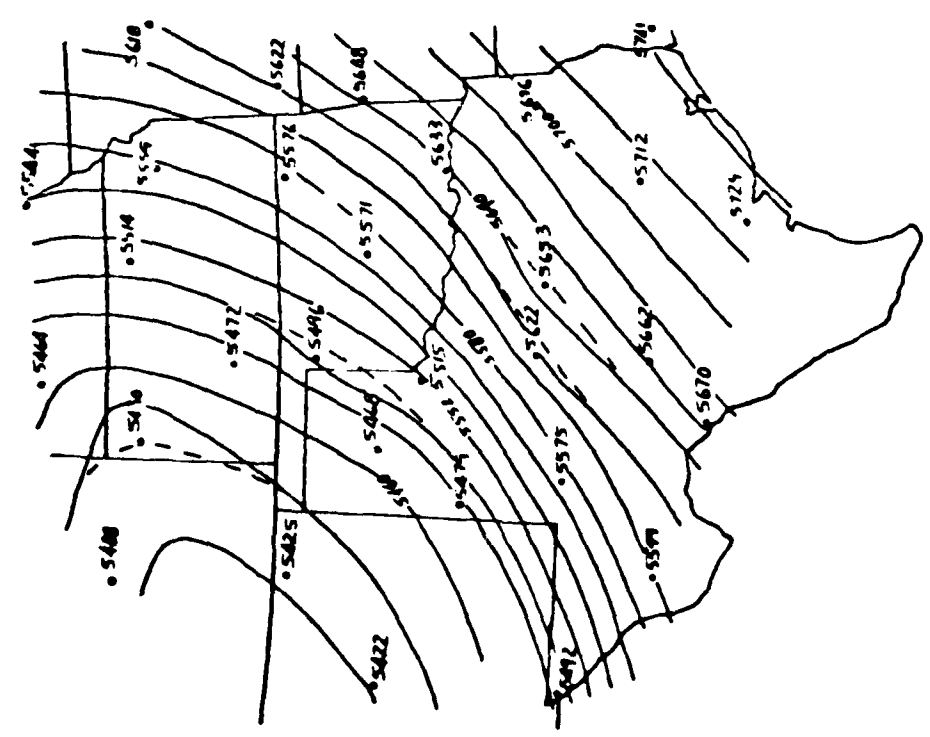
Fig.3: Time-averaged 500 mb height 10-11 April 1979. Subjective corrections shown as dashed lines.

72
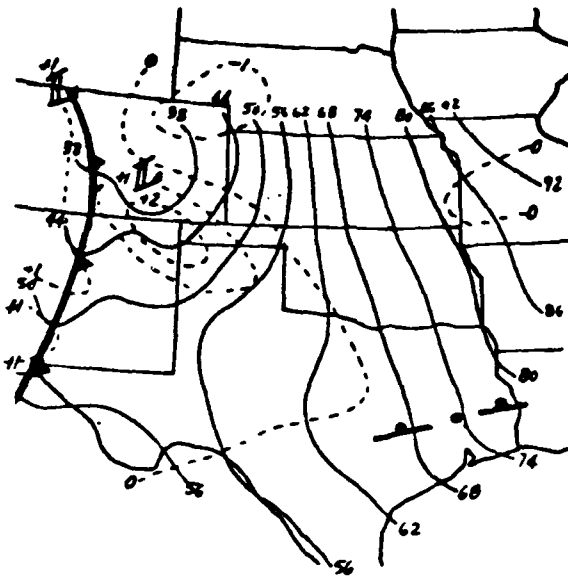
Fig.5a: Surface fronts and alt. setting (10^2in Hg: solid) and quasi-geostrophic surface omega (μb/s: dashed) at 1200 GMT 10 April 1979.

Fig.5b: Nephanalysis at 1200 GMT 10 April 1979 from GOES IR data, with convective and sandstorm activity from radar and hourlies. Ceilings (scalloped).
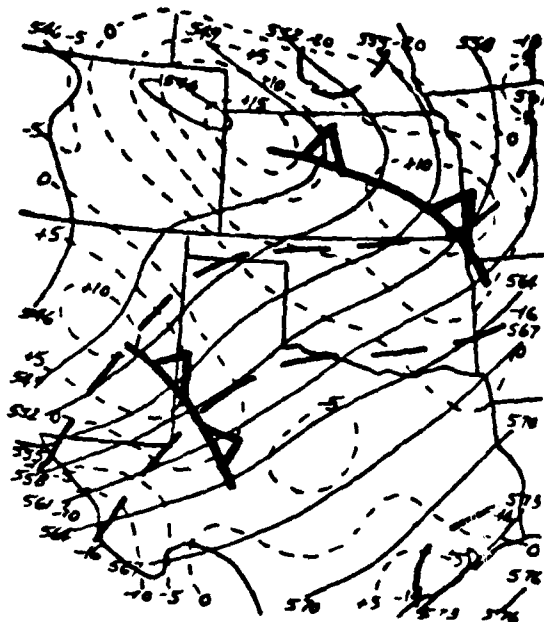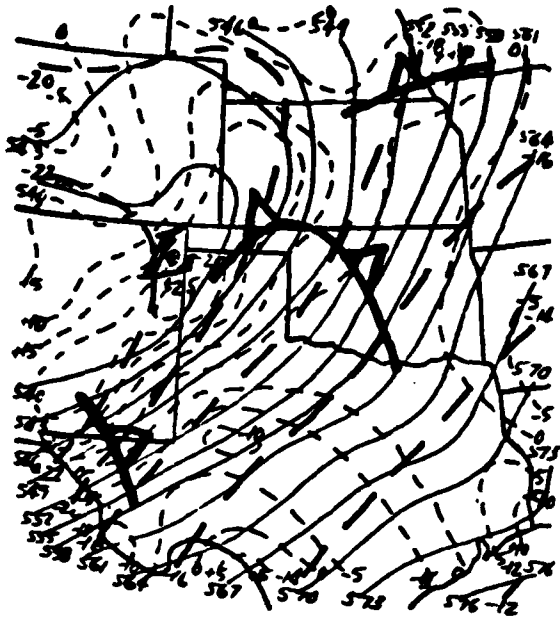
Fig.5c: 500 mb height (m: solid lines), temperature (C: heavy dashed), and relative vorticity ($10^{-5}s^{-1}$: light dashed) at 1200 GMT. Minor wave trough ( ).
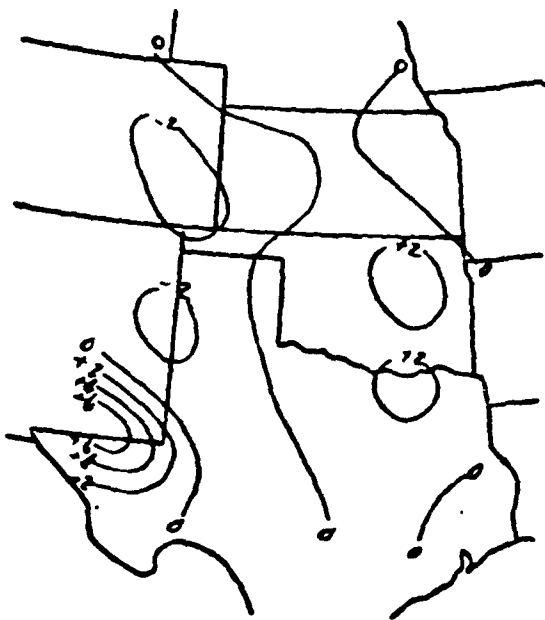
Fig.5d: 500 mb quasi-geostrophic omega (µb/s) at 1200 GMT 10 April 1979.
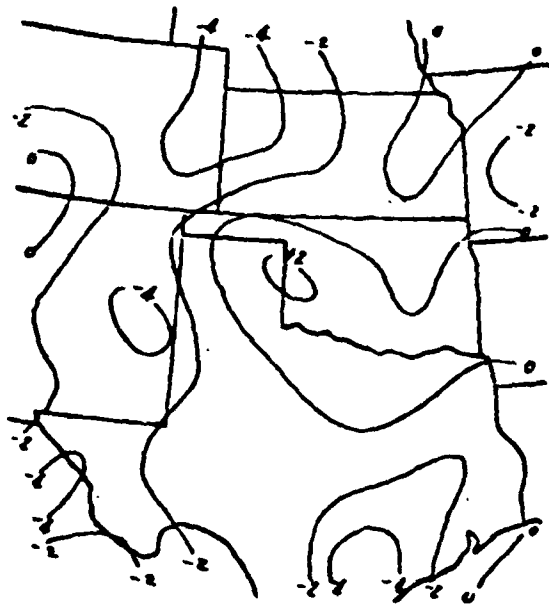
Fig.5e: 500mb kinematically computed omega (µb/s) corrected by O'Brien's method, at 1200 GMT 10 April 1979.

74
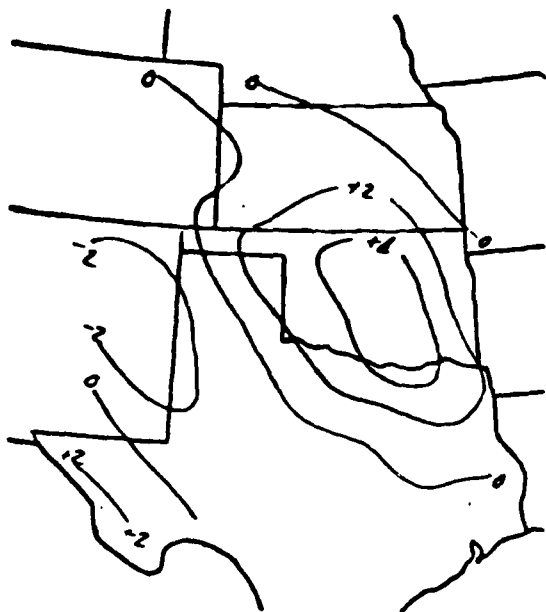
Fig.5f: 500mb omega (μb/s) due to differential vorticity advection (F1), at 1200 GMT 10 April 1979.
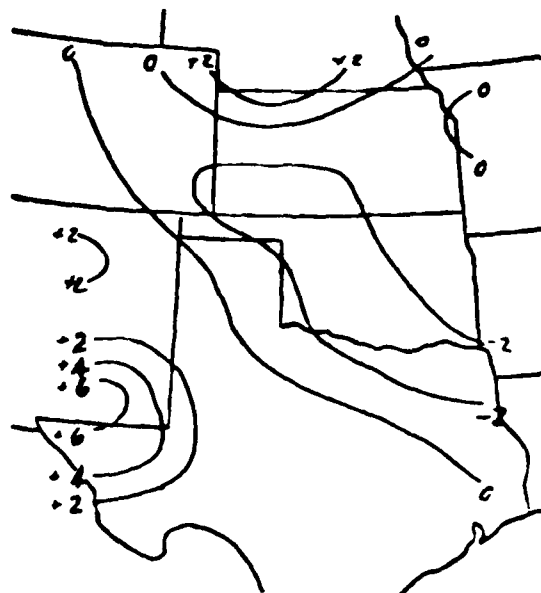
Fig.5g: 500mb omega (μb/s) due to the laplacian of temperature advection (F2), at 1200 GMT 10 April 1979.
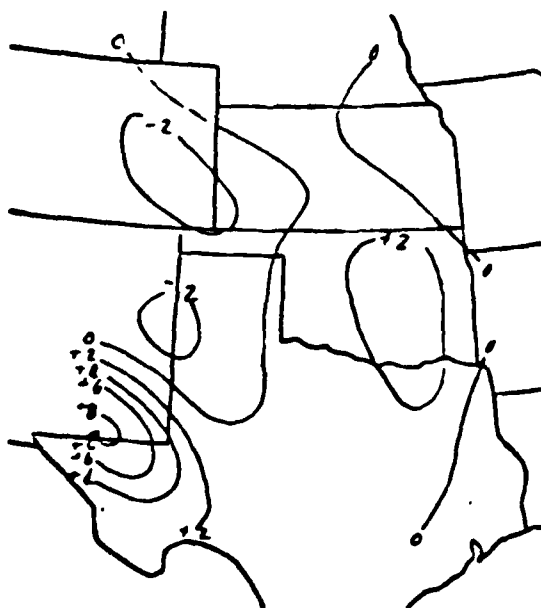
Fig.5h: 500mb omega (μb/s) due to the advection of vorticity (2ζ+f) by the thermal wind (F3), at 1200 GMT 10 April 1979.
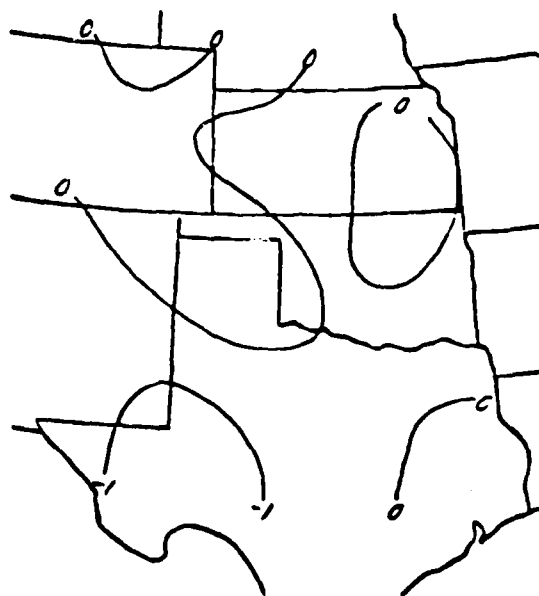
Fig.5i: 500mb omega (μb/s) due to Wiin-Nielsen's deformation function (F4), at 1200 GMT 10 April 1979.
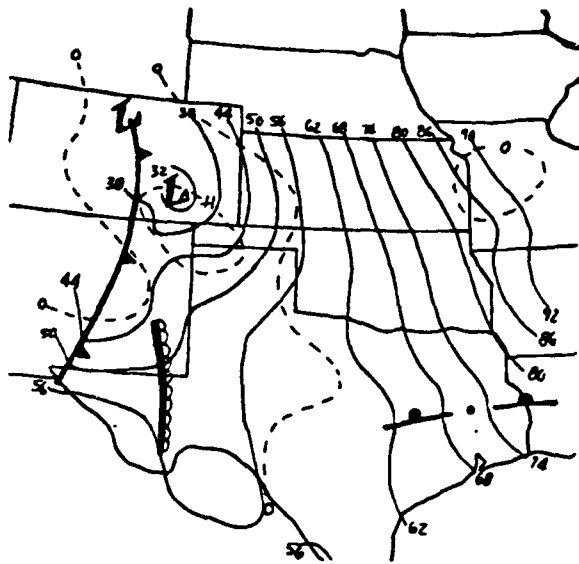
Fig.6a: Surface fronts and alt. setting (10^2 in Hg: solid) and quasi-geostrophic surface omega (μb/s: dashed) at 1500 GMT 10 April 1979. Dry line (   ).

Fig.6b: Nephanalysis at 1500 GMT 10 April 1979 from GOES video data, with convective and sandstorm activity from radar and hourlies. Ceilings (scalloped).
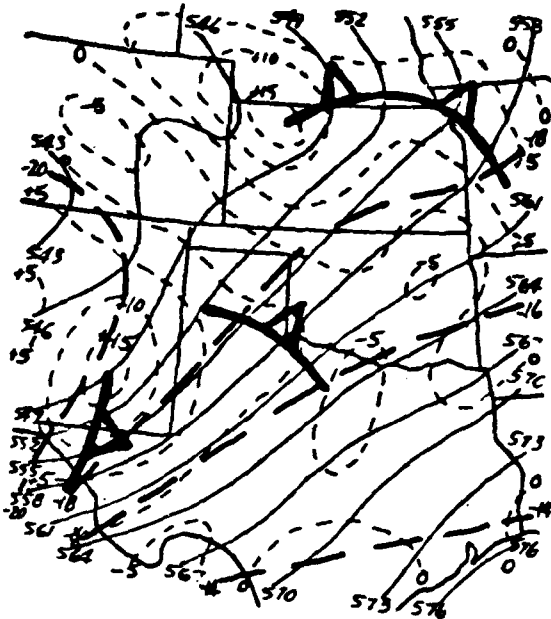
Fig.6c: 500 mb height (m:
solid lines), temperature (C: heavy
dashed), and relative vorticity
($10^{-5}s^{-1}$: light dashed) at 1500 GMT.

Minor wave trough (⌃⌃).

Fig.6d: 500 mb quasi-
geostrophic omega (μb/s) at
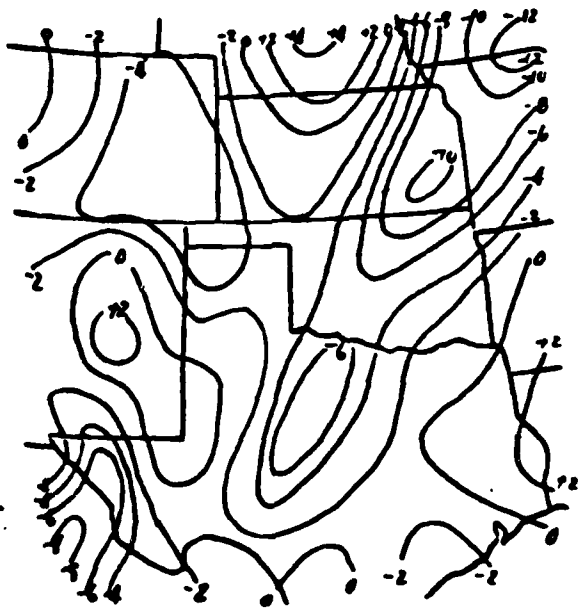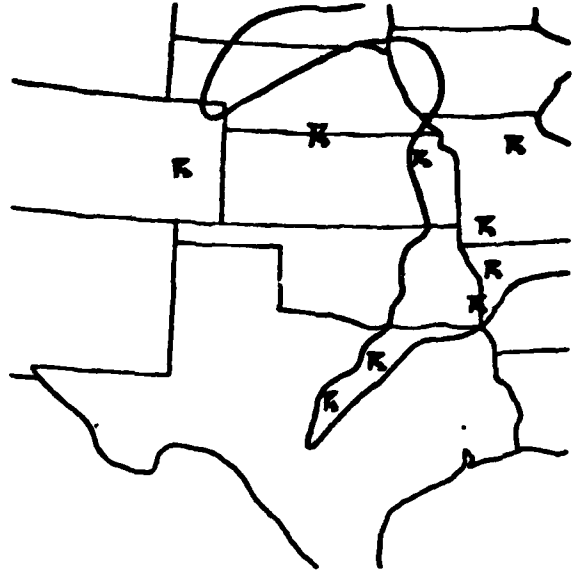1500 GMT 10 April 1979.
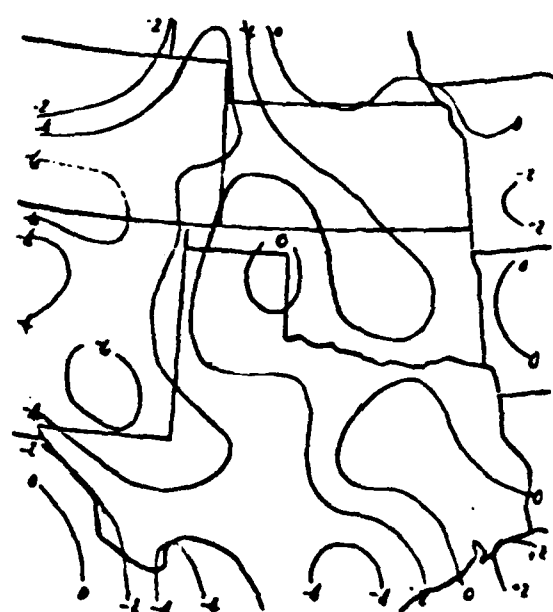
Fig.6e: 500mb kinematically
computed omega (μb/s) corrected by
O'Brien's method, at 1500 GMT
10 April 1979.

77
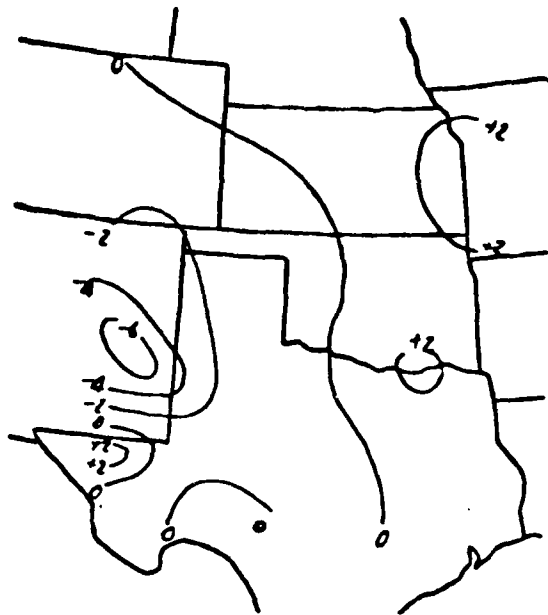
Fig.6f: 500mb omega (μb/s)
due to differential vorticity
advection (F1), at 1500 GMT
10 April 1979.

Fig.6g: 500mb omega (μb/s)
due to the laplacian of
temperature advection (F2), at
1500 GMT 10 April 1979.

Fig.6h: 500mb omega (μ b/s)
due to the advection of vorticity
(2ζ+f) by the thermal wind (F3),
at 1500 GMT 10 April 1979.
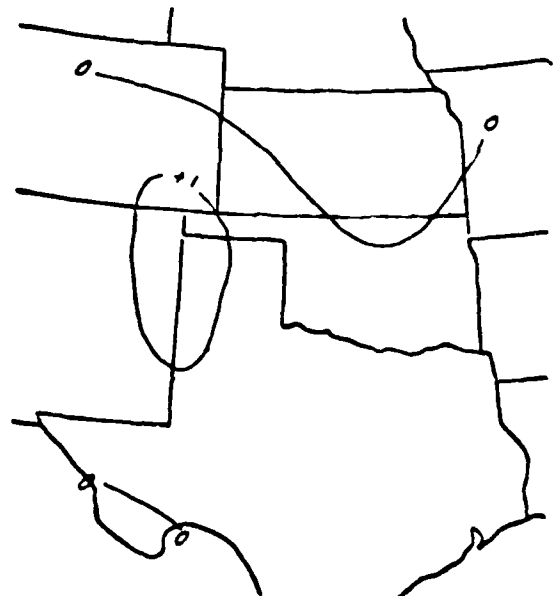
Fig.6i: 500mb omega (μb/s)
due to Wiin-Nielsen's deformation
function (F4), at 1500 GMT
10 April 1979.

78
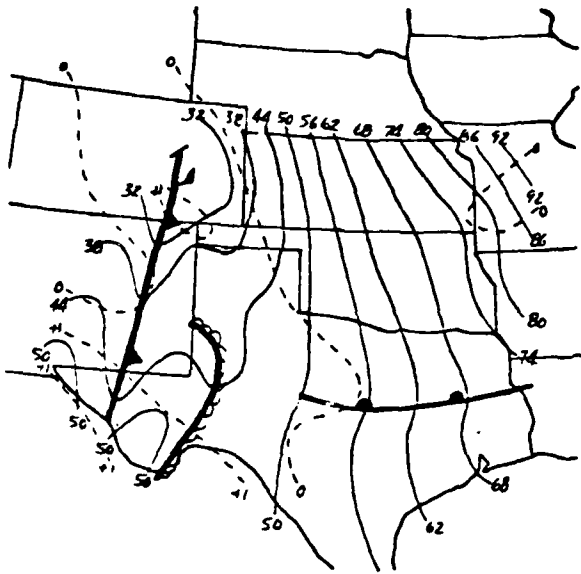
Fig. 7a: Surface fronts and   Fig. 7b: Nephanalysis at 1800
alt. setting (10^2in Hg: solid)   GMT 10 April 1979 from GOES video
and quasi-geostrophic surface   data, with convective and sandstorm
omega (μb/s: dashed) at 1800 GMT   activity from radar and hourlies.
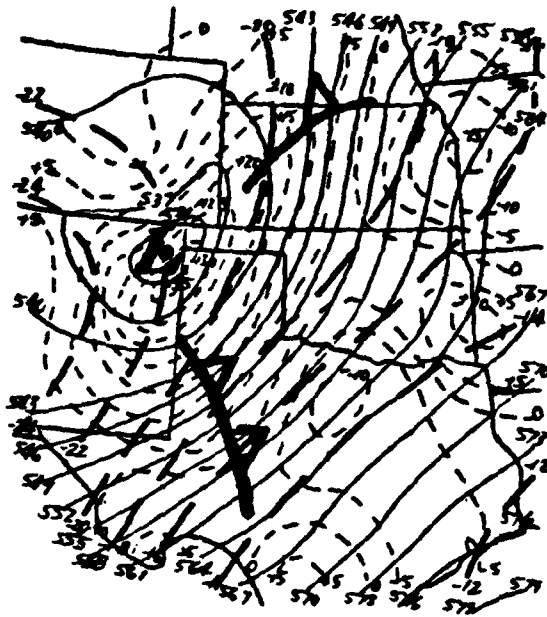10 April 1979.   Dry line (━━━)   Ceilings (scalloped).
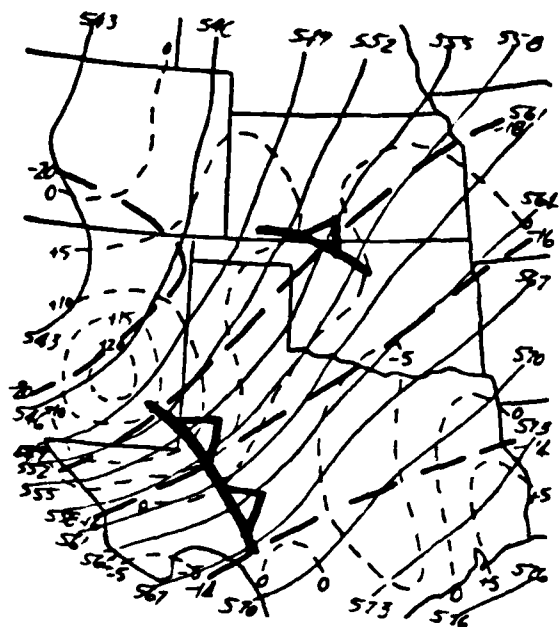
Fig.7c: 500 mb height (m:
solid lines), temperature (C: heavy
dashed), and relative vorticity
$(10^{-5}s^{-1}$: light dashed) at 1800 GMT.
Minor wave trough (⌃⌃).
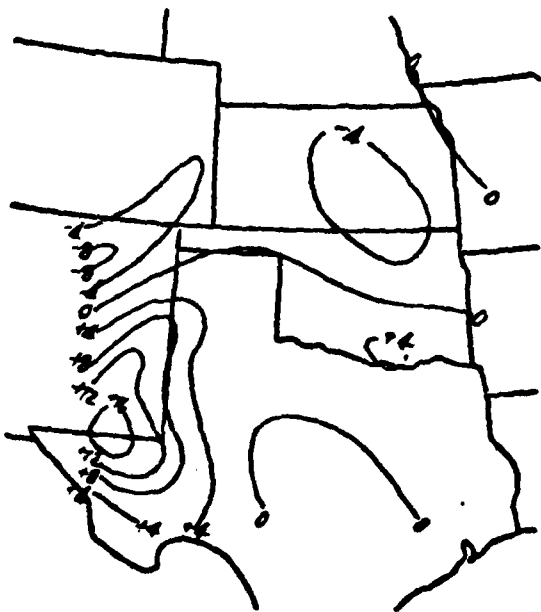

Fig.7d: 500 mb quasi-
geostrophic omega (µb/s) at
1800 GMT 10 April 1979.
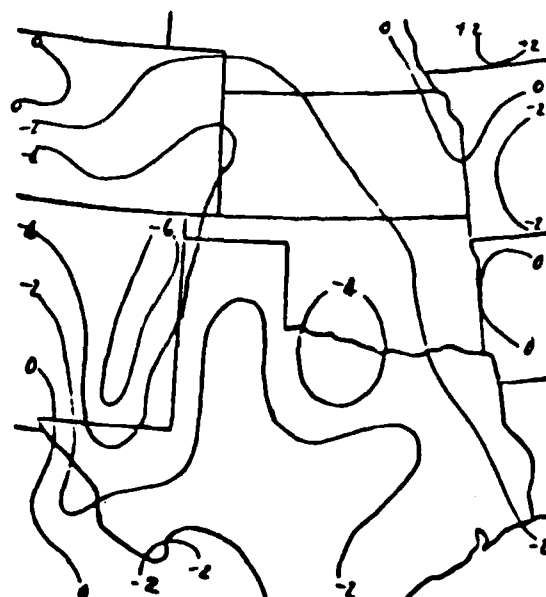
Fig.7e: 500mb kinematically
computed omega (µb/s) corrected by
O'Brien's method, at 1800 GMT
10 April 1979.

Fig.7f: 500mb omega (µb/s)
due to differential vorticity
advection (F1), at 1800 GMT
10 April 1979.

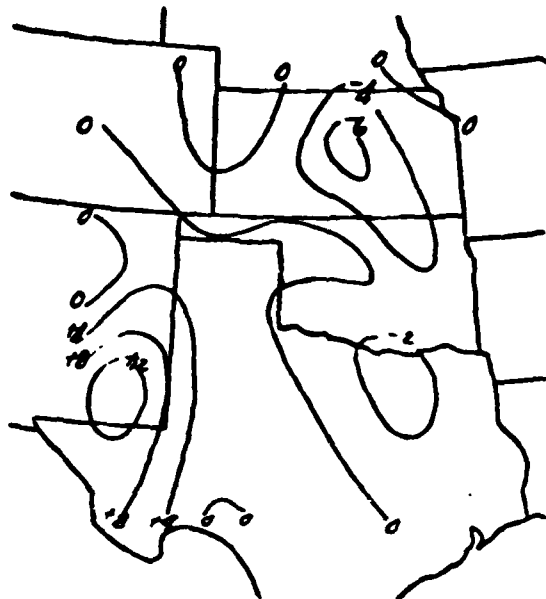Fig.7g: 500mb omega (µb/s)
due to the laplacian of
temperature advection (F2', at
1800 GMT 10 April 1979.

Fig.7h: 500mb omega (µb/s)
due to the advection of vorticity
(2ζ+f) by the thermal wind (F3),
at 1800 GMT 10 April 1979.

Fig.7i: 500mb omega (µb/s)
due to Wiin-Nielsen's deformation
function (F4), at 1800 GMT
10 April 1979.
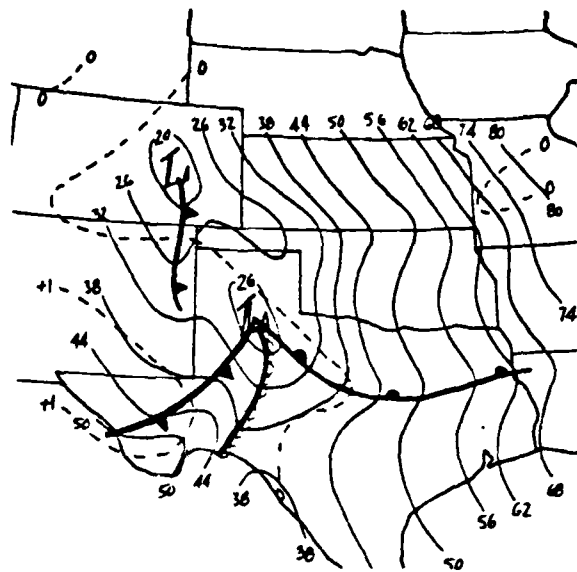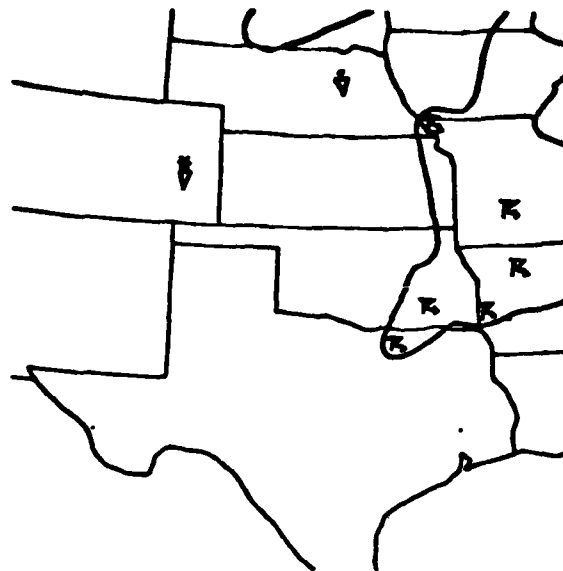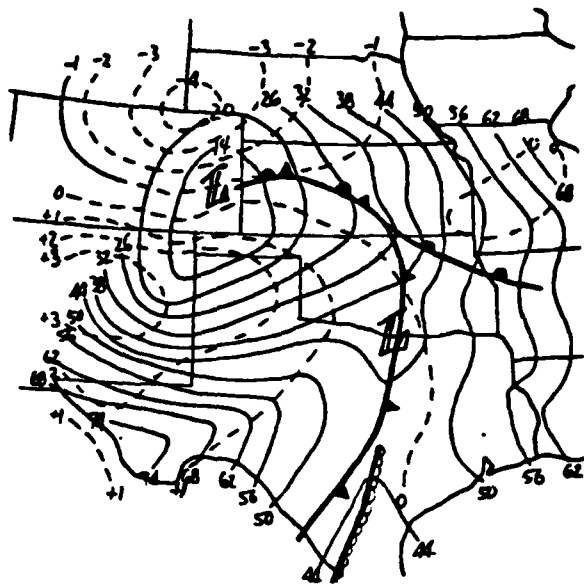
Fig. 8a: Surface fronts and
alt. setting (10^2 in Hg: solid)
and quasi-geostrophic surface
omega (μb/s: dashed) at 2100 GMT
10 April 1979. Dry line (━━━).
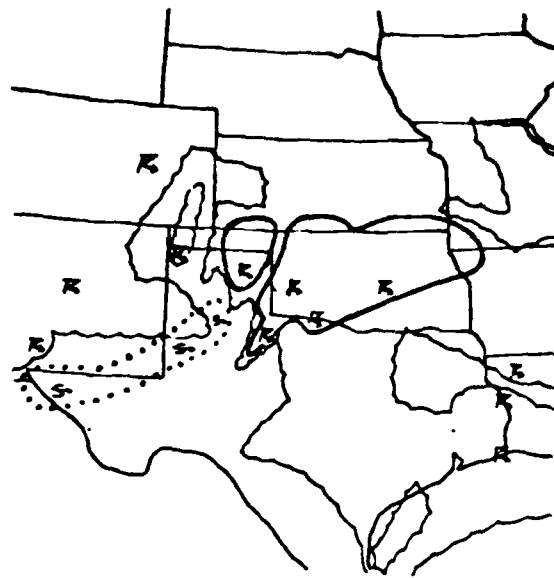
Fig. 8b: Nephanalysis at 2100
GMT 10 April 1979 from GOES video
data, with convective and sandstorm
activity from radar and hourlies.
Ceilings (scalloped) and cold-
est clouds (solid outline).
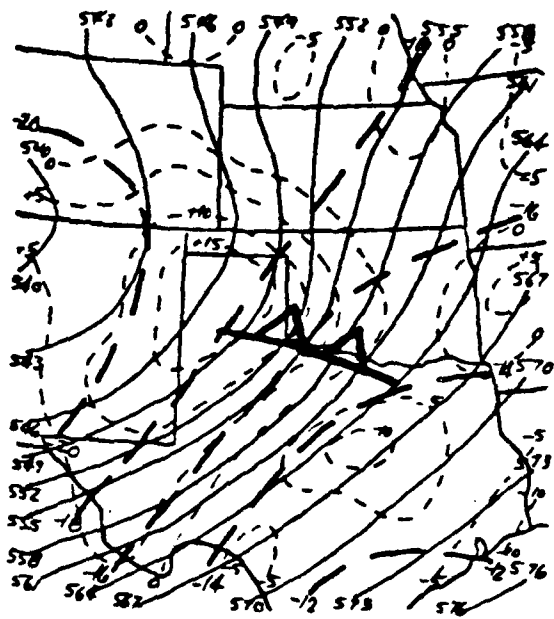
Fig.8c: 500 mb height (m: solid lines), temperature (C: heavy dashed), and relative vorticity ($10^{-5}s^{-1}$: light dashed) at 2100 GMT. Minor wave trough ( ).

Fig.8d: 500 mb quasi-geostrophic omega (µb/s) at 2100 GMT 10 April 1979.

Fig.8e: 500mb kinematically computed omega (µb/s) corrected by O'Brien's method, at 2100 GMT 10 April 1979.

Fig.8f: 500mb omega (μb/s)
due to differential vorticity
advection (F1), at 2100 GMT
10 April 1979.

Fig.8g: 500mb omega (μb/s)
due to the laplacian of
temperature advection (F2), at
2100 GMT 10 April 1979.

Fig.8h: 500mb omega (μb/s)
due to the advection of vorticity
(2ζ+f) by the thermal wind (F3),
at 2100 GMT 10 April 1979.
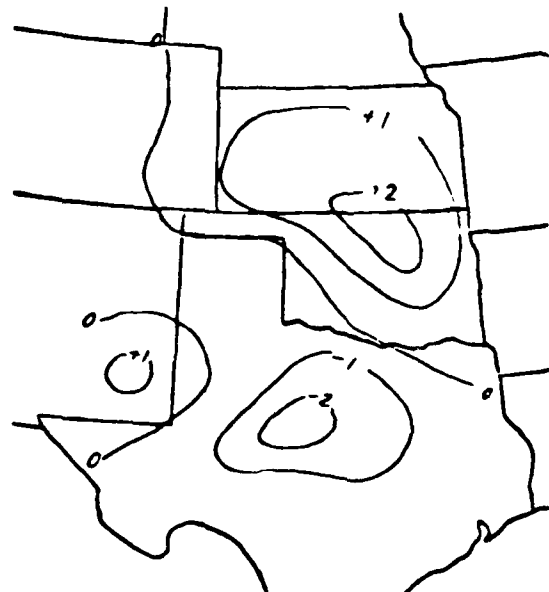
Fig.8i: 500mb omega (μb/s)
due to Wiin-Nielsen's deformation
function (F4), at 2100 GMT
10 April 1979.
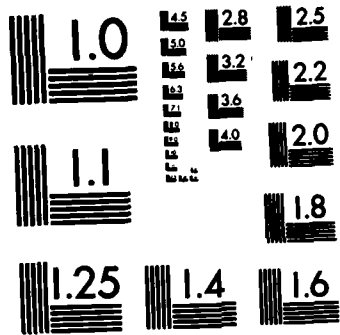
MICROCOPY RESOLUTION TEST CHART

NATIONAL BUREAU OF STANDARDS-1963-A
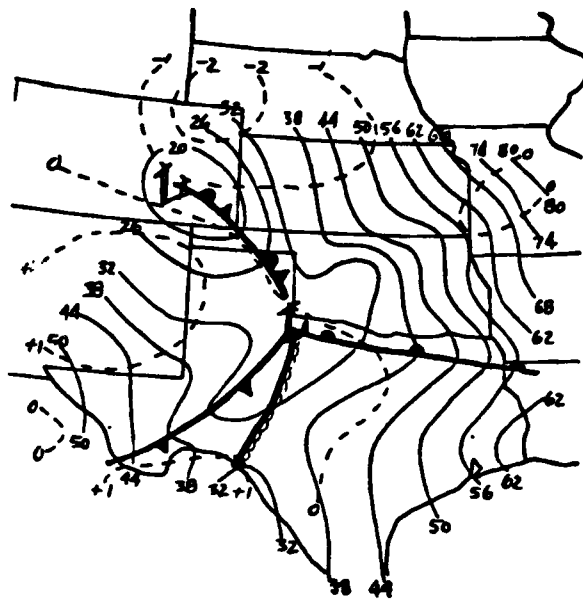
Fig.9a: Surface fronts and alt. setting (10^2in Hg: solid) and quasi-geostrophic surface omega (μb/s: dashed) at 0000 GMT 11 April 1979. Dry line ( ).
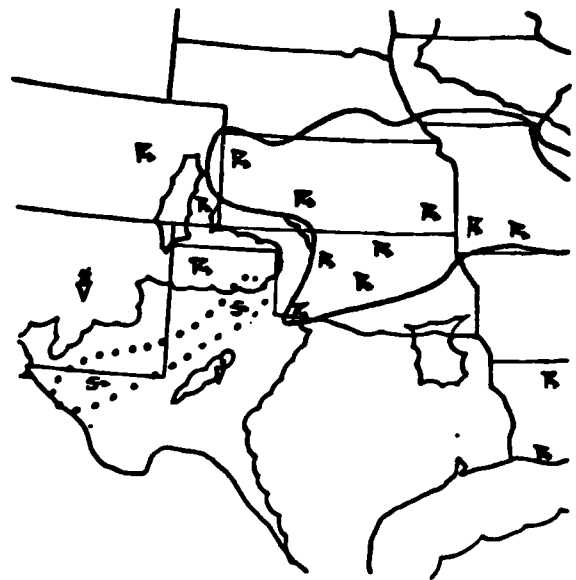
Fig.9b: Nephanalysis at 0000 GMT 11 April 1979 from GOES video data, with convective and sandstorm activity from radar and hourlies. Ceilings (scalloped) and coldest clouds (solid outline).
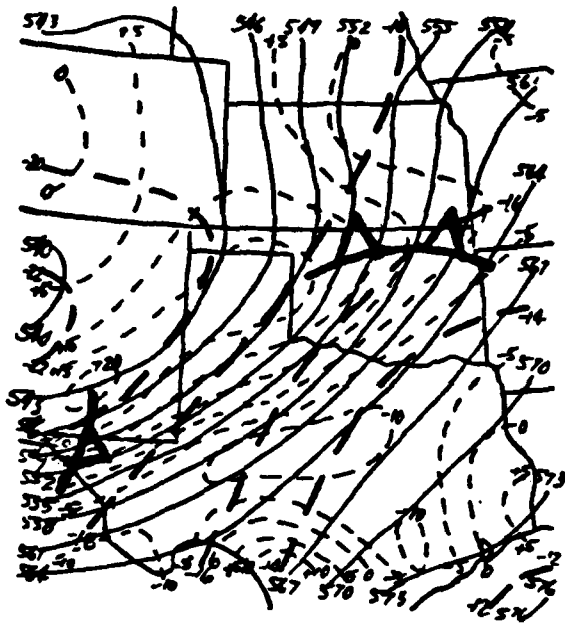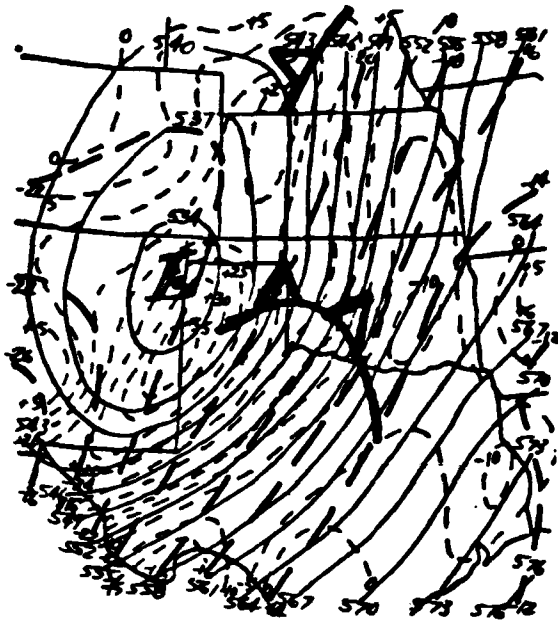
Fig.9C: 500 mb height (m: solid lines), temperature (C: heavy dashed), and relative vorticity ($10^{-5}s^{-1}$: light dashed) at 0000 GMT. Minor wave trough (⌃⌃).
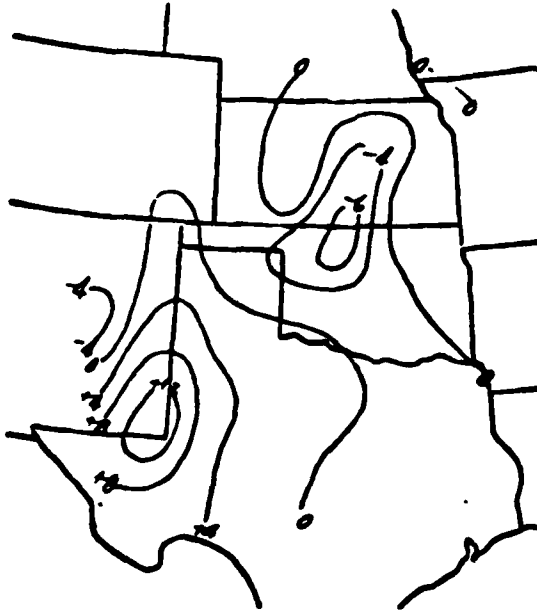

Fig.9d: 500 mb quasi-geostrophic omega (μb/s) at 0000 GMT 11 April 1979.
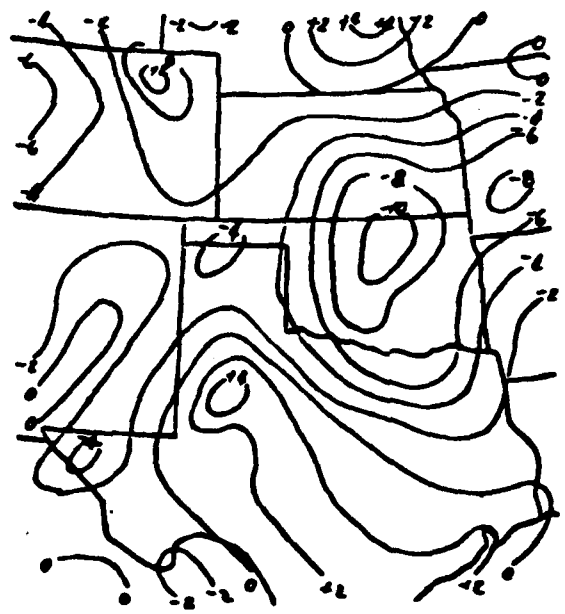
Fig.9e: 500mb kinematically computed omega (μb/s) corrected by O'Brien's method, at 0000 GMT 11 April 1979.

86

Fig.9f: 500mb omega (μb/s) due to differential vorticity advection (F1), at 0000 GMT 11 April 1979.
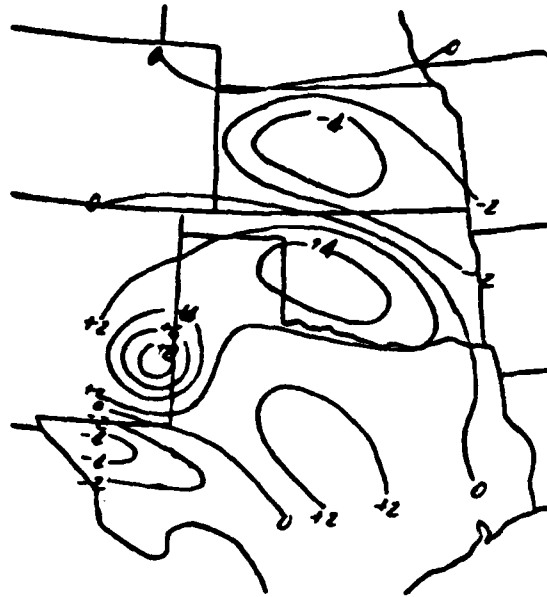
Fig.9g: 500mb omega (μb/s) due to the laplacian of temperature advection (F2), at 0000 GMT 11 April 1979.
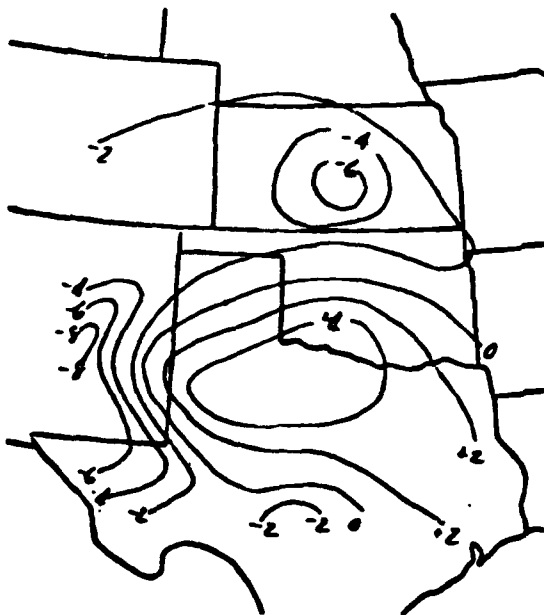
Fig.9h: 500mb omega (μ b/s) due to the advection of vorticity (2ζ+f) by the thermal wind (F3), at 0000 GMT 11 April 1979.
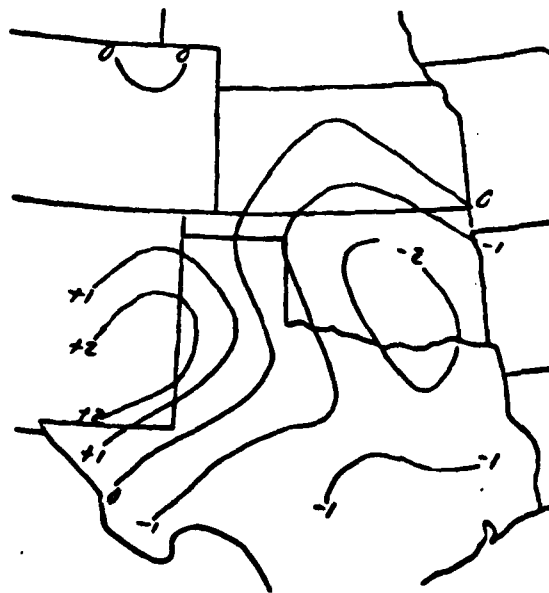
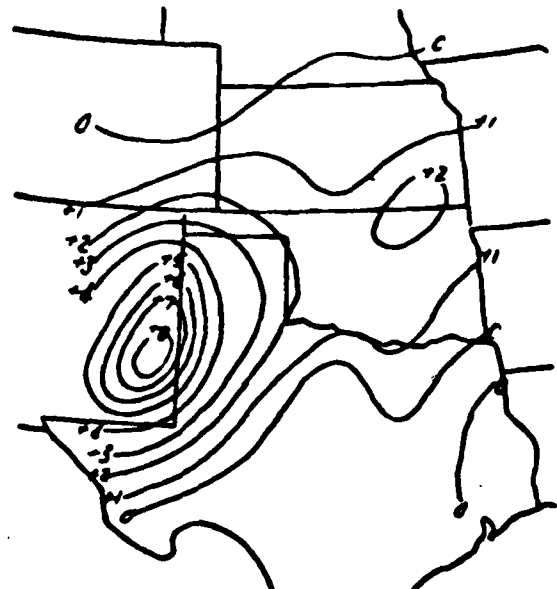Fig.9i: 500mb omega (μb/s) due to Wiin-Nielsen's deformation function (F4), at 0000 GMT 11 April 1979.

87
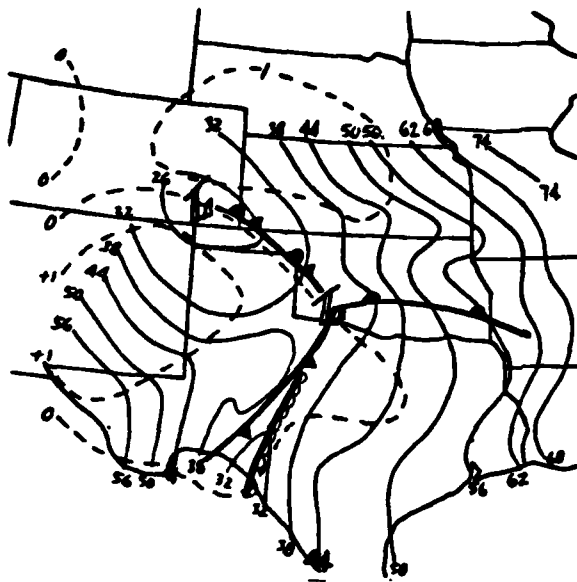
Fig.10a: Surface fronts and   Fig.10b: Nephanalysis at 0300
alt. setting (10^2in Hg: solid)   GMT 11 April 1979 from GOES IR
and quasi-geostrophic surface   data, with convective and sandstorm
omega (μb/s: dashed) at 0300 GMT   activity from radar and hourlies.
11 April 1979.   Dry line (⟍).Ceilings (scalloped) and cold-
est clouds (solid outline).
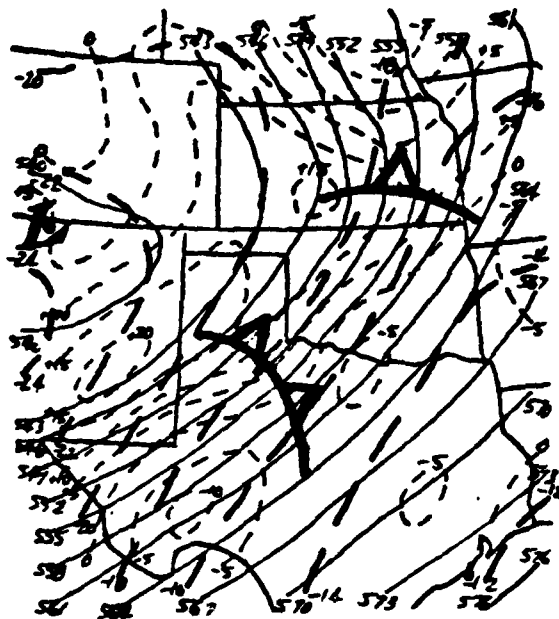
Fig.10c: 500 mb height (m: solid lines), temperature (C: heavy dashed), and relative vorticity ($10^{-5}s^{-1}$: light dashed) at 0300 GMT. Minor wave trough (⌂⌂).
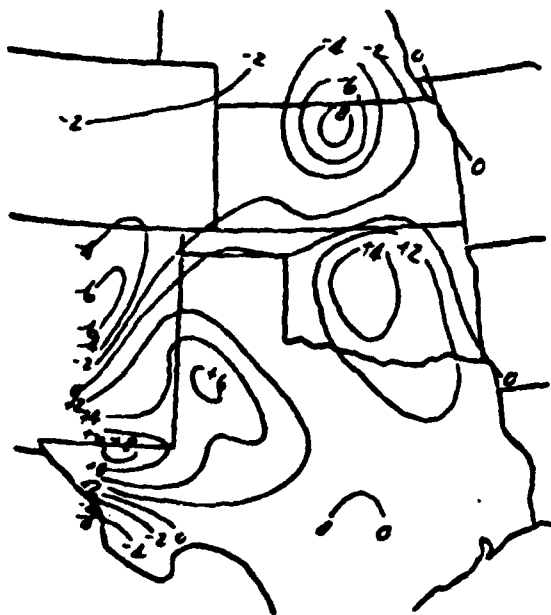
Fig.10d: 500 mb quasi-geostrophic omega (μb/s) at C300 GMT 11 April 1979.
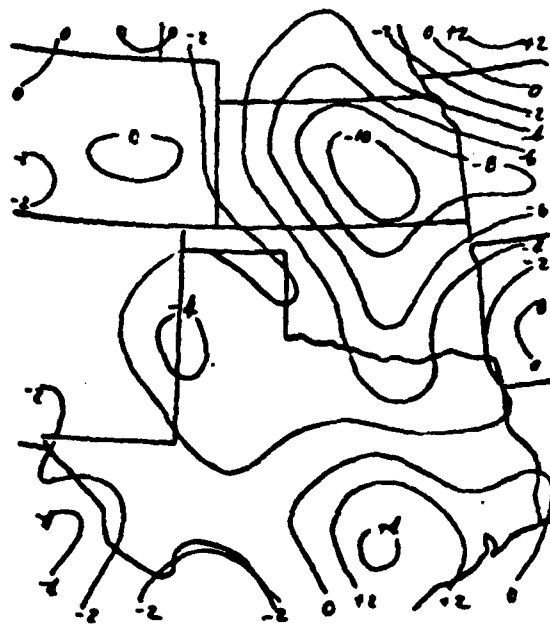
Fig.10e: 500mb kinematically computed omega (μb/s) corrected by O'Brien's method, at 0300 GMT 11 April 1979.

Fig.10f: 500mb omega (μb/s)
due to differential vorticity
advection (F1), at 0300 GMT
11 April 1979.
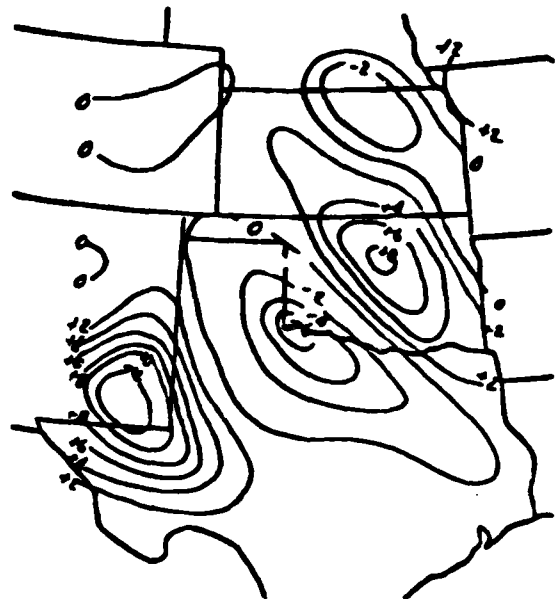
Fig.10g: 500mb omega (μb/s)
due to the laplacian of
temperature advection (F2), at
0300 GMT 11 April 1979.
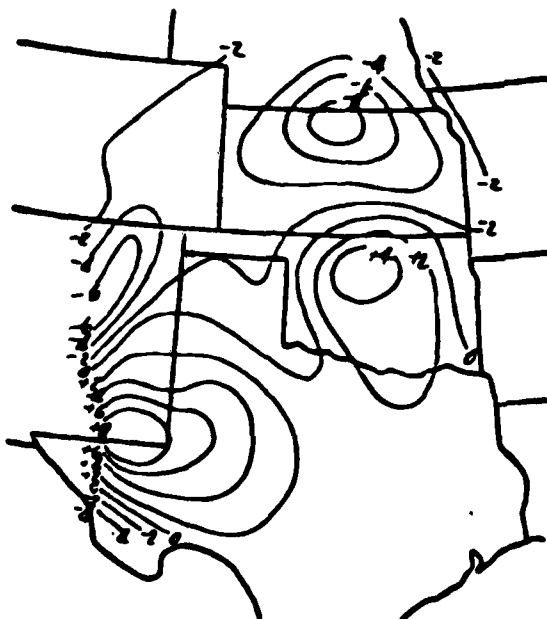
Fig.10h: 500mb omega (μ b/s)
due to the advection of vorticity
(2ζ+f) by the thermal wind (F3),
at 0300 GMT 11 April 1979.

Fig.10i: 500mb omega (μb/s)
due to Wiin-Nielsen's deformation
function (F4), at 0300 GMT
11 April 1979.
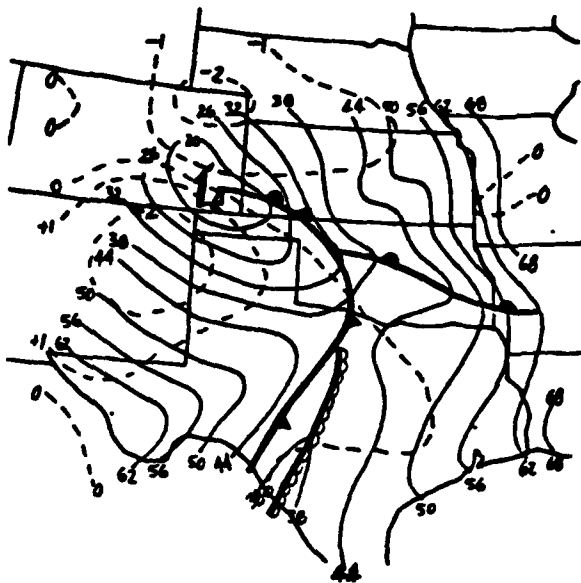
Fig.11a: Surface fronts and alt. setting (10^2 in Hg: solid) and quasi-geostrophic surface omega (μb/s: dashed) at 0600 GMT 11 April 1979. Dry line (⟍⟍⟍).

Fig.11b: Nephanalysis at 0600 GMT 11 April 1979 from GOES IR data, with convective and sandstorm activity from radar and hourlies. Ceilings (scalloped) and coldest clouds (solid outline).

Fig.11c: 500 mb height (m: solid lines), temperature (C: heavy dashed), and relative vorticity $(10^{-5}s^{-1}$: light dashed) at 0600 GMT. Minor wave trough ( ).

Fig.11d: 500 mb quasi-geostrophic omega (µb/s) at 0600 GMT 11 April 1979.

Fig.11e: 500mb kinematically computed omega (µb/s) corrected by O'Brien's method, at 0600 GMT 11 April 1979.

92

Fig.11f: 500mb omega (ub/s)
due to differential vorticity
advection (F1), at 0600 GMT
11 April 1979.

Fig.11g: 500mb omega (ub/s)
due to the laplacian of
temperature advection (F2), at
0600 GMT 11 April 1979.

Fig.11h: 500mb omega (u b/s)
due to the advection of vorticity
(2ζ+f) by the thermal wind (F3),
at 0600 GMT 11 April 1979.

Fig.11i: 500mb omega (ub/s)
due to Wiin-Nielsen's deformation
function (F4), at 0600 GMT
11 April 1979.
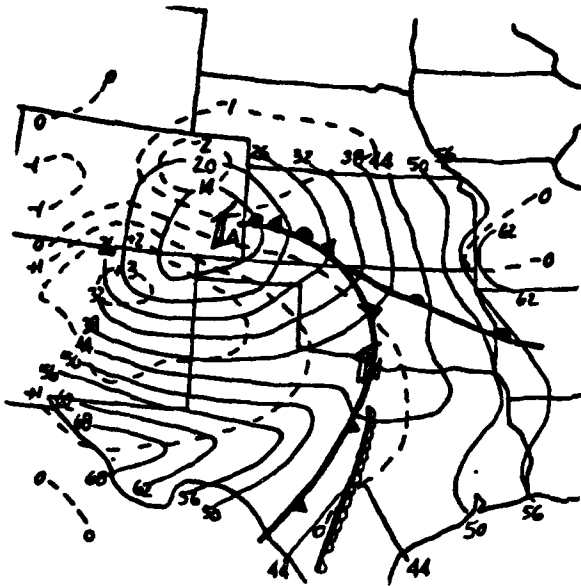
Fig.12a: Surface fronts and   Fig.12b: Nephanalysis at 0900
alt. setting (10^2in Hg: solid)   GMT 11 April 1979 from GOES IR
and quasi-geostrophic surface   data, with convective and sandstorm
omega (µb/s: dashed) at 0900 GMT   activity from radar and hourlies.
11 April 1979.   Dry line (⬛⬛⬛⬛). Coldest clouds (solid line).

Fig.12c: 500 mb height (m: solid lines), temperature (C: heavy dashed), and relative vorticity ($10^{-5} s^{-1}$: light dashed) at 0900 GMT. Minor wave trough (⌃⌃).

Fig.12d: 500 mb quasi-geostrophic omega (μb/s) at 0900 GMT 11 April 1979.
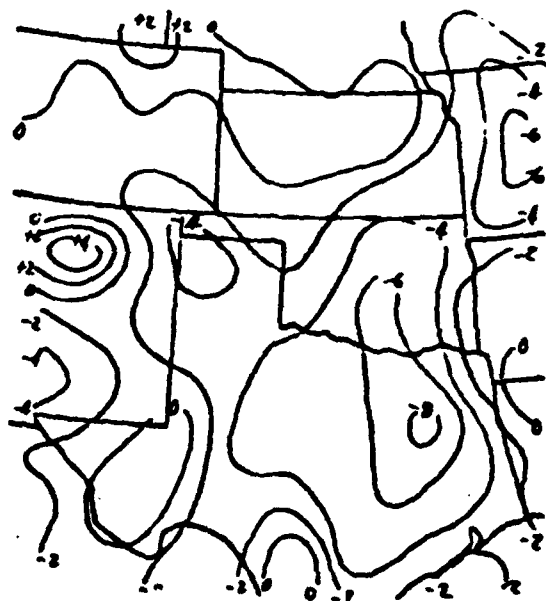
Fig.12e: 500mb kinematically computed omega (μb/s) corrected by O'Brien's method, at 0900 GMT 11 April 1979.

95
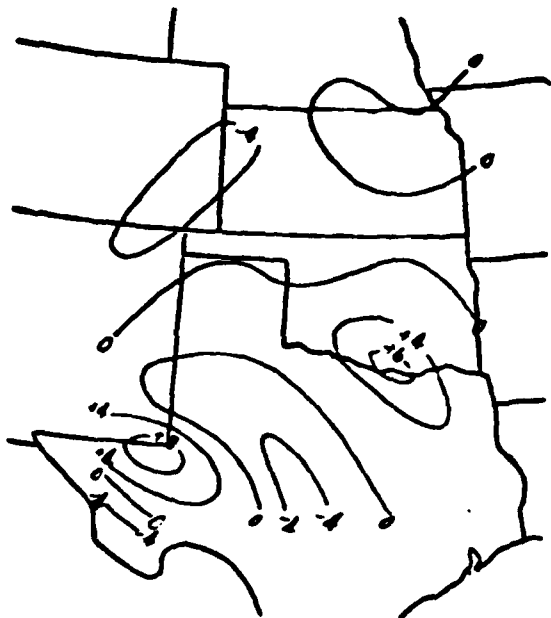
Fig.12f: 500mb omega (µb/s)
due to differential vorticity
advection (F1), at 0900 GMT
11 April 1979.

Fig.12g: 500mb omega (µb/s)
due to the laplacian of
temperature advection (F2), at
0900 GMT 11 April 1979.

Fig.12h: 500mb omega (µ b/s)
due to the advection of vorticity
(2ζ+f) by the thermal wind (F3),
at 0900 GMT 11 April 1979.

Fig.12i: 500mb omega (µb/s)
due to Wiin-Nielsen's deformation
function (F4), at 0900 GMT
11 April 1979.

96

Fig.13a: Surface fronts and
alt. setting (10^2 in Hg: solid)
and quasi-geostrophic surface
omega (μb/s: dashed) at 1200 GMT
11 April 1979.   Dry line (⌇⌇⌇⌇).

Fig.13b: Nephanalysis at 1200
GMT 11 April 1979 from GOES IR
data, with convective and sandstorm
activity from radar and hourlies.
Coldest clouds (solid line).

Fig.13c: 500 mb height (m: solid lines), temperature (C: heavy dashed), and relative vorticity ($10^{-5}s^{-1}$: light dashed) at 1200 GMT. Minor wave trough (⌃⌃).

Fig.13d: 500 mb quasi-geostrophic omega (νb/s) at 1200 GMT 11 April 1979.
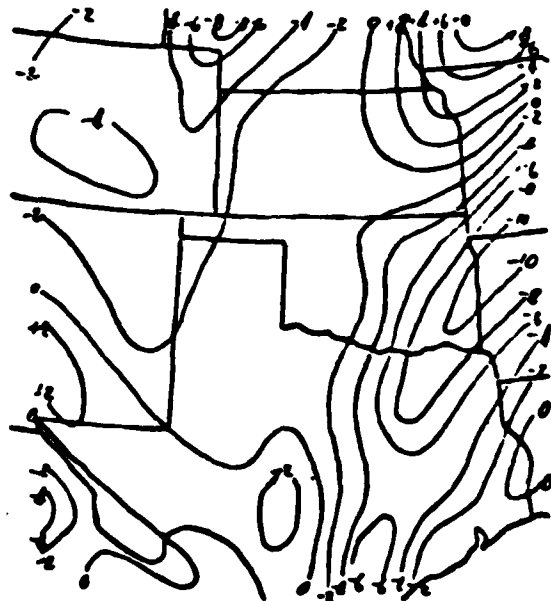
Fig.13e: 500mb kinematically computed omega (νb/s) corrected by O'Brien's method, at 1200 GMT 11 April 1979.

Fig.13f: 500mb omega (μb/s)
due to differential vorticity
advection (F1), at 1200 GMT
11 April 1979.

Fig.13g: 500mb omega (μb/s)
due to the laplacian of
temperature advection (F2), at
1200 GMT 11 April 1979.

Fig.13h: 500mb omega (μ b/s)
due to the advection of vorticity
(2ζ+f) by the thermal wind (F3),
at 1200 GMT 11 April 1979.

Fig.13i: 500mb omega (μb/s)
due to Wiin-Nielsen's deformation
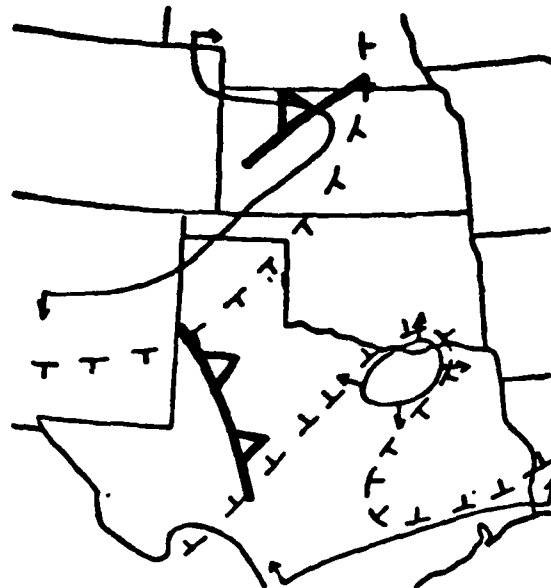function (F4), at 1200 GMT
11 April 1979.

99

Fig.14a: Richardson numbers (see text). Regions at and above 500mb at 1200 GMT 10 April 1979 with $0 < R_i \leqslant .95$ (solid) and $0 < R_i \leqslant .25$(dashed). 500mb trough (⌒⌒).
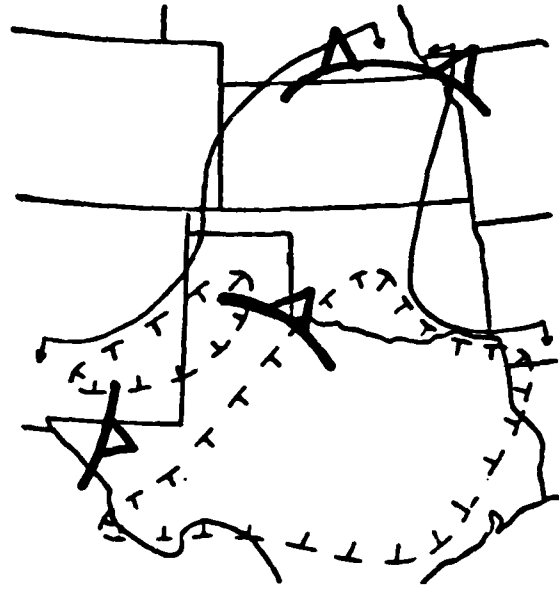
Fig.15a: Richardson numbers (see text). Regions at and above 500mb at 1500 GMT 10 April 1979 with $0 < R_i \leqslant .95$ (solid) and $0 < R_i \leqslant .25$(dashed). 500mb trough (⌒⌒).
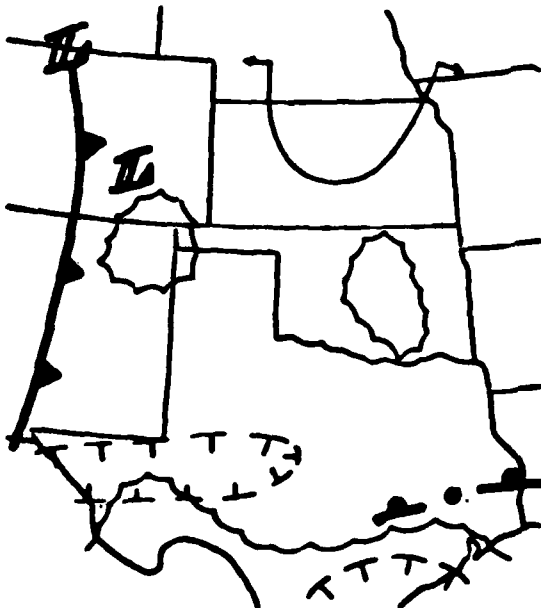
Fig.14b: Regions below 500mb at 1200 GMT 10 April 1979 with $0 < R_i \leqslant .95$(solid) and $0 < R_i \leqslant .25$(dashed). Surface $R_i \leqslant .95$(scalloped). Surface fronts and lows.
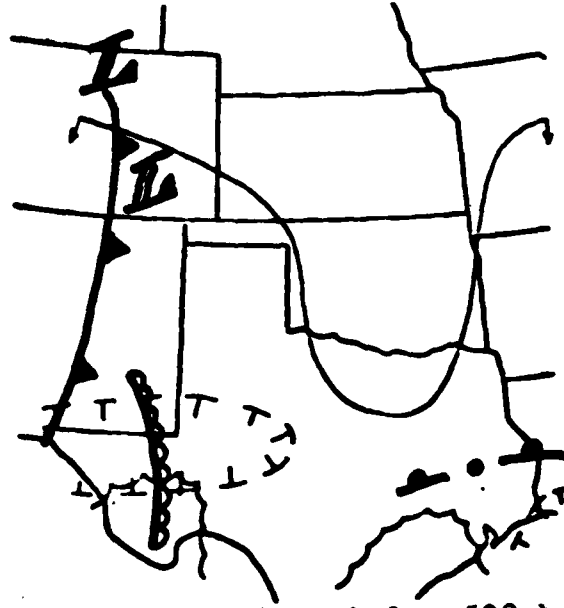
Fig.15b: Regions below 500mb at 1500 GMT 10 April 1979 with $0 < R_i \leqslant .95$(solid) and $0 < R_i \leqslant .25$(dashed). Surface $R_i \leqslant .95$(scalloped). Surface fronts, low, and dry line.

100

Fig.16a: Richardson numbers
(see text). Regions at and
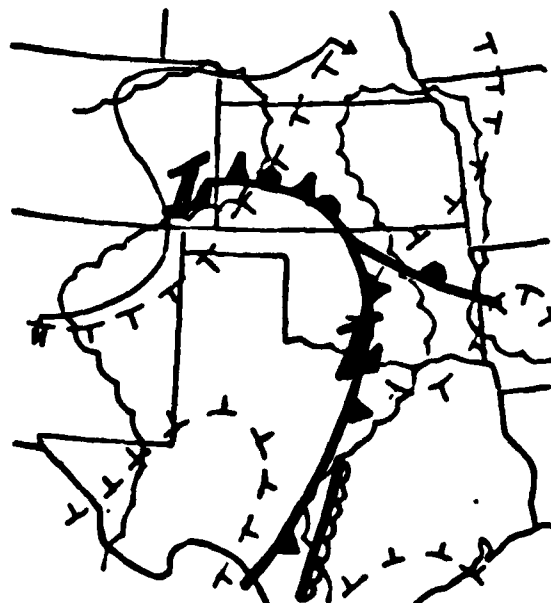above 500mb at 1800 GMT 10
April 1979 with $0<R_i\leq.95$
(solid) and $0<R_i\leq.25$(dashed).
500mb trough (⌒⌒).

Fig.17a: Richardson numbers
(see text). Regions at and
above 500mb at 2100 GMT 10
April 1979 with $0<R_i\leq.95$
(solid) and $0<R_i\leq.25$(dashed).
500mb trough (⌒⌒).
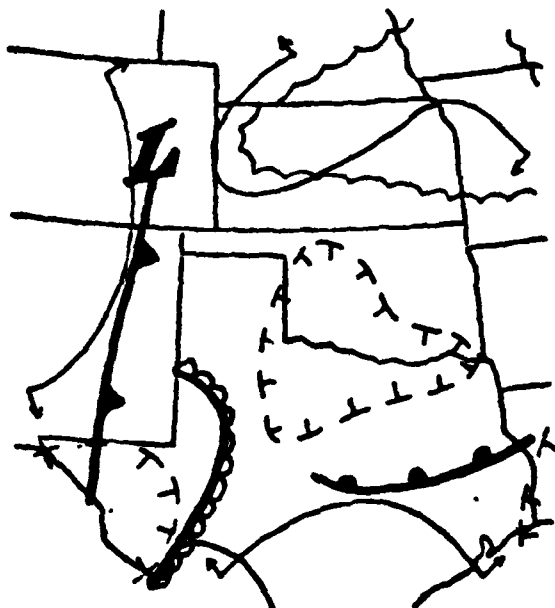
Fig.16b: Regions below 500mb
at 1800 GMT 10 April 1979
with $0<R_i\leq.95$(solid) and
$0<R_i\leq.25$(dashed). Surface
$R_i\leq.95$(scalloped). Surface
fronts, low, and dry line.
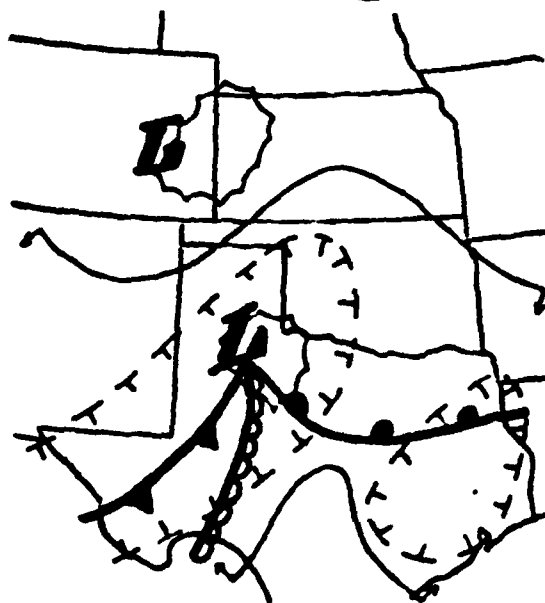
Fig.17b: Regions below 500mb
at 2100 GMT 10 April 1979
with $0<R_i\leq.95$(solid) and
$0<R_i\leq.25$(dashed). Surface
$R_i\leq.95$(scalloped). Surface
fronts, lows, and dry line.
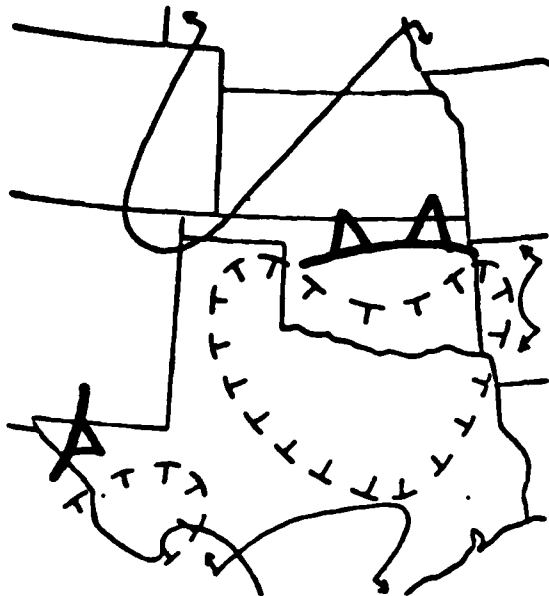
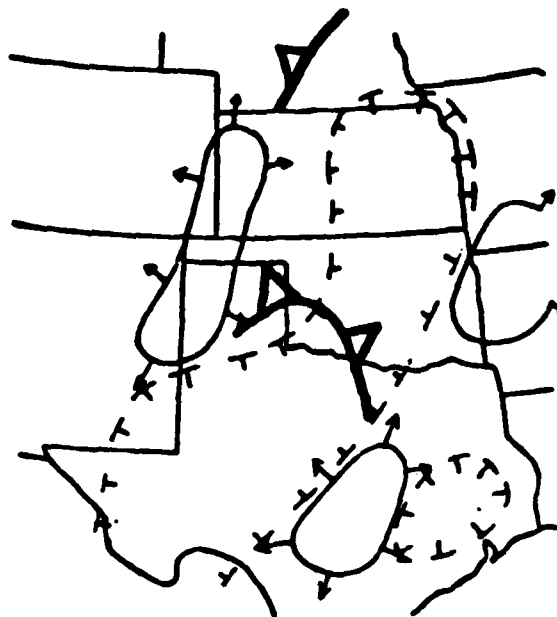Fig.18a: Richardson numbers
(see text). Regions at and
above 500mb at 0000 GMT 11
April 1979 with $0 < R_i \leq .95$
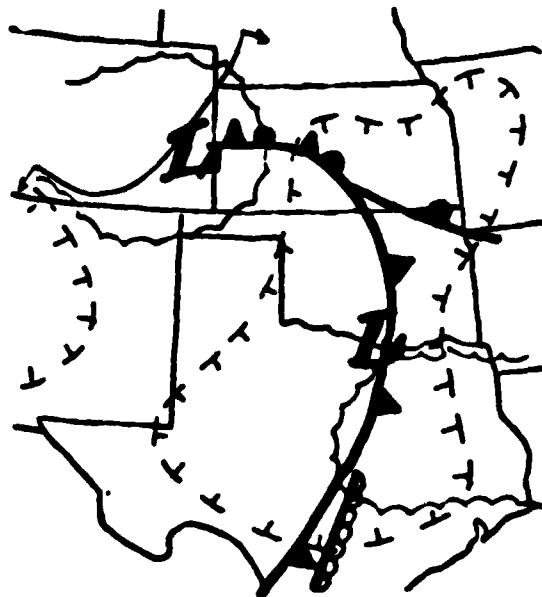(solid) and $0 < R_i \leq .25$(dashed).
500mb trough (⟨ᴧᴧ⟩).
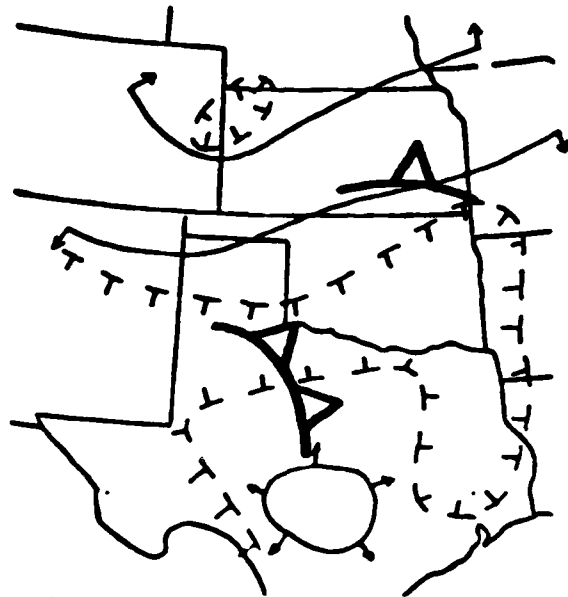
Fig.19a: Richardson numbers
(see text). Regions at and
above 500mb at 0300 GMT 11
April 1979 with $0 < R_i \leq .95$
(solid) and $0 < R_i \leq .25$(dashed).
500mb trough (⟨ᴧᴧ⟩).
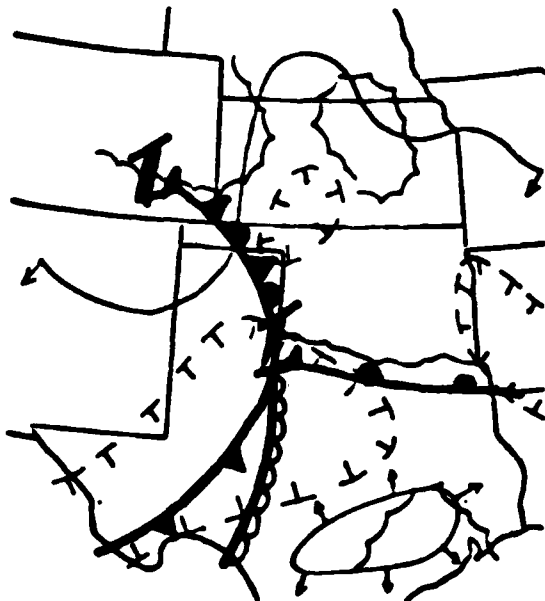
Fig.18b: Regions below 500mb
at 0000 GMT 11 April 1979
with $0 < R_i \leq .95$(solid) and
$0 < R_i \leq .25$(dashed). Surface
$R_i \leq .95$(scalloped). Surface
fronts, lows, and dry line.

Fig.19b: Regions below 500mb
at 0300 GMT 11 April 1979
with $0 < R_i \leq .95$(solid) and
$0 < R_i \leq .25$(dashed). Surface
$R_i \leq .95$(scalloped). Surface
fronts, lows, and dry line.

Fig.20a: Richardson numbers
(see text). Regions at and
above 500mb at 0600 GMT 11
April 1979 with 0 R_i .95
(solid) and 0<R_i≤.25(dashed).
500mb trough (‾∿‾).

Fig.21a: Richardson numbers
(see text). Regions at and
above 500mb at 0900 GMT 11
April 1979 with 0<R_i≤.95
(solid) and 0<R_i≤.25(dashed).
500mb trough (‾∿‾).

Fig.20b: Regions below 500mb
at 0600 GMT 11 April 1979
with 0<R_i≤.95(solid) and
0<R_i≤.25(dashed). Surface
R_i≤.95(scalloped). Surface
fronts, low, and dry line.

Fig.21b: Regions below 500mb
at 0900 GMT 11 April 1979
with 0<R_i≤.95(solid) and
0<R_i≤.25(dashed). Surface
R_i≤.95(scalloped). Surface
fronts, lows, and dry line.

103

Fig.22a: Richardson numbers (see text). Regions at and above 500mb at 1200 GMT 11 April 1979 with $0 < R_i \leqslant .95$ (solid) and $0 < R_i \leqslant .25$ (dashed). 500mb trough (◁◁◁).

Fig.22b: Regions below 500mb at 1200 GMT 11 April 1979 with $0 < R_i \leqslant .95$ (solid) and $0 < R_i \leqslant .25$ (dashed). Surface $R_i \leqslant .95$ (scalloped). Surface fronts, lows, and dry line.

104
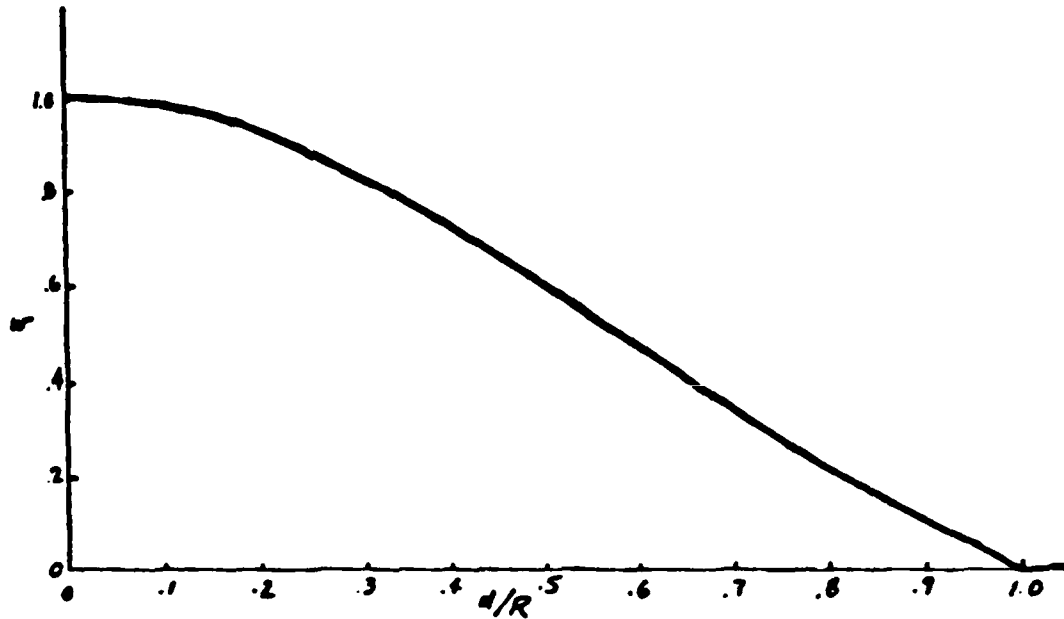
Fig.23: Cressman's weighting function versus the ratio
of distance from the gridpoint (d) to the radius of
influence (R).
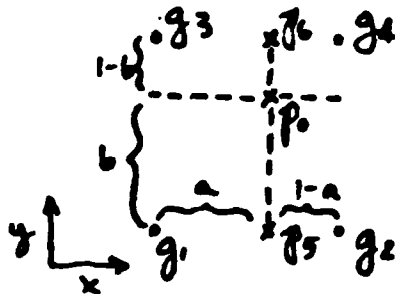
Fig.24: Bilinear interpolation of the value of a scalar
to a point, p_o, from gridded values at the four closest
gridpoints, g_1 through g_4.
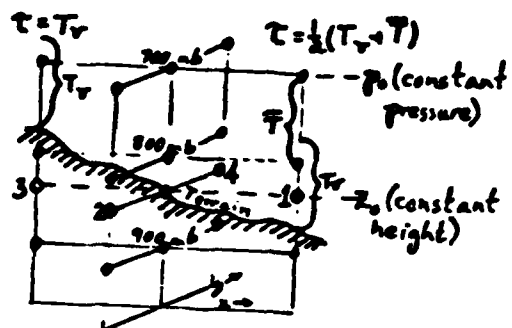
Fig.25: Scheme for deriving geostrophic
surface winds from gridded heights. See
text for explanation.
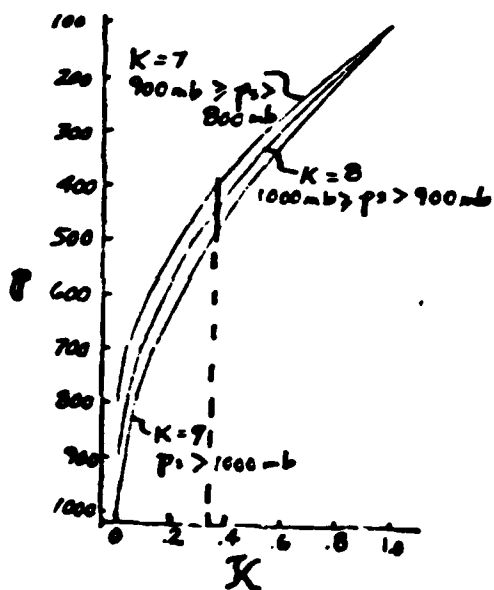
Fig.26: O'Brien's quadratic
correction factor as a function
of surface pressure (P_s) and
pressure level (p).
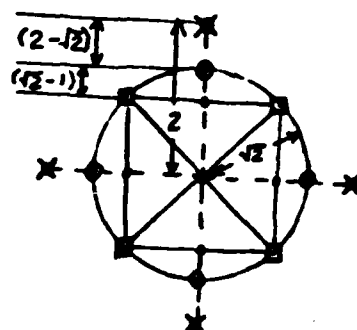
Fig.27: Data sampling for a modi-
fied shearing deformation operator
(circles) consistent in scale with
the stretching deformation (squares).
Standard sampling for shearing
deformation (x's) is inconsistent.
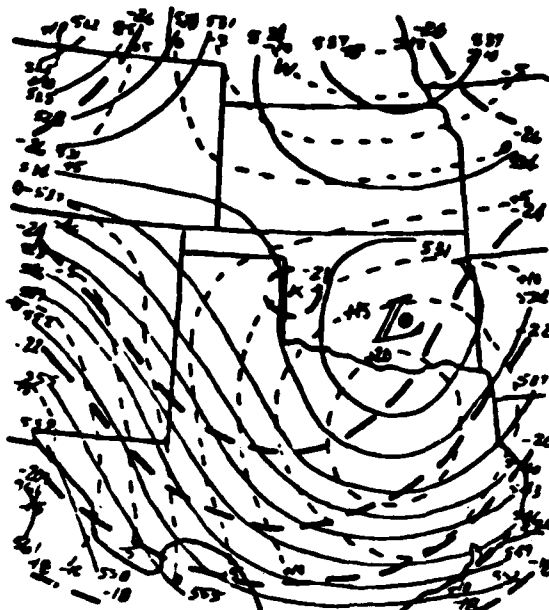
Fig.28a: Sanders' 500mb analytic height (m: solid lines), temperature (C: heavy dashed), and relative vorticity ($10^{-5}s^{-1}$: light dashed).
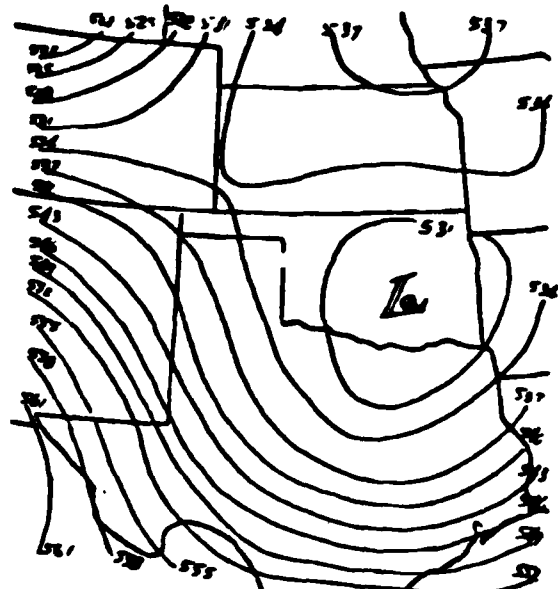
Fig.29a: Sanders' 500mb heights objectively analyzed using the geostrophic winds as bogus rawinsonde wind data.
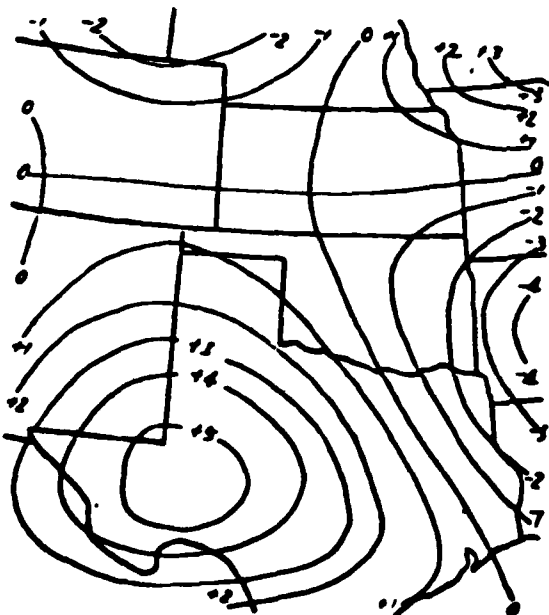
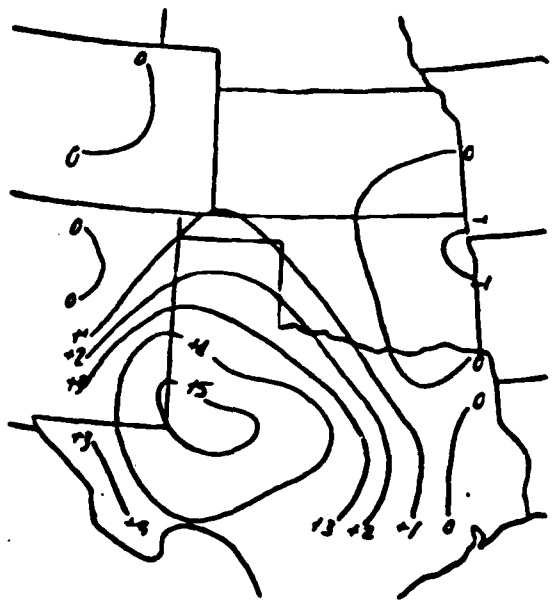Fig.28b: Sanders' 500 mb analytic quasi-geostrophic omega (µb/s).

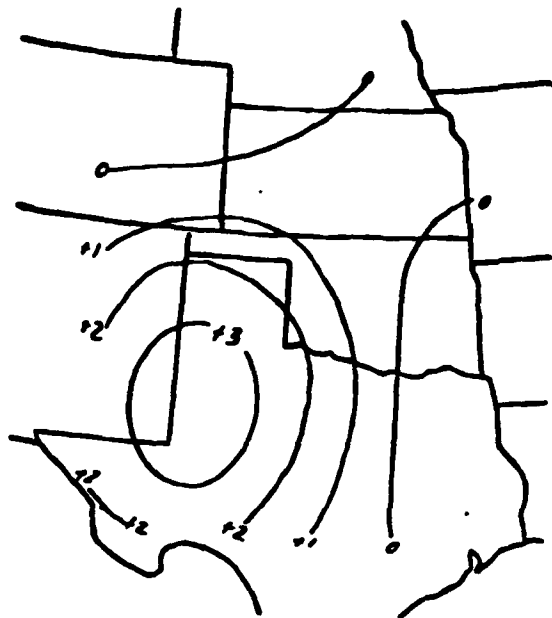Fig.29b: Quasi-geostrophic omega (µb/s) derived from the objectively analyzed height field.

Fig.30a: 500mb omega (μb/s) due to differential vorticity advection (F1) for Sanders' analytic height field (Figure E.1a).

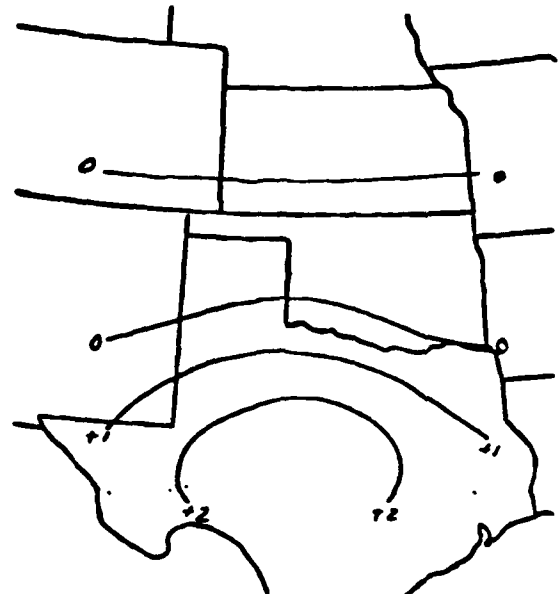**Fig.30b:** 500mb omega (μb/s) due to the laplacian of thermal advection (F2) for Sanders' analytic height field (Figure E.1a).

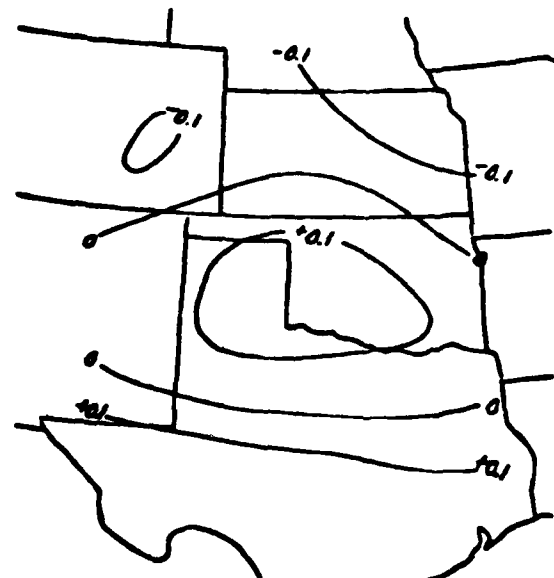**Fig.30c:** 500mb omega (μb/s) due to the advection of vorticity (2ζ·) by the thermal wind (F3) for Sanders' analytic heights.

Fig.30d: 500mb omega (μb/s) due to Wiin-Nielsen's deformation function (F4) for Sanders' analytic height field (Figure E.1a).

108